ELECTRONIC TRANSPORT PROPERTIES OF GRAPHENE-BASED HETEROSTRUCTURES

A thesis submitted to the University of Manchester
for the degree of Doctor of Philosophy
in the Faculty of Engineering and Physical Sciences

Manchester 2012

By
Liam Britnell
School of Physics & Astronomy

Contents

List of Figures

Abstract

Heterostructures fabricated from atomically thin crystalline layers are new materials which offer exciting possibilities for next-generation electronic and optoelectronic sensors and devices. The idea of heterostructures is not new and traditional semiconductor heterostructures have already played an important technological role in many modern electronic components. It is possible to fabricate new and exciting structures by stacking single atomic layers of different materials into heterostructures. This technology can be used to create materials and devices with a wide variety of properties. The stacking order, thickness, doping and crystal orientation play the major roles in determining the characteristics of these new materials.

The experimental work for this thesis involves the electrical characterisation of several different heterostructures.

i Investigation of boron nitride as an atomically thin tunnel barrier, including its homogeneity across micron sized areas. The area normalised conductance was found to depend on boron nitride thickness, changing by 1.5 decades per layer.

ii Graphene-based tunnelling transistors which exhibit current modulation by external gate voltage. With boron nitride as the tunnel barrier an on-off ratio of up to 40 was acheived.

iii Resonant tunnelling devices which show negative differential conductivity in their current-voltage characteristics.

iv Photodetection and solar cell devices using semiconducting tungsten disulfide. The maximum external quantum efficiency observed was 0.1 A/W which was approximately constant across the visible spectrum.

The enormous array of possibilities made available by this technology means that there is huge scope for further investigation with more exploratory research to make proof-of-principle functional devices for application in technology.

Declaration

No portion of the work referred to in this thesis has been submitted in support of an application for another degree or qualification of this or any other university or other institution of learning.

Copyright Statement

Acknowledgements

During the course of this PhD research I have been helped by more people than I can mention here. I would like to especially thank Sören Neubeck, Daniel Cunha-Elias and Peter Blake for their tutoring and endless patience, which has allowed me to work sucessfully in the last three years. My appreciation goes also to Axel Eckmann, Branson Belle, Roma Gorbachev, Rahul Nair and Artem Mishchenko for their invaluable advice and expertise. I must also thank Rashid Jalil and Thanasis Georgiou, among others, for the provision of so many interesting samples without which much of this research would have been impossible. Two others to whom I am indebted are Stan Gillot and Mark Sellers for their great assistance (naturally dished out with a healthy helping of sarcasm of course!). Lastly my heartfelt thanks goes to Andre Geim, Leonid Ponomarenko, Laurence Eaves and of course Kostya Novoselov for their guidance and supervision; giving me purpose, direction and endless inspiration.
And to you the reader, even if this is the only page of this thesis you read, it is much appreciated.

Liam Britnell
Manchester, November 2012

Dedicated to Bill, Jenny and Huw.

Publications

♢ A. Felten, B. S. Flavel, **L. Britnell**, A. Eckmann, P. Louette, J.-J. Pireaux, M. Hirtz, R. Krupke and C. Casiraghi
Single- and double-sided chemical functionalization of bilayer graphene
to appear in Small.

♢ V. G. Kravets, F. Schedin, R. Jalil, **L. Britnell**, R. V. Gorbachev, B. Thackray, D. Ansell, K. S. Novoselov, A. K. Geim, A. V. Kabashin and A. N. Grigorenko
Singular-phase nanooptics in plasmonic metamaterials: towards label-free single molecule detection to appear in Nature Materials.

♢ A Eckmann, A Felten, A Mishchenko, **L Britnell**, R Krupke, KS Novoselov, C Casiraghi
Probing the nature of defects in graphene by Raman spectroscopy
Nano Letters, **12** 3925-3930 (2012).

♢ S. J. Haigh, A. Gholinia, R. Jalil, S. Romani, **L. Britnell**, D. C. Elias, K. S. Novoselov, L. A. Ponomarenko, A. K. Geim and R. Gorbachev
Graphene-based heterostructures and superlattices: Cross-sectional imaging of individual layers and buried interfaces
Nature Materials, **11** 764-767 (2012).

♢ **L. Britnell**, R. V. Gorbachev, R. Jalil, B. D. Belle, F. Schedin, M. I. Katsnelson, L. Eaves, S. V. Morozov, A. S. Mayorov, N. M. R. Peres, A. H. C. Neto, J. Leist, A. K. Geim, L. A. Ponomarenko and K. S. Novoselov
Electron tunneling through ultrathin boron nitride crystalline barriers
Nano Letters, **12** 1707-1710 (2012).

♢ **L. Britnell**, R. V. Gorbachev, R. Jalil, B. D. Belle, F. Schedin, A. Mishchenko, T. Georgiou, M. I. Katsnelson, L. Eaves, S. V. Morozov, N. M. R. Peres, J. Leist, A. K. Geim, K. S. Novoselov and L. A. Ponomarenko
Field-effect tunneling transistor based on vertical graphene heterostructures
Science, **335** 947-950 (2012).

♢ V. G. Kravets, F. Schedin, R. Jalil, **L. Britnell**, K. S. Novoselov and A. N. Grigorenko
Surface hydrogenation and optics of a graphene sheet transferred onto a plasmonic nanoarray
Journal of Physical Chemistry C, **116** 3882-3887 (2012).

♢ T. Georgiou, **L. Britnell**, P. Blake, R. V. Gorbachev, A. Gholinia, A. K. Geim, C. Casiraghi and K. S. Novoselov
Graphene bubbles with controllable curvature
Applied Physics Letters, **99** 093103 (2011).

♢ A. S. Mayorov, R. V. Gorbachev, S. V. Morozov, **L. Britnell**, R. Jalil, L. A. Ponomarenko, P. Blake, K. S. Novoselov, K. Watanabe, T. Taniguchi and A. K. Geim
Micrometer-scale ballistic transport in encapsulated graphene at room temperature
Nano Letters, **11** 23962399 (2011).

♢ R. V. Gorbachev, I. Riaz, R. R. Nair, R. Jalil, **L. Britnell**, B. D. Belle, E. W. Hill, K. S. Novoselov,

K. Watanabe, T. Taniguchi, A. K. Geim and P. Blake
Hunting for monolayer boron nitride: optical and Raman signatures
Small, **7** 465468 (2011).

♢ T. J. Echtermeyer, **L. Britnell**, P. K. Jasnos, A. Lombardo, R. V. Gorbachev, A. N. Grigorenko, A. K. Geim, A. C. Ferrari and K. S. Novoselov
Strong plasmonic enhancement of photovoltage in graphene
Nature Communications, **2** 458 (2011).

♢ R. R. Nair, W. Ren, R. Jalil, I. Riaz, V. G. Kravets, **L. Britnell**, P. Blake, F. Schedin, A. S. Mayorov, S. Yuan, M. I. Katsnelson, H. M. Cheng, W. Strupinski, L. G. Bulusheva, A. V. Okotrub, I. V. Grigorieva, A. N. Grigorenko, K. S. Novoselov and A. K. Geim
Fluorographene: A Two-Dimensional Counterpart of Teflon
Small, **6** 2877-2884 (2010).

Part I

Introduction

Chapter 1

Introduction to graphene based heterostructures

In order to discuss graphene heterostructures it is necessary to first consider the properties of the constituent materials. This chapter will introduce the relevant properties of graphene, boron nitride and tungsten disulfide which are all used in later chapters. At the end of the chapter a general introduction to graphene-based heterostructures is given.

1.1 Graphene

Since the isolation of monolayer graphene from its parent material graphite in 2004[1] there has been a huge research interest in this two-dimensional system. Only a single atom thick, it can extend for millions of atoms laterally and possesses a range of superior properties[2]. The reasons why graphene has generated so much interest are many and varied but most come under the umbrella of two main concepts. Firstly it is a very 'clean' and simple system in which to investigate fundamental physics and chemistry: it is entirely composed of surface atoms and can be obtained with a low defect density (1 in 10^8)[3], making it a theoreticians' playground for exploring novel phenomena[4]. Secondly, due to its outstanding properties, it also has the potential to be utilised in a whole range of applications from computing[5], displays and optoelectronics[6], to composite materials[7]. Its two-dimensional nature making it uniformly modifiable[8] and hence a strong candidate in detection technologies: for example, its conductivity is highly sensitive to its chemical enviroment, making it ideal for gas sensing[9].

Many interesting physical phenomena can be observed in this near defectless material: The charge carriers, which can be tuned between electrons and holes, are massless, relativistic-like particles which exhibit the quantum Hall effect (integer and fractional) in magnetic fields[10]. They have very high mobility over a broad temperature range and one of the highest at room temperature. It exhibits interesting optical properties such as

[1] Novoselov, K. S. *et al. Science*, 306 (2004) 666–669.

[2] Novoselov, K. S. *Angewandte Chemie International Edition*, 50 (2011) 6986–7002.

[3] Ni, Z. H. *et al. Nano Letters*, 10 (2010) 3868–3872.

[4] Neto, A. H. C. *et al. Reviews of Modern Physics*, 81 (2009) 109–162.

[5] Yang, H. *et al. Science*, 336 (2012) 1140–1143.

[6] Bonaccorso, F. *et al. Nature Photonics*, 4 (2010) 611–622.

[7] Huang, X. *et al. Chemical Society Reviews*, 41 (2012) 666–686.

[8] Liu, J., Tang, H. & Gooding, J. J. *Journal of Materials Chemistry*, 22 (2012) 12435–12452.

[9] Schedin, F. *et al. Nature Materials*, 6 (2007) 652–655.

[10] Dean, C. R. *et al. Nature Physics*, 7 (2011) 693–696.

a visible light absorption defined solely by fundamental constants, $\pi\alpha$=2.3%[11]. Furthermore, it is also one of the strongest materials ever measured, comparable with diamond yet can be stretched up to 20% before fracturing[12]. It also possesses a very good thermal conductivity[13], making it a potential heat sink material.

Another reason interest has accelerated so quickly is that it is very easily produced–simply by peeling layers off graphite with 'scotch tape'–making it easily accessable to any research group. That said, it can also be mass produced by a variety of methods including chemical vapour deposition[14] and chemical exfoliation[15] which are beginning to bear fruit and hence it has been touted as a disruptive technology, with the potential to out-perform and replace state-of-the-art materials across many areas[16].

[11] Nair, R. R. *et al. Science*, 320 (2008) 1308.

[12] Lee, C. *et al. Science*, 321 (2008) 385–388.

[13] Balandin, A. A. *et al. Nano Letters*, 8 (2008) 902–907.

[14] Bae, S. *et al. Nature Nanotechnology*, 5 (2010) 574–578.

[15] Coleman, J. N. *et al. Science*, 331 (2011) 568–571.

[16] Novoselov, K. S. *et al. Nature*, 490 (2012) 192–200.

1.1.1 Crystal structure

Graphene is a honeycomb-like lattice of carbon atoms constructed from two interpenetrating triangular Bravais lattices. Its unit cell contains two atoms, one from each triangular lattice, in non-identical enviroments. The structure is drawn in fig. 1.1**a**, where the two non-identical carbon sites **A** and **B** are shown along with the principal lattice vectors. The nearest neighbour distance (C-C bond length) d_{nn} is 1.42 Å and the principal vector length is 2.46 Å. The stacking of the graphene layers in graphite is called AB (or Bernal) stacking which means each layer is shifted $a/\sqrt{3}$ from it's neighbouring planes above and below. Bi- and tri- layer graphene are interesting in their own right, with their own unique properties but will not be discussed further. The number of layers in a given graphene sample can be determined by several methods: optical contrast between sample and substrate[17], Raman spectroscopy[18] and atomic force microscopy (see the chapter 2 on experimental techniques). Due to its rather non-invasive nature, Raman spectroscopy is the tool of choice in most circumstances.

[17] Blake, P. *et al. Applied Physics Letters*, 91 (2007) 063124.

[18] Ferrari, A. C. *et al. Physical Review Letters*, 97 (2006) 187401.

Graphene is a semimetal[19] with an exactly zero band gap where the density of electronic states (DOS) vanishes at the meeting point of the conduction and valance bands. The first theoretical investigations of graphene were made in the late 1940s[20], over half a century before it was discovered experimentally[21]. Graphene was studied theoretically to help understand the electrical properties of graphite and also as it is the building block of carbon nanotubes and fullerenes. The tight-binding calculation for graphene, presented by Wallace in his 1947 paper, is often still used today.

[19] A semimetal's conductivity lies in between that of a semiconductor and a true metal because it has no band gap but a low density of electronic states near the Fermi level.

[20] Wallace, P. R. *Physical Review Letters*, 71 (1947) 622–634.

[21] Novoselov, K. S. *et al. Science*, 306 (2004) 666–669.

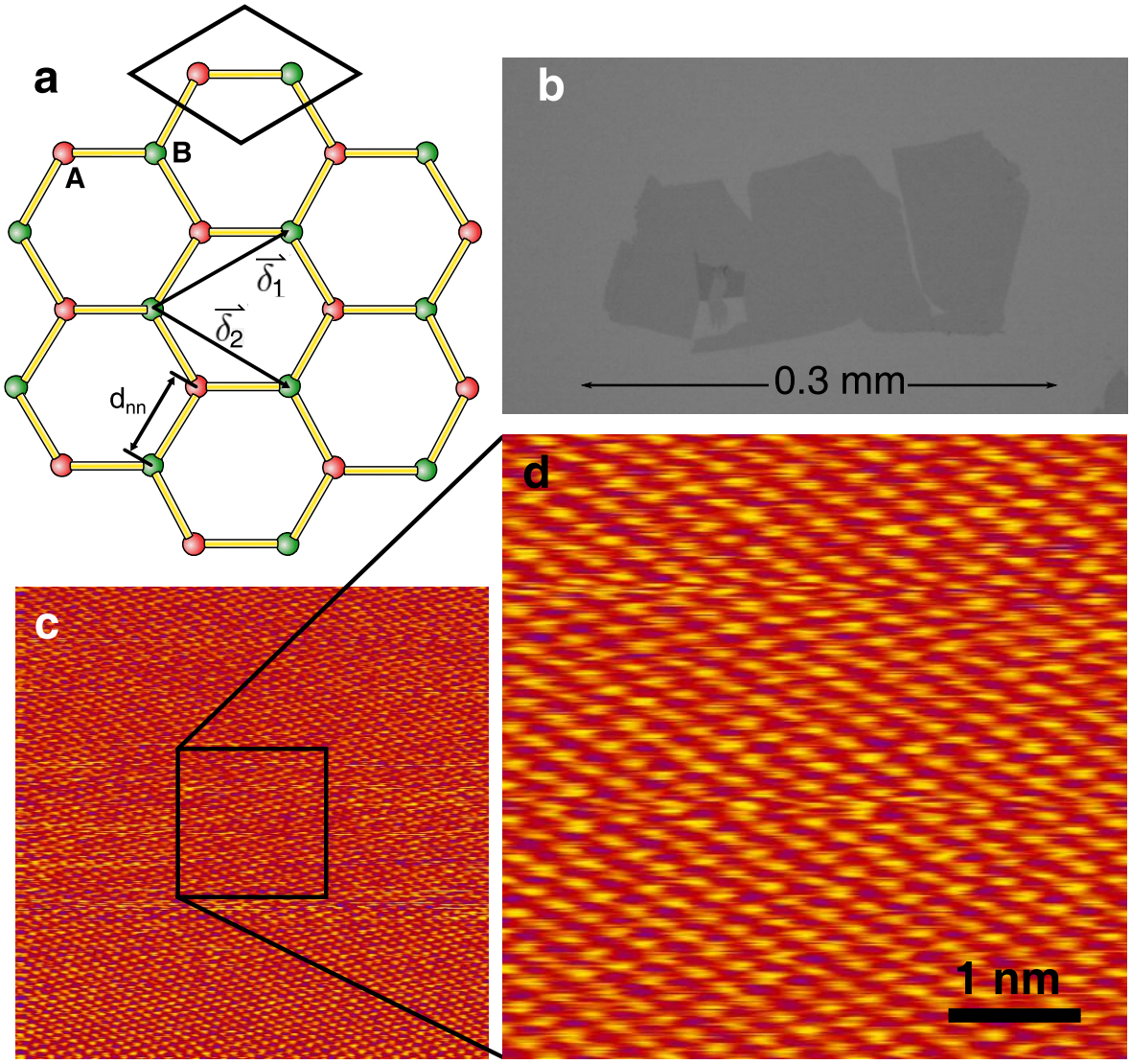

Figure 1.1: **a** The crystal structure of graphene showing the **A** and **B** sublattices (red and green atoms respectively), principal lattice vectors and carbon-carbon bond length d_{nn}=1.42 Å. The lattice constant is 2.46 Å. The primitive cell is also shown. **b** An optical image of monolayer graphene on Si/SiO_2 produced by micromechanical cleavage. **c** and **d** are lattice resolution scanning tunnelling microscope images of the surface of graphite. The lattice is triangular rather than hexagonal due to coupling with the graphene layer below. As shown, **d** is a zoomed image of **c**.

The tight-binding approach is a way to calculate band structures by considering how the wave functions of the atoms overlap. For graphene, it is possible to reach an analytical solution in the case where only hopping of electrons between nearest neighbour carbon atoms is considered. It is physically insightful and gives a good approximation to the band structure. It is interesting to note that in the case of bilayer graphene it is important to also take second nearest neighbour hopping into account in order to understand physics close to the charge neutrality point[22].

[22] Mayorov, A. S. *et al.* *Nano Letters*, 12 (2012) 4629–4634.

From the crystallographic structure of graphene, see fig. 1.1, it is possible to analytically obtain a good approximation of the band structure using this method. The carbon atoms have four valence electrons with orbitals $2s$, $2p_x$, $2p_y$ and $2p_z$. In the graphene lattice the carbon-carbon bonds are sp^2 hybridized, meaning the overlaping $2s$, $2p_x$ and $2p_y$ wavefunctions form a single hybrid orbital while the $2p_z$ orbital is decoupled from the others and it is only electrons in this orbital which are free to jump between atoms. It is the $2p_z$ (or π electrons) that dominate electronic transport through the lattice.

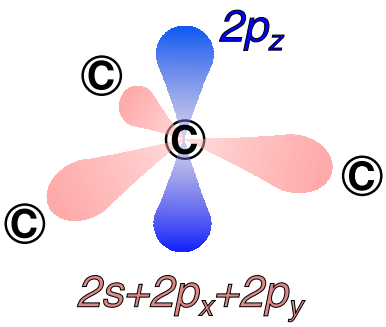

Figure 1.2: The electron orbtials of sp^2 hybridized carbon. $2s$, $2p_x$ and $2p_y$ form a single in-plane orbital while $2p_z$ is decoupled from the rest and lies out-of-plane.

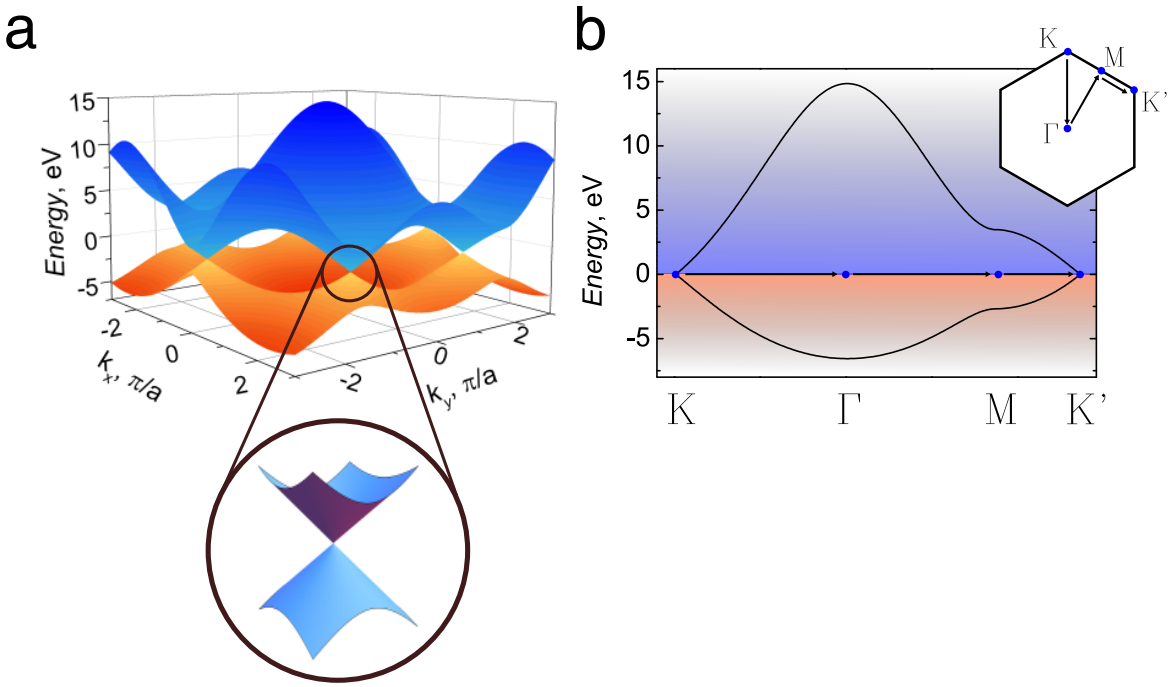

Figure 1.3: The band structure of the π orbitals of graphene calculated using the nearest neighbour tight-binding approach. **a** A 3D plot of the band structure in momentum space, the zoomed section shows the linear dispersion relation close to the Dirac point where the bands meet. **b** The two branches shown along the high symmetry triangle shown in the inset.

Before giving the results of the tight-binding calculation, the full derivation of which can be found elsewhere[23], a few terms need to be defined.

A lattice (being a periodic array of points in real space) can be Fourier transformed to give another periodic array of points in so-called reciprocal space–this new lattice being called the

[23] Saito, R., Dresselhaus, G. & Dresselhaus, M. S. *Physical Properties of Carbon Nanotubes*. Imperial College Press (1998).

reciprocal lattice. For a hexagonal lattice with a principal vector length a in real space, the reciprocal lattice is also hexagonal and the new principal vectors have a length $\frac{2\pi}{a}\frac{2}{\sqrt{3}}$. The Wigner-Seitz cell of the reciprocal lattice is called the first Brillouin zone. The band structure is how the allowed energies of the electrons in the lattice depend on their momentum k in the reciprocal lattice.

With these terms defined it is possible to describe the main results of the tight-binding calcualtion for graphene, which are as follows. The energy bands

$$E(\vec{k}) = \frac{\epsilon_{2p} \pm tw(\vec{k})}{1 \pm sw(\vec{k})} \tag{1.1}$$

where

$$w(\vec{k}) = \sqrt{1 + 4\cos\frac{\sqrt{3}k_x a}{2}\cos\frac{k_y a}{2} + 4\cos\frac{k_y a^2}{2}} \tag{1.2}$$

where a is the length of the primitive vector in real space and $k_x$and k_y are the x and y components of the electrons momentum. t and s are the hopping and overlap energies and their values used here are -3.033 and 0.129 respectively. t is the energy for an electron to jump between nearest neighbours and s is the energy overlap of the wave functions of nearest neighbours. The onsite energy ϵ_{2p} is taken as zero. The band structure is shown in fig. 1.3**a** and the two branches between the high symmetry points are shown in fig 1.3**b**. The important points gleaned from this picture are that the bands touch at 6 points around the edge of the first Brillouin zone and the fact that the bands are linear close to these points is uncommon. The linearity can be shown by taking a Taylor expansion of dispersion relation around these points[24]. The key points marked on the band structure diagram are also shown in the representation of the Brillouin zone. The most relevant points on the diagram, considering the present discussion, are those marked **K** and **K'**. These are the points where the conduction and valence bands touch.

[24] The DOS is linearly dependent on energy near the Dirac point, a direct result of the linear dispersion relation.

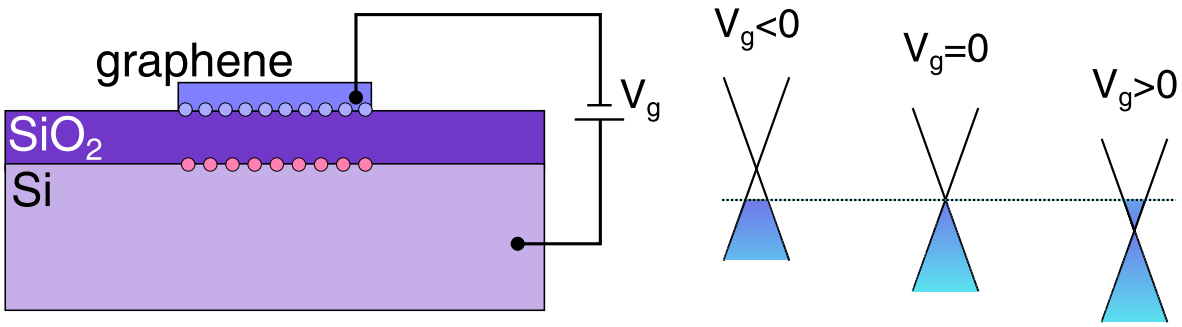

Figure 1.4: Electrostatic gating of graphene on an oxidised silicon wafer. A voltage applied between graphene and the Si induces charges in the graphene sheet due to the electric field across the oxide layer. In the diagram shown, the positive V_g means electrons are accumulated in graphene and the Fermi level is shifted from the Dirac point into the conduction band. For V_g <0, the Fermi level is in the valence band and carriers are holes as shown on the right.

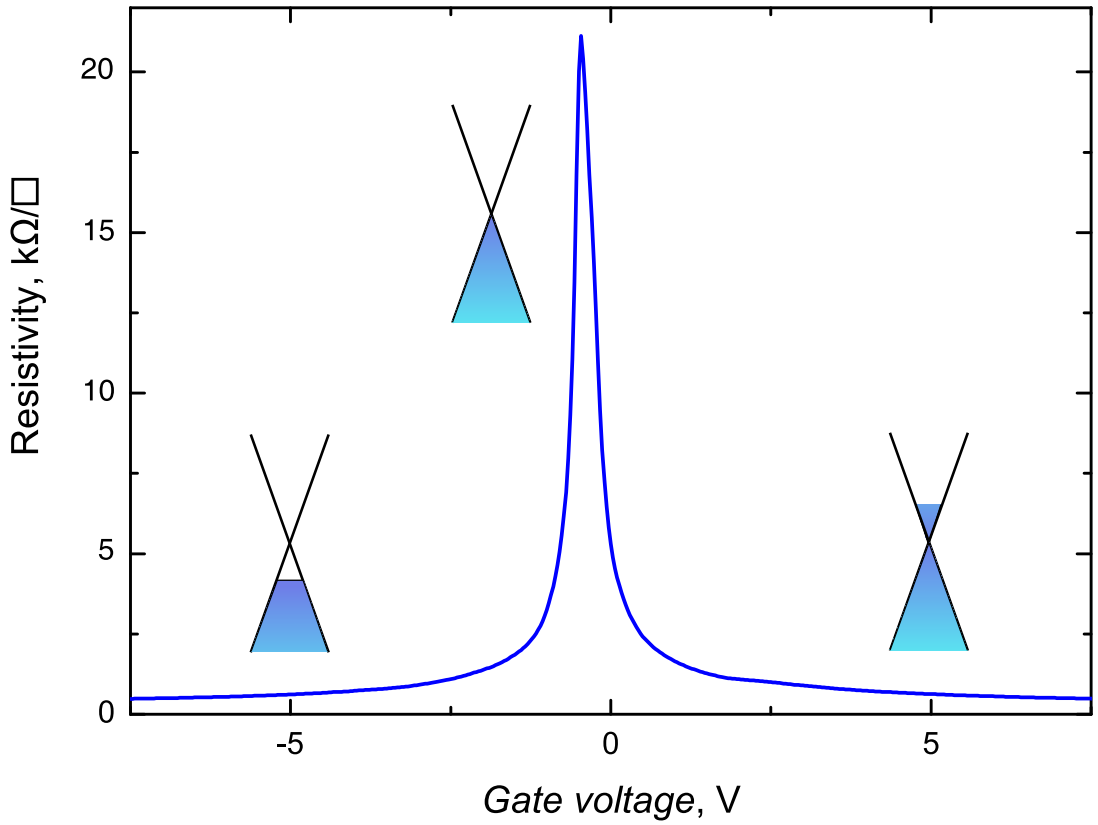

Figure 1.5: Resistivity of graphene as a function of gate voltage. For V_g >0 (V_g <0), the Fermi level is in the conduction (valence) band and carriers are electrons (holes). The resistivity reaches a maximum when the Fermi level is sitting at the Dirac point near V_g ∼0.

1.1.2 Electrostatic gating

For undoped graphene the Fermi level lies at the Dirac point, where the conduction and valence bands meet. At this point, the DOS vanishes and thus it is expected that the resistance would approach an infinite value, but experimentally it always remains finite[25]. It is worth saying that it is very difficult to experimentally study physics close to the Dirac point due to the existence of electron hole puddles which act to smear out this region[26,27]. To change the carrier density in graphene the Fermi level needs to be moved relative to the graphene bands;

[25] Novoselov, K. S. *et al.* *Nature*, 438 (2005) 197–200.

[26] Martin, J. *et al.* *Nature Physics*, 4 (2007) 144–148.

[27] Mayorov, A. S. *et al.* *Nano Letters*, 12 (2012) 4629–4634.

this can be done by electrostatic gating. Graphene is often deposited on a dielectric which allows application of a gate voltage. In fig. 1.4 graphene is shown sitting on a Si/SiO_2 wafer. As a parallel plate capacitor, a voltage applied to the Si induces a charge of opposite sign in the graphene and hence the Fermi level can be moved into either the conduction or valence band. The relation between the position of the Fermi level (relative to the Dirac point) and the induced charge carrier concentration n is $\varepsilon_F = \sqrt{n\pi}\hbar v_F$, where $\hbar$ is the reduced Planck constant and v_F is the Fermi velocity in graphene which is $\sim 10^6$ ms^{-1}. It can be seen that the charge carriers in graphene, can be tuned between electrons and holes with the crossover at the Dirac point. Easily achievable carrier concentrations are of the order 10^{13} cm^{-2} which corresponds to a shift of the Fermi level of around 350 meV. This can be further increased by using a polymer electrolyte[28].

[28] Pachoud, A. *et al. Europhysics Letters*, 92 (2010) 27001.

As the number of available charge carriers changes, the resistivity decreases as shown in fig. 1.5. The Dirac point lies close to V_g=0 and for V_g <0 the charge carriers are holes and for V_g >0 electrons. The maximal resistance does not lie at V_g=0 due to residual doping from processing.

1.2 Other Two-Dimensional Crystals

Graphene is promising to revolutionise technology in its own right, but since its discovery a whole catalogue of two-dimensional materials have been found, using the same fabrication techniques[29]. Most are interesting, and between them they cover a wide variety of properties.

[29] Novoselov, K. S. *et al. Proceedings of the National Academy of Sciences of the United States of America*, 102 (2005) 10451–10453.

Graphene is a very versatile material but it does have several draw backs. An obvious example of this is that because it has a zero band gap it is very power consuming when used as a transistor as it has no real *off* state. Although much work is being undertaken to try and overcome this, and other, obstacles it is also important that one does not ignore other materials. For this reason there is a large focus in the community on combining graphene with other materials to create novel materials and structures with well defined properties. The following section will introduce and focus on a few of the possible materials for these heterostructures.

A common feature of all the materials is that they are of a layered nature and hence are cleavable by the *scotch tape* technique but can also be produced in bulk by other methods such as chemical exfoliation[30].

[30] Coleman, J. N. *et al. Science*, 331 (2011) 568–571.

1.2.1 Hexagonal Boron Nitride (hBN)

Several crystalline forms of boron nitride exist; it has both cubic and wurtzite structures but the more stable and useful here, is its hexagonal form (hBN). hBN is a layered crystal similar to graphite but that the A and B sublattices, referred to in section 1.1.1, are made up of different elements: boron and nitrogen atoms in an ionic lattice.

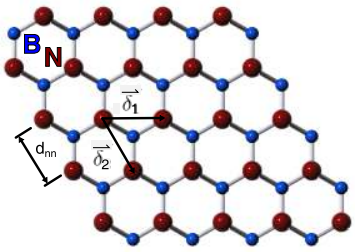

Figure 1.6: The crystal structure of hexagonal boron nitride, view parallel to the c-axis. The lattice bonding is primarily ionic because of the difference in electron affinity. The boron atoms are shown in blue and the nitrogen in red.

Although used widely in its own right, as a lubricant amongst other things, the reason for interest in hBN related to graphene, was initially because it proved to be a high quality substrate for graphene electronics[31]. hBN is a dielectric with a large bandgap (∼6 eV)[32] and a dielectric constant similar to SiO_2 (∼$4\epsilon_0$ where ϵ_0 is the permittivity of free space).

It has been shown that it is possible to extract single atomic planes from the bulk crystal[33], in a similar fashion to graphene from graphite by micromechanical cleavage–few layer samples have been shown to have a comparable strength to graphene[34]. However the optical properties of graphene and monolayer hBN are quite different meaning that typically hBN gives a low visible contrast on most substrates. For graphene on oxidised silicon (300 nm oxide), an interference effect enhances its contrast to around 10% making it easily visible with an optical microscope. Under the same conditions, hBN is barely visible with a contrast on the order of only a few percent. To facilitate the fabrication procedures, work was undertaken to find the conditions for optimal contrast[33], this is discussed further in chapter 3 and appendix A.

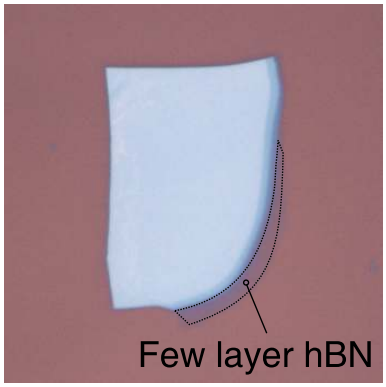

Figure 1.7: An optical image of hBN on SiO_2. A few-layer hBN region is found near at the edge of a thicker flake, inside the dotted line.

1.2.2 Transition metal dichalcogenides

Another group of layered materials is the transition metal dichalcogenides (TMDCs) which are currently attracting much interest. They are structured such that each layer consists of a three atomic planes: a layer of transition metal atoms (Mo, Ta, W...) sandwiched between two layers of chalcogen atoms (S, Se or Te), see fig 1.8. There is strong covalent bonding between the atoms within each layer and predominantly weak van der Waals bonding between adjacent layers. Many of these materials MoS_2, WS_2, TaS_2 to name a few are structurally similar but have an array of electronic properties ranging from semiconducting[35] to metallic[36] depending on their exact composition and thickness[37]. One example, tungsten disulfide (WS_2), has various applications including solid state lubrication and industrial surface protection[38,39].
The source, and hence quality, of the crystals has a strong

[31] Dean, C. R. *et al.* *Nature Nanotechnology*, 5 (2010) 722–726.

[32] Watanabe, K., Taniguchi, T. & Kanda, H. *Nature Materials*, 3 (2004) 404–409.

[33] Gorbachev, R. V. *et al.* *Small*, 7 (2011) 465–468.

[34] Song, L. *et al.* *Nano Letters*, 10 (2010) 3209–3215.

[35] Mattheiss, L. F. *Physical Review B*, 8 (1973) 3719–3740.

[36] Ayari, A. *et al.* *Journal of Applied Physics*, 101 (2007) 014507.

[37] Kumar, A. & Ahluwalia, P. K. *European Physical Journal B*, 85 (2012) 186.

[38] Hilton, M. R. & Fleischauer, P. D. *Surface and Coatings Technology*, 54-55 (1992) 435–441.

[39] Cohen, S. R. *et al.* *Thin Solid Films*, 1-2 (1998) 190–197.

effect on their properties; it is well known in semiconductors that impurity states can affect performance greatly. Also, some of the crystals are unstable in air and easily oxidise making fabrication processing difficult. In this work the field of view is restricted to include only tungsten disulfide WS_2 as it was relatively easy to work with and gave good device performance, as discussed in chapter 6.

Bulk WS_2 is a semiconductor with an indirect band gap of ∼1.3 eV and a direct gap ∼1.8 eV[40]. By studying fig. 1.9, one can see in bulk WS_2, the fundamental gap is a transition from the conduction band at **T** to the valence band at **Γ** ($E_{indirect}$=1.3 eV), while there is a direct gap at **K** of E_{direct}=1.8 eV. The evolution from three dimensions to two, leads to $E_{indirect}$ increasing from 1.3 eV to 2.1 eV; so in monolayer the fundament gap is a direct transition at **K** with the energy virtually unchanged. This means monolayer WS_2 has a much enhanced photoluminescence[41] because radiative recombination becomes favourable. Bulk films however still have a large optical absorption coefficient $\sim 10^7 m^{-1}$, which makes them suitable for photodetection and light harvesting devices[42].

[40] Kam, K. K. & Parkinson, B. A. *Journal of Physical Chemistry*, 86 (1982) 463–467.

[41] Gutiérrez, H. R. *et al.* *arXiv:1208.1325*, (2012).

[42] Ballif, C. *et al.* *Applied Physics A: Materials Science & Processing*, 62 (1996) 543–546.

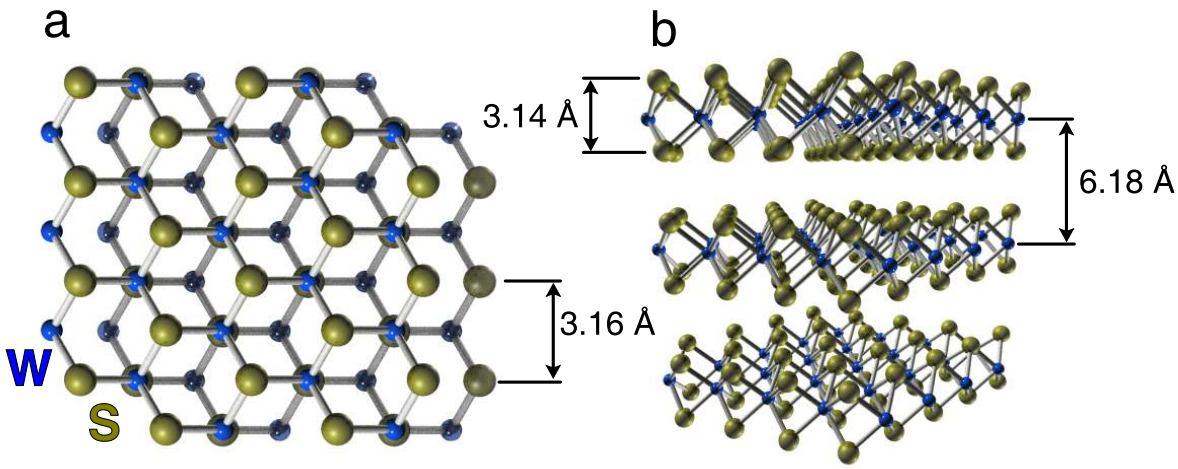

Figure 1.8: The crystal structure of tungsten disulfide. **a** View parallel to the *c*-axis **b** Portions of three atomic planes. The strong intra-plane covalent bonding is shown by the bars connecting W and S atoms. The interlayer distance $c/2$ is 6.18 Å[a], the intralayer S-1S distance is 3.14 Å[b] and the intralayer S-S distance *a* is 3.16 Å[c]. There are other TMDCs which share this trigonal prism structure but have slightly differing lattice constants. They have the generic formula MX_2, where M = Mo, W and X = S, Se, Te.

[a] Tenne, R. *et al.* *Nature*, 360 (1992) 444–446.

[b] Schutte, W. H., De Boer, J. L. & Jellinek, F. *Journal of Solid State Chemistry*, 70 (1987) 207–209.

[c] Bromley, R. A., Murray, R. B. & Yoffe, A. D. *Journal of Physics C: Solid Sate Physics*, 5 (1972) 759–778.

The photoactive properties of WS_2 are utilised in heterostructures in chapter 6.

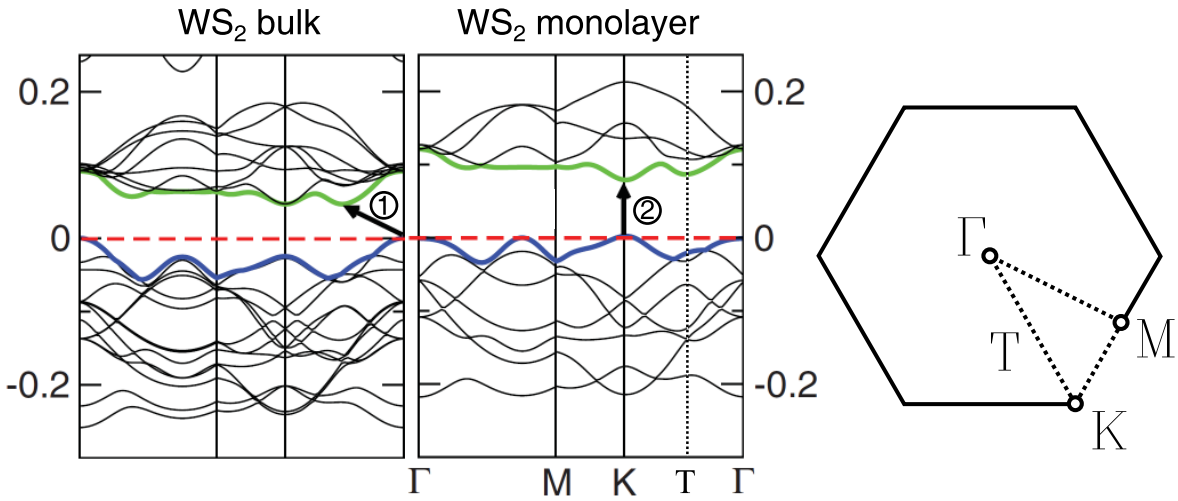

Figure 1.9: The band structure of bulk and monolayer WS_2. The fundamental band gap is indirect for bulk ($\mathbf{\Gamma} \rightarrow \mathbf{T}$–labelled (1)) and direct for monolayer (**K**–labelled (2)). *This figure is adapted from Gutiérrez et al.*[a]

[a] Gutiérrez, H. R. *et al. arXiv:1208.1325*, (2012).

1.2.3 Chemically modified graphene: graphane and fluorographene

Chemical derivatives of graphene are also potential heterostructure components. Graphene can be chemically modified by covalently bonding atomic hydrogen or fluorine to the lattice[43,44], see fig. 1.10. In doing so, the dissociated electrons are soaked up as the hybridization of the orbitals changes from sp^2 to sp^3, where all the electron orbitals form a single hybrid orbital. As a result the material becomes insulating and interacts with its environment differently, becoming hydrophilic in the case of graphane for example. Both materials have been investigated for use in heterostructures but problems associated with fabrication must be overcome before they can be utilised. For fluorographene, the aggressive reaction of fluorine with no only graphene but with many common substrates is a problem. In the case of graphane, stability over time needs to be fully investigated and addressed.
Work related to the strength of fluorographene was undertaken and is presented in appendix B.

[43] Elias, D. C. *et al. Science*, 323 (2009) 610–613.

[44] Nair, R. R. *et al. Small*, 6 (2010) 2877–2884.

1.3 Graphene production by mechanical cleavage

There are many ways to produce graphene; any one being chosen depending on the quantity and quality of graphene required.
All the results presented in the later chapters were made on graphene obtained by the well-known 'scotch-tape' technique.

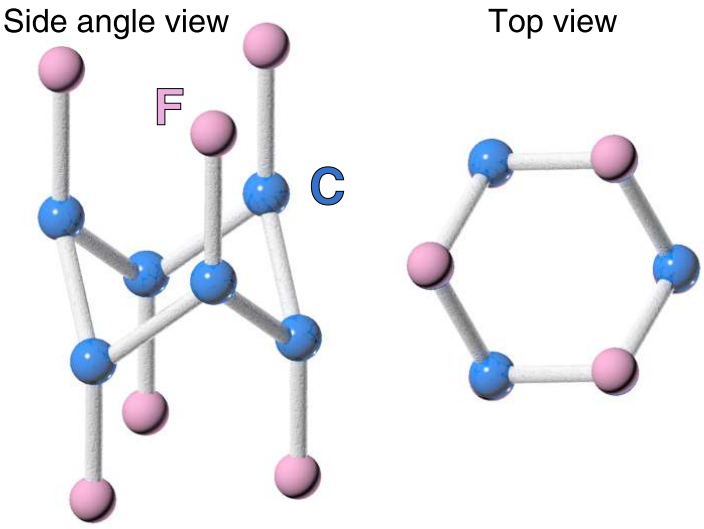

Figure 1.10: The structure of fluorographene where the carbon atoms are blue and the fluorine atoms pink. Fluorographene retains the hexagonal lattice of graphene but with atomic scale out-of-plane corrugations[45].

This technique, although impractical for any scaleable processes, gives the cleanest and highest quality samples. The technique is well described elsewhere[46] but in principle is as follows. With reference to fig. 1.11, a graphite crystal is lightly pressed onto a piece of adhesive tape leaving an impression of the crystal on the tape. This is repeated several times until thin graphite crystals cover an area similar that of the chosen substrate. The graphite covered tape is firmly pressed onto a freshly cleaned substrate. Commonly, an oxidised silicon wafer is used as a substrate and can be pre-treated by oxygen plasma. The tape is either carefully removed by hand or dissolved, leaving thin graphite/graphene flakes behind. A typical image of what is left on Si/SiO_2 is shown in fig. 1.11**b**. There are always flakes with a range of thicknesses left on the substrate so using an optical microscope, graphene flakes are found by optical contrast and subsequently the thickness confirmed by Raman spectroscopy[47]. This is also dicussed in chapter 2.

[45] Samarakoon, D. K. *et al.* *Small*, 7 (2011) 965–969.

[46] Novoselov, K. S. *et al.* *Proceedings of the National Academy of Sciences of the United States of America*, 102 (2005) 10451–10453.

[47] Ferrari, A. C. *Solid State Communications*, 143 (2007) 47–57.

1.4 Fabrication via deterministic flake transfer

In order to make the heterostructures which are the main focus of this work it is necessary to accurately transfer flakes onto each other with as little contamination as possible. There are several techniques being used by the community and the design of the device will determine which is most appropriate to use. There is a point of note related to relative crystal orientation: the crystals are transferred without knowledge of their crystallographic directions, meaning their relative orientation

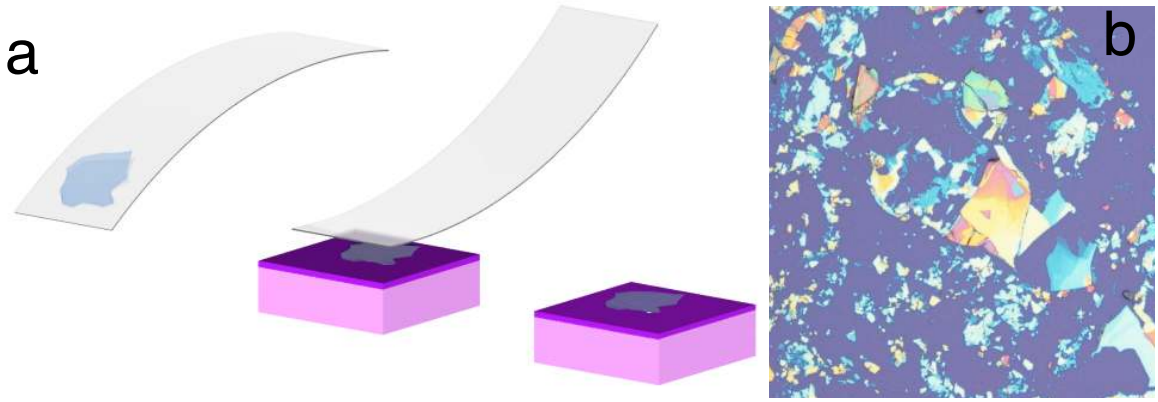

Figure 1.11: **a** Cartoon of the 'scotch-tape' technique to produce graphene flakes for device fabrication. First an impression of a graphite flake is made on adhesive tape which is then firmly pressed onto a substrate such as an oxidised silicon wafer. **b** Among the debris, monolayer graphene can be found.

is random. For graphene on hBN it has been shown to that new phenomena appear when the lattices are aligned[48] but the affected energy scale is far from the Dirac point unless the misorientation is less than a few degrees so it is deemed have little impact on this work. It is possible to choose the orientation by aligning crystals by using flakes with edges that follow obvious crystallographic lines. It should be pointed out that it is not the intention of this thesis to present novel work related to fabrication of heterostructures and that the role of the author was primarily to characterise such materials using a variety of techniques including scanning probe microscopy, Raman spectroscopy and electronic transport measurements.

[48] Yankowitz, J. X. M. *et al. Nature Physics*, 8 (2012) 382–386.

'Wet' Transfer

The original techniques used to transfer graphene flakes from the surface of a silicon wafer are labelled *wet transfer* because they involve the immersion of the graphene flakes in solvents thus contaminating the device surface. A more complete description of the techniques has been given by Schneider *et al.*[49] but a brief description is given here. The general idea behind two techniques–'wedge' and 'etch' transfer–is that a polymer is spun on the substrate (such as Si/SiO_2) after the flakes have been identified. In wedge transfer cellulose acetate butyrate (CAB) is spun on the surface and then the sample is immersed in water which allows the polymer to release from the surface with the graphene flakes adhered to the bottom surface of the CAB. The polymer membrane can then be transferred to the surface of another substrate and positioned then finally dissolved to leave the graphene flake in the required position. A variant of this technique uses poly(methyl methacrylate) (PMMA) spun on the top surface and then the surface of the SiO_2 can be etched using buffered potassium hydroxide (KOH). A vital point about the fabrication of heterostructure devices is the interfaces between the various materials, this is especially true of tunnelling devices. With these techniques it is difficult to clean the interface and thus there can be a lot of contamination trapped leading to irreproducibility in the measurements. To overcome this problem a different technique is now preferentially used which is described below.

[49] Schneider, G. F. *et al.* *Nano Letters*, 10 (2010) 1912–1916.

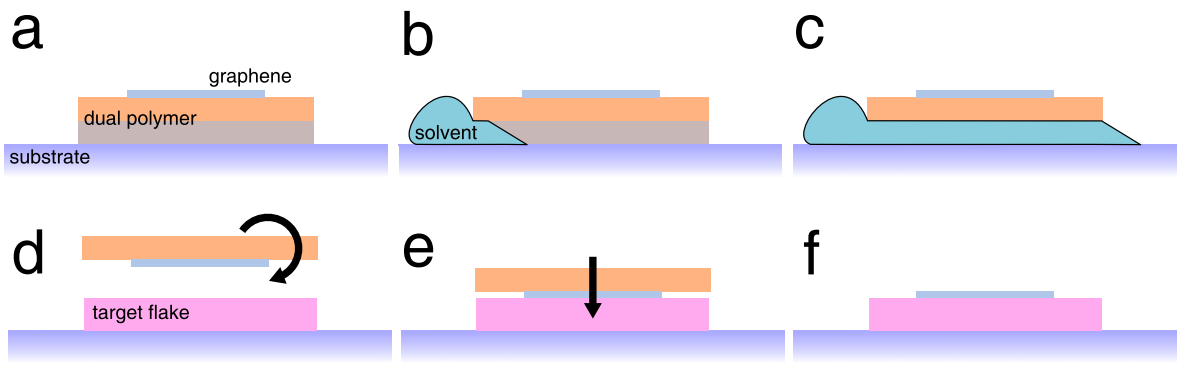

Figure 1.12: The *dry transfer* technique to produce heterostructures. **a** Graphene is cleaved onto a dual polymer stack sitting on a rigid substrate. **b** Solvent is injected underneath the polymer stack. **c** The solvent selectively dissolves the bottom polymer layer. **d** The top polymer layer is inverted and can be taken and positioned above the target flake. **e** The two flakes are carefully brought into contact. **f** The top polymer is dissolved and the sample annealled to removed contamination.

'Dry' Transfer

For this *dry transfer* technique the graphene flakes are initially exfoliated onto a double layered polymer (fig. 1.12**a**) which has been spun onto a silicon wafer. The technique has the draw back that in general the flakes obtained are smaller due to the lower adhesion between graphene and the polymer and also the optical contrast is lower due to the changes in interference

conditions of the substrate. However, the major advantage of this technique is that the bottom polymer layer can be selectively dissolved by directly injecting a solvent under the top layer without the graphene contacting the solvent (fig. 1.12**b,c**). The membrane can be picked up, inverted (fig. 1.12**d**) then positioned above the target and carefully placed in contact with the substrate (fig. 1.12**e**). The remaining polymer layer can then be dissolved and the top surface of graphene annealed thoroughly in a gaseous mixture of H_2/Ar (10:90) at 300°C to remove any remaining polymer contamination (fig. 1.12**f**). As it is not trapped at the interface but on top, it is easily removed. Cross-sectional transmission electron microscopy of such devices shows a very clean, contamination free interface[50].

[50] Haigh, S. J. *et al.* *Nature Materials*, 11 (2012) 764–767.

The *dry transfer* technique is used preferentially because it typically results in a much cleaner interface than other methods. All measurements of the work in this thesis were made on samples fabricated with this technique unless stated otherwise.

1.4.1 Other fabrication techniques

Mechanical cleavage gives the highest quality graphene under the right conditions and can give monolayer flakes up to 1 mm in size. However, for mass production of graphene–as would be required for applications–there exist various other methods to produce graphene. The quantity, roughly dictating the quality. Chemical vapour deposition (CVD) is a common method of producing high purity materials for the semiconductor industry. The principle behind the method is that chemical ingredients are vapourised inside a heated furnace containing a substrate where growth is seeded. By careful control of the conditions inside the furnace (flow rate, temperature and pressure etc) , thin films can form on the surface of the substrate. In the case of graphene, much research has gone into increasing the quality of the product and decreasing the process cost in order to find a viable method of mass producing graphene[51]. To produce large area graphene films by CVD, a carbon containing gas–usually methane (CH_4)–is allowed to flow into a furnace at ∼1000°. The gas dissociates and carbon can start to form graphene on the substrate surface. To date, the best results have been achieved with Cu, where the thickness is predominantly monolayer due to a self-limited growth process[52]. The result is graphene with a fairly high degree of purity and grain size, depending on the growth parameters.

[51] Mattevi, C., Kim, H. & Chhowalla, M. *Journal of Materials Chemistry*, 21 (2011) 3324–3334.

[52] Li, X. *et al.* *Nano Letters*, 9 (2009) 4268–4272.

Another method of producing large quantities of graphene is to place graphite in a solvent and apply ultrasound to the liquid. The ultrasonic vibration breaks up the graphite so a

distribution of thicknesses is obtained and remain in suspension. Centrifugation of the solution allows selection of the thinnest flakes. This method is used for many other layered crystals also[53].

Two other methods are worth mentioning. Firstly the growth of graphene on the surface of silicon carbide (SiC)[54]. At elevated temperatures, the carbon atoms are mobile enough to escape the lattice to the surface where they form epitaxial graphene. This has various uses, partly because SiC is a semiconductor and so devices can be formed directly on SiC wafers[55]. Secondly, graphene can be obtained by reducing graphite oxide. Graphite oxide is a long studied material which has the structure of graphite but with an increased c-axis constant because many carboxylic, epoxy and hydroxyl groups are bound to carbon atoms and sit between the layers. Expansion and reduction of the graphite layers allows graphene to be obtained[56]. The removal of the molecular groups tends to leave the resultant graphene with a high proportion of defects[57] but can still be useful for many applications such as membranes[58]

[53] Coleman, J. N. *et al.* *Science*, 331 (2011) 568–571.

[54] Emtsev, K. V. *et al.* *Nature Materials*, 8 (2009) 203–207.

[55] Hertel, S. *et al.* *Nature Communications*, 3 (2012) 957.

[56] Park, S. & Ruoff, R. S. *Nature Nanotechnology*, 4 (2009) 217–224.

[57] Gómez-Navarro, C. *et al.* *Nano Letters*, 10 (2010) 1144–1148.

[58] Nair, R. R. *et al.* *Science*, 335 (2012) 442–444.

1.5 Two-dimensional crystal heterostructures

Most of the results presented in this thesis focus on devices comprising several different crystal layers, fig. 1.13. The idea of two-dimensional crystal heterostructures has been developed in the last few years as technological expertise has allowed the precise and clean transfer of these crystal layers onto one another. Heterostructures have a long and rich history in semiconductor physics, leading to observation of interesting phenomena such as Coulomb drag and resonant tunnelling and led to technologies such as quantum well lasers.

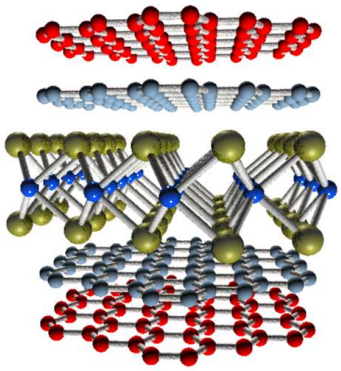

Figure 1.13: Cartoon of a two-dimensional a crystal based heterostructure comprising layers of graphene, hBN and WS_2.

However, while these heterostructure systems (typically III-V semiconductor materials) have the advantage that they can be grown directly on one another by very clean methods such as molecular beam epitaxy, the growth techniques can limit the possibilities. The samples produced by transferring crystal flakes onto each other allows an almost inexhaustible catalogue of devices by varying composition, doping and thickness, which can be chosen with atomic vertical precision. The aim is that functional devices, both including and beyond those presented here, will be fabricated and that they can compete with existing technologies in a broad range of application areas. A drawback of this technique is that subsequent layers are unlikely to have rotational or translational alignment as is present in epitaxially grown crystals for instance. The experimental chapters of this thesis discuss various such heterostructures and their properties and applications but first a chapter describing the experimental

techniques is presented.

Chapter 2

Experimental Techniques

In this chapter the general principles behind the experimental equipment and techniques used over the course of this research will be outlined. The opening sections will describe the use of scanning probe techniques and electronic transport measurements. Subsequently a brief explaination of how Raman spectroscopy was used and the ability to locally map photocurrents generated in graphene heterostructures will be given.

2.1 Atomic Force Microscopy

Atomic force microscopy has been utilised for several parts of this thesis so it is useful to give an overview of its mechanism and related techniques. AFM has been primarily used as an imaging tool to investigate surface contamination and roughness as well as to determine the thickness of thin crystallites. The field of scanning probe microscopy (SPM) was born with the inventions of the first scanning tunneling microscope[1] (STM) and atomic force microscope[2] (AFM) in the 1980s. In all cases SPM techniques involve measuring physical properties with a very fine, needle like probe close to the sample surface. The major strengths of SPM techniques are as follows.

1. The high lateral resolution means many different properties can be measured on very local scale, ∼10 nm or better with modern probes.
2. The high vertical resolution, which can be below 1 Å, means surface topography can be measured with high accuracy–important for investigating surface properties.
3. There is a large degree of flexibility in the measured properties; mechanical, electrical, magnetic and optical to name a few.
4. SPMs can be used invasively to perform lithographic patterning[3] and even manipulation/arrangement of single molecules[4].

[1] Binnig, G. & Rohrer, H. *IBM Journal of Research and Development*, 30 (1986) 355–369.

[2] Binnig, G., Quate, C. F. & Gerber, C. *Physical Review Letters*, 56 (1986) 930–933.

Manufacturer	Veeco
Microscope	Multimode
Controller	Nanosocpe IIIa
Modes	TM-AFM, CM-AFM, STM
Scanner range	1 µm, 5 µm, 100 µm

Table 2.1: DI AFM specification.

[3] Masubuchi, S. *et al. Applied Physics Letters*, 94 (2009) 082107.

[4] Gomes, K. K. *et al. Nature*, 483 (2012) 306–310.

Atomic force microscopy has become a widely used tool in investigations of material surfaces on the nanoscale. Graphene is by

definition entirely composed of surface and AFM is a tool that has been widely used in graphene research. Most commonly, AFM is used to image surface topography but quantitative measurements can be made; mechanical properties of graphene such as stiffness[5] and friction[6] have been investigated with these techniques for instance. Another important technique is conductive AFM where a probe is used to locally map conduction of a sample. This section will first introduce the ideas and concepts behind AFM and then explain how these quantitative measurements can be made.

[5] Lee, C. *et al. Science*, 321 (2008) 385–388.

[6] Lee, C. *et al. Science*, 328 (2010) 76–80.

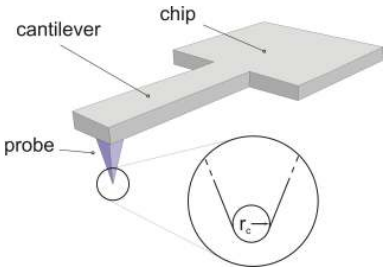

Figure 2.1: Sketch of an AFM probe showing the tip's radius of curvature r_c.

The general idea behind AFM is that a needle like probe–see fig. 2.1–with a very sharp tip is brought into contact with the surface of a sample and scanned over the surface by use of a piezoelectric motor. The sample-probe interaction can be measured and the height of the tip is usually adjusted accordingly to maintain a constant interaction force; this can be interpreted as the surface topography. The technique and apparatus allow measurement of very localised forces and so samples can be mapped with a resolution in the subnanometer range in the vertical dimension and better than 10 nm in the lateral dimension. The precision in the lateral dimension is limited by the probe's radius of curvature, see fig. 2.1. Two common scanning methods are used, described in the following section, but both follow a similar premise.

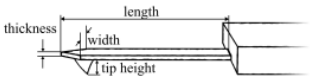

Figure 2.2: Sketch of an atomic force microscopy probe, detailing the various dimensions. width ∼30 µm, thickness ∼5 µm, length ∼100-500 µm and tip height ∼10-15 µm.

The probe is mounted on a cantilever and positioned above the sample. A laser beam is incident on the cantilever and the reflected light detected by a four-piece photodiode. This gives the four signals labelled A, B, C and D in fig. 2.3 and their relative proportions depend on the laser spot position and hence the cantilever motion can be deduced. These variations are mapped as a function of lateral position and hence local information is revealed about the sample surface.

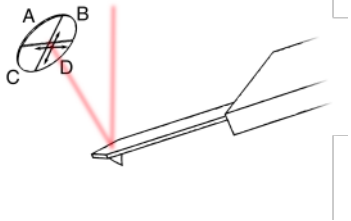

Figure 2.3: Sketch the laser beam deflecting onto the quadrant photodiode.

2.1.1 Tapping-Mode AFM

The most common method used to detect the interaction force is variations in an oscillating cantilever's amplitude as it is scanned over the sample, see fig. 2.4. This is referred to as tapping-mode AFM (TM-AFM) because the probe is repeatedly tapping on the surface.

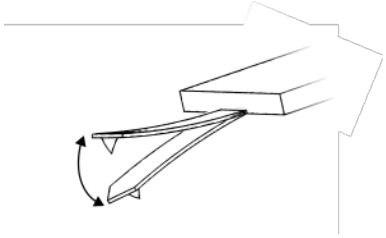

Figure 2.4: Sketch of tip oscillation in tapping-mode AFM.

The equation of motion of a damped, driven cantilever has a term dependent on the probe-sample interaction and thus the system's resonant frequency is dependent on this force.

$$m\frac{d^2z}{dt^2} = -k_c z - \frac{m\omega_0}{Q}\frac{dz}{dt} + F_0\cos(\omega t) + F(z) \qquad (2.1)$$

where the parameter definitions are given in table 2.2. The tip vibration leads to an oscillating output voltage of the photodiode and the amplitude is tracked as the probe is scanned across the surface and encounters regions of varying height. A feedback loop keeps a constant probe-surface distance by maintaining a constant oscillation amplitude. If the height increases the probe-sample force will increase and the probe will be retracted to compensate. In the simplest case, a trace of the probe's path is interpreted as the topography of the sample.

Symbol	Parameter
m	mass
z	vertical position
t	time
k_c	spring const.
ω_0	resonant frequency
Q	quality factor
F_0	driving force amplitude
$F(z)$	probe-sample interaction force

Table 2.2

2.1.2 Step height measurement

One of AFM's main uses is height and lateral distance measurement because of the precision to which it can measure. In the lateral dimensions this is limited by the radius of the AFM probe $r_c \sim 10$ nm. In the vertical direction the accuracy of the microscope used is $\sim$1 Å. There are several ways to determine step heights, both of which are illustrated in figure 2.5. For demonstration purposes, the molecule pentacene which forms islands on SiO_2 is shown. Fig. 2.5**a** shows the height mapped ny TM-AFM as a function of both lateral dimensions and the entire image spans 10 µm. One can see the islands have discrete steps in height. Fig. 2.5**b** shows the distribution of height values from the map.

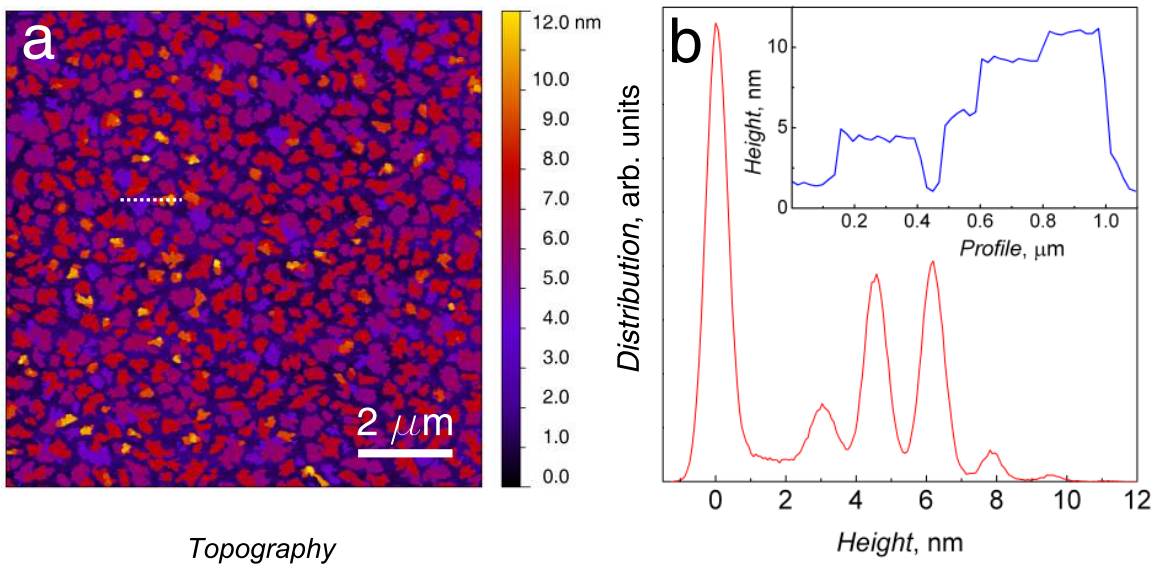

Figure 2.5: TM-AFM of pentacene on SiO_2. **a** The height of the pentacene islands mapped as a function of both lateral dimensions and the entire image spans 10 µm. Islands with discrete steps are visible. **b** The distribution of height values from **a**. The peaks in this plot give heights of the layers relative to the surface and can be used to get an accurate step height in the absence of contamination and image artefacts. The inset shows a line scan (indicated by the dotted white line) which is a more direct method to measure stepheight.

2.1.3 Phase imaging

Phase imaging with AFM is done by monitoring the phase shift between the driving voltage of the cantilever and the output voltage of the photodiode. This shift is related to the probe-sample interaction, in particular energy dissipation[7]. There is a shift in phase when the probe is near the sample surface and this phase shift will depend on the material. This is used to determine the boundary of one crystallite on the surface of another and its utility will be shown in chapter 3.

[7] Eaton, P. & West, P. *Atomic Force Microscopy*. Oxford University Press (2010).

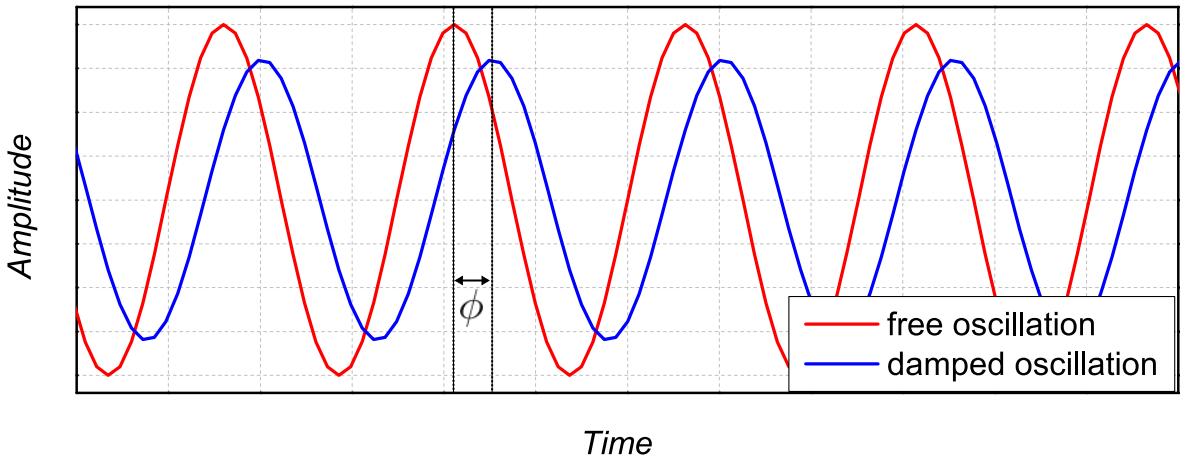

Figure 2.6: Example of the cantilever oscillation showing the phase when the cantilever to near and far from the surface. The phase shift is shown on the diagram.

2.1.4 Contact-Mode AFM

In contact-mode AFM (CM-AFM) the same setup is used only the oscillation of the cantilever is switched off and instead the deflection of the cantilever is used to determine the probe-sample force–as the tip is pushed into the sample, the cantilever will bend. Again, in regions where the sample is higher, a greater deflection of the cantilever will be observed and the probe height adjusted accordingly to maintain a constant interaction force. This mode of operation is much more sensitive to artifacts because of the greater lateral forces exerted between the probe and sample but means that friction and other adhesion properties can be determined.

Force measurement

One advantage of CM-AFM is that it is possible to control the force applied to the surface with a fair degree of precision. This is done by pushing the tip into the sample surface and measuring the resultant deflection of the cantilever. With knowledge of the cantilever's spring constant, it is possible to convert the deflection into a force. Thus by setting a certain deflection during scanning the force normal to the surface can be controlled. A typical curve is shown in fig. 2.7 where

deflection is plotted as a function of the vertical displacement, the black line denoting extension and the red line retraction. The ramp starts at (a) and the corresponding deflection remains zero until the sample is reached at (b) where contact is made and deflection begins. The deflection increases up to point (c) where the ramp direction is reversed. The deflection decreases again but becomes negative at point (b) as the tip remains in contact with the sample due to adhesion. At point (d) the restoring force of the cantilever overcomes the adhesion force and the deflection returns to zero. The stiffness of the cantilever determines the force for a set deflection: one can multiply the deflection by the known spring constant of the cantilever. Then the adhesion and loading forces can be determined. The loading force is that which will be applied to the sample during scanning.

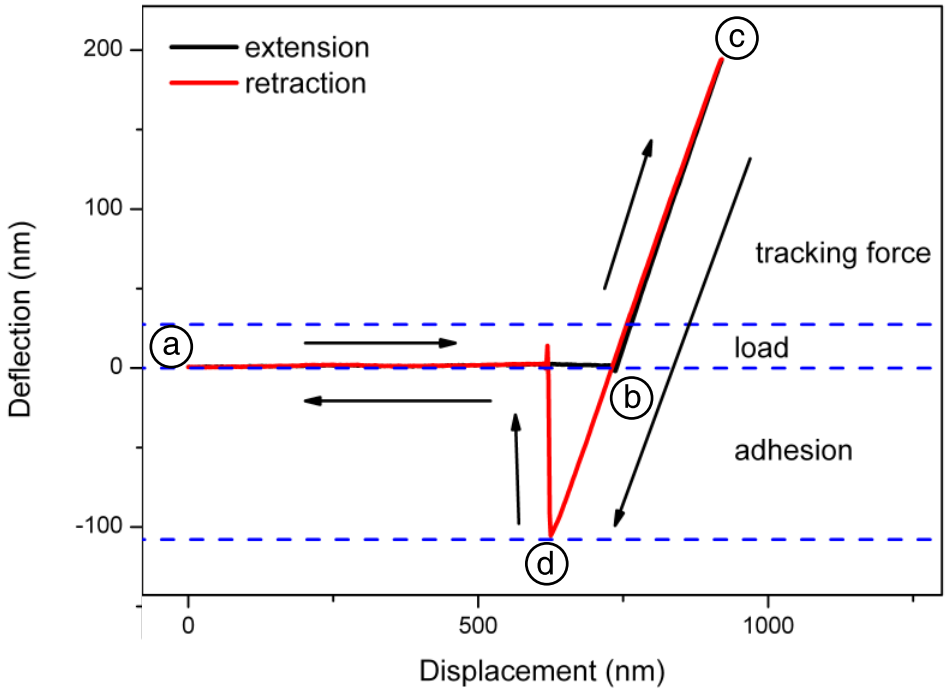

Figure 2.7: Example force-displacement curve. Initially the cantilever is unbent. From (a) the probe is moved closer to the sample and contact is made at (b) and deflection increases up to (c). From (c) the probe is retracted and the deflection becomes negative as the tip is adhered to the sample. At (d) the restoring force overcomes the adhesion force and the probe snaps out of contact.

2.1.5 Nano-indentation using atomic force microscopy probes

Another technique that is made possible by the precision of the atomic force microscope is indentation using the probe to measure mechanical properties of a sample[8]. Modern AFMs can do this whilst scanning but due to complications brought by geometric factors of the tip and sample, the interpretation of

[8] Radmacher, M. *Methods in Cell Biology*, 68 (2002) 67–90.

data can be difficult. A well defined system is easier to model and hence for these indentation experiments a circular aperture covered by graphene was used; the result being something akin to a drum. When the probe is driven into the centre of the membrane, both the cantilever and the membrane will take some of the strain. By measuring the deflection of the cantilever (inferred from the laser spot movement) the deflection of the membrane can be deduced. A cartoon schematic of such a process is shown in figure 2.8.

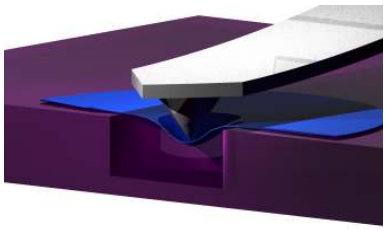

Figure 2.8: Indentation with an atomic force microscopy probe.

Membrane deflection

In order to determine the deflection of a membrane δ with indentation of an AFM probe it is necessary to compare a force-displacement curves taken on the membrane and an infinitely hard substrate–often SiO_2 is considered a suitable reference material. When the probe is forced into an infinitely hard substrate all displacement goes into bending the cantilever d. However, if the sample can be deformed then both the cantilever and membrane will become strained. The membrane deflection can be inferred by taking the difference between the probe displacement and the cantilever deflection.

$$\delta = z - d \tag{2.2}$$

An example of indentation of trilayer graphene covering holes etched in silicon oxide is shown in fig. 2.9, where the measured force is plotted as a function of the indentation depth. The contact occurs at point **A** and the membrane is indented up to point **B** at which point the bottom of the hole is reached and the increasing force results in no further indentation. 3D AFM images of a partially covered hole, taken before and after indentation, are shown in fig. 2.10. After indentation the graphene membrane becomes adhered to the bottom of the pit.

Following the model given by Lee *et al.*[9] we can determine the Young's modulus of the graphene sheet by fitting the force-indentation curve with

$$F = \sigma_0^{2D}(\pi a)\left(\frac{\delta}{a}\right) + E^{2D}(q^3 a)\left(\frac{\delta}{a}\right)^3 \tag{2.3}$$

where σ_0^{2D} is the membranes pretension, a its diameter, E^{2D} its Young's modulus and q the Poisson's ratio of graphite (taken from Lee *et al.*[10]). Fitting the curve with σ_0^{2D} and E^{2D} as fitting parameters allows the Young's modulus to be determined as 890 N/m.

With a bottomless hole, the membrane will fracture at a certain

[9] Lee, C. *et al. Science*, 321 (2008) 385–388.

[10] Lee, C. *et al. Science*, 321 (2008) 385–388.

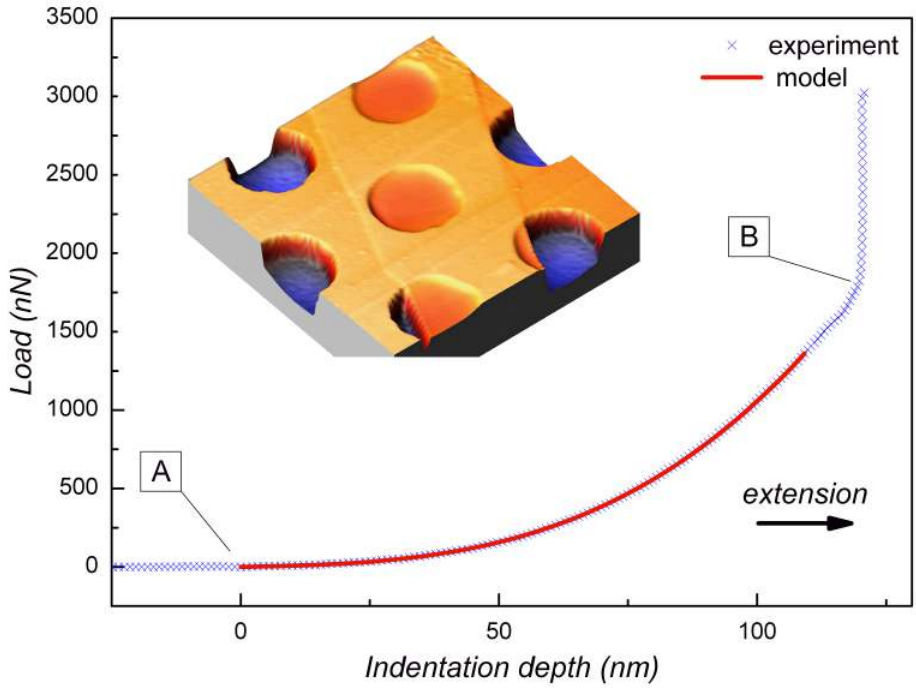

Figure 2.9: A force-indentation plot for trilayer graphene covered holes in SiO_2. The contact occurs at point **A**, the membrane is indented up to point **B** at which point the bottom of the hole is reached and the increasing force results in zero indentation. The inset is a 3D representation of the graphene covered holes.

force allowing determination of the fracture strain. Using this technique, the fracture strain of fluorographene was measured and is presented in appendix B. Crucially, this fracture force is heavily dependent on the tip radius[11]: the sharper the tip and lower the required force. In order to make a comparison between fluorographene and pristine graphene the same tip was used for all membranes and was not seen to be dependent on order of the measurements suggesting the tip was not degrading with repeated indentation measurements.

[11] Lee, C. *et al.* *Science*, 321 (2008) 385–388.

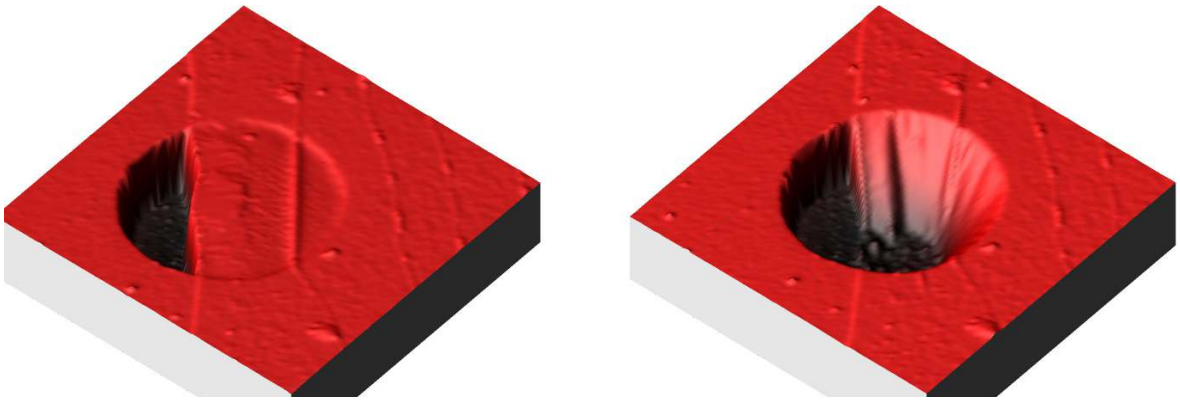

Figure 2.10: Indentation of a trilayer graphene membrane. The left and right hand panels show TM-AFM images taken before and after indentation respectively. After indentation it is seen that the graphene has become adhered to the botton of the hole.

2.1.6 Conductive AFM

Another quantitative measurement technique that is possible with CM-AFM is conductive AFM (C-AFM), where the probe is covered with a conductive coating; gold and platinum/iridium coating are commonly used. The Au coatings were produced by evaporation of Au onto Si probes, giving a relatively large contact area. The Au tipped probes allowed low contact resistance because of their size and the fact that Au can be deformed, even under the low forces during operation, further increasing the contact area. The Pt/Ir probes were purchased precoated and generally gave higher resistance but could be used to measure with a higher lateral resolution because of the strength of the coating.
C-AFM is particularly useful for investigating the homogeneity of a sample's conductivity. Presented as part of chapter 3, are results on the homogeneity of few-layer boron nitride revealing a very uniform tunnelling current when a bias voltage is applied between the probe and a graphite electrode lying underneath the few-layer hBN.

The experimental setup that was used is shown in fig. 2.11. The AFM has been modified by attaching a wire directly to the tip holder to allow a voltage V_b to be applied between probe and sample. The voltage was applied by a Keithley 2400 Sourcemeter and the current I measured by recording the voltage drop across a load resistor of known resistance placed in series with the sample, this measurement was made with a Keithley 2182A Nanovoltmer. This signal could then be fed into the microscope controller to be registered alongside the topography image. The voltage source was controlled by a Labview program which also allowed recording of $I(V_b)$ characteristics; to check for ohmic conduction between probe and sample for example.

2.2 Basic electronic transport in graphene

Electronic transport is heavily studied in graphene research, with various reviews of the topic[12,13]. In this section, the measurement conventions will be outlined to ease the discussion of the results given in the later sections. The details will be basic and more aligned to understanding the terminology of the measurements.
With reference to fig. 2.12, the measured quantities are the current I that's flowing between two terminals and their potential difference V. The conductivity σ of a two-dimensional sample with a width w and length l is given by $\sigma = \frac{I}{V}\frac{l}{w}$. In the

[12] Neto, A. H. C. *et al.* *Reviews of Modern Physics*, 81 (2009) 109–162.

[13] Sarma, S. D. *et al.* *Reviews of Modern Physics*, 83 (2011) 407–470.

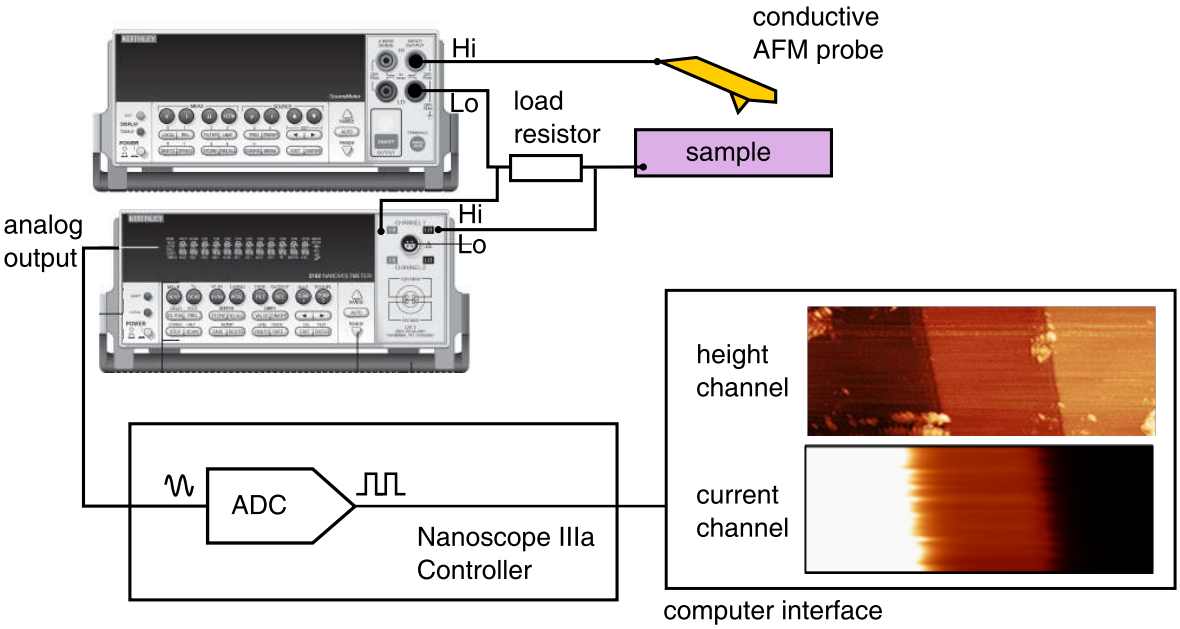

Figure 2.11: Conductive atomic force microscopy setup. A voltage is applied between probe and sample by a Keithley 2400 Sourcemeter and the current measured by recording the voltage drop across a resistor of known value with a Keithley 2182A Nanovoltmeter. The current signal can be fed into the microscope controller to be read alongside the other AFM data.

simplest case, considering the delocalised electrons in graphene to behave as in a metal one can use the Drude model[14] which gives the constant of proportionality between the current density $|\mathbf{j}| = I/w$ and and electric field $|\mathbf{E}| = V/l$ across a region of the material as the conductivity σ.

[14] Ashcroft, N. W. & Mermin, N. *Solid State Physics*. Harcourt Brace (1976).

$$\mathbf{j} = \sigma \mathbf{E} \tag{2.4}$$

where

$$\sigma = ne\mu \tag{2.5}$$

where μ is the charge mobility and n the charge carrier density (in units of inverse area in 2D). By measuring how the conductivity of the system changes with carrier density, it is possible to determine the mobility of the charge carriers, see fig. 2.14. The charge carrier mobility is an important parameter because it is a quantitative measure of the quality of a given device. The high mobility is one reason why there has been much interest in graphene as, in principle, it allows devices to work at high frequencies; important for increased performance of electronic components such as transistors. In principle, measurements can be made in any geometry but to ease interpretation of results most samples shown in the later chapters will have a standard device design, see fig 2.12. In order to measure mobility both the conductivity and the carrier density need to be determined. To measure conductivity, a current is passed

between the two end contacts while the voltage is measured between any combination of electrodes inbetween. The voltage is either labelled V_{xx} or V_{xy} depending on whether the voltage is measured parallel or perpendicular to the current flow. These two values allows us to determine the in-plane conductivity values σ_{xx} and σ_{xy}.

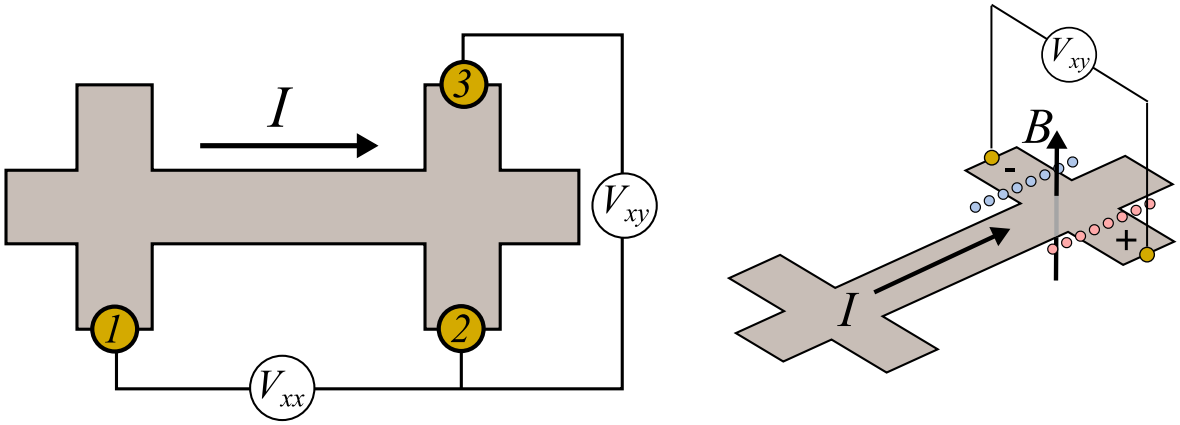

Figure 2.12: Measurement conventions in a 2D sample. **a** A current is passed between the two end electrodes and the parallel and perpendicular voltages measured V_{xx} and V_{xy} respectively. **b** if a magnetic field is applied, the charges of opposite sign build up on either side giving a finite V_{xy}.

Carrier density can be varied by electrostatic gating which moves the chemical potential in graphene. In the absence of magnetic field $|\boldsymbol{B}|$, V_{xy}=0 as there is no net force perpendicular to the current flow. However, in a magnetic field oriented out of (or into) the plane of the sample, the Lorentz force pushes electrons towards one edge giving a finite V_{xy}. The well-known Hall effect $V_{xy} = -\frac{I|\boldsymbol{B}|}{ne}$ allows determination of both the sign of the charge carriers ($\pm e$) and their density as functions of gate voltage, see fig. 2.13. One can see from the plot shown in fig. 2.14 that by measuring how σ changes with n, the mobility can be determined: $\mu = \frac{1}{e}\frac{\delta\sigma}{\delta n}$.

Measurements in graphene are often done in vacuum to eliminate the effects of doping from contaminants present in air, e.g. water molecules. This is not essential but hysteresis tends to be unavoidable in measurements done in ambient conditions. There is also unavoidable doping due to the substrate but in most samples this leads to a hysterisis on the order of a few mV in V_g.

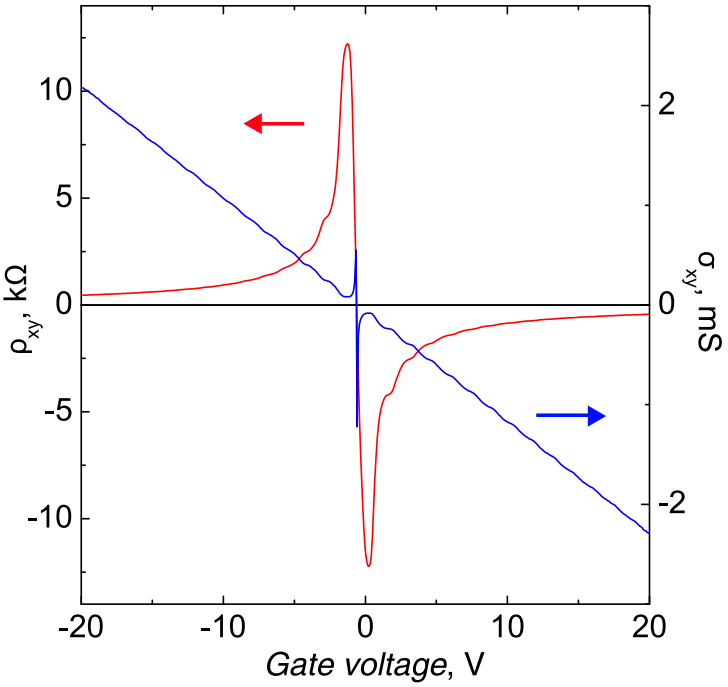

Figure 2.13: The Hall effect in graphene in a magnetic field of 2.8 T. The red curve is the Hall resistivity ρ_{xy} and the blue curve is the Hall conductivity $\sigma_{xy} = \frac{1}{\rho_{xy}}$. A linear fit to σ_{xy} determines the carrier concentration $n(V_g)$.

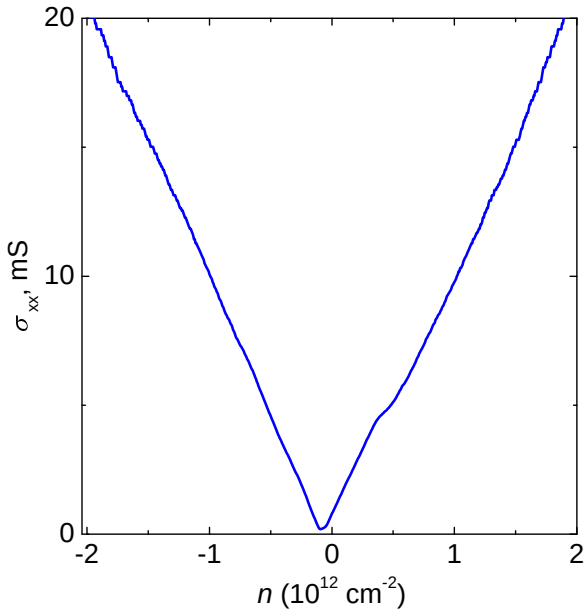

Figure 2.14: Conductivity of graphene as a function of carrier concentration. A linear fit of the conductivity gives the mobility $\mu = \frac{1}{e}\frac{\delta\sigma}{\delta n}$, from equation (2.5)

2.3 Raman Spectroscopy

Manufacturer	WITec
Excitation energies	1.96, 2.41, 2.54 eV
Spot size	∼500 nm
Grating	600, 1800 mm^{-1}
Resolution	3, 1 cm^{-1}
Spectrometer	1024x127 px Si CCD
Spectrometer temperature	222 K

Table 2.3: WITec Raman specification.

Raman spectroscopy is a technique used to study vibrations and rotations of molecules. In crystals Raman spectroscopy probes vibrations of the lattice. A photon can excite electrons in a material by absorption which in turn can interact with phonons. When the electrons drop back to lower energy states they can re-emit light at a different energy to the excitation. Looking at this inelastically scattered light, one can infer what processes have occurred in the sample. There is a long history of Raman spectroscopy in carbon research: graphite and nanotubes particularly. It has also proved a particularly useful tool in graphene research as it allows chracterization of strain[15], doping[16] and chemical modification[17] among other properties. Furthermore, because graphene is composed entirely of surface atoms, where all are equally influenced by enviromental changes, Raman spectroscopy allows observation of relatively small changes.

[15] Mohiuddin, T. M. G. *et al.* *Physical Review B*, 79 (2009) 205433.

[16] Das, A. *et al.* *Nature Nanotechnology*, 3 (2008) 210–215.

[17] Dresselhaus, M. S. *et al.* *Graphene nanoelectronics Chapter 2: Raman spectroscopy: Characterization of edges, defects, and the Fermi energy of graphene and sp^2 carbons.* Springer (2012).

The technique involves shining monochromatic laser light onto the sample and inspecting the spectrum of the light that comes back. While most of the light is elastically scattered, i.e. it has the same energy as the incident light, a small proportion (∼1 in 10^6) undergoes a Raman scattering process and loses (or gains) energy as a result. These processes are very dependent on the state of the material and thus a lot of information can be garnered by studying the resulting spectrum. The entire Raman cycle must fulfil both momentum and energy conservation which restricts the possible modes which can be excited. Graphene has several distinct peaks in its spectrum; the most important of which are the so-called G, 2D (or sometimes G′) and D peaks. The latter is a defect activated peak, meaning it is only seen when the sample has deviations from a perfect crystal lattice.

One reason why Raman spectroscopy is particularly useful in graphene research is that it is able to quickly distinguish between mono-, bi- and few- layer graphene without damage to the sample[18]. This is shown in fig. 2.15 where the 2D peak is shown for thicknesses of graphene from monolayer to graphite. In graphene there is only one scattering process that fulfils the right conditions so a single transition is seen; the peak can be fitted with a single Lorentzian line shape. With the addition of another layer, the number of allowed processes is four-fold, each with a slightly different energy. This leads to a more complex line shape which can be fitted with four Lorentzian peaks. For more layers, even more transitions are allowed but the separation in energy is not enough to unambiguously distinguish

[18] Ferrari, A. C. *et al.* *Physical Review Letters*, 97 (2006) 187401.

the number of layers in thicker samples. Measuring the width of the 2D peak is an easy way to distinguish monolayer from thicker flakes.

Other crystals such as WS_2 and MoS_2 have thickness dependent peak positions which can be used to determine the number of layers for thin samples[19,20].

Raman spectroscopy is also able to determine the concentration of defects in graphene by the appearance of the D peak and its ratio to the G peak[21]. It is even possible to distinguish the type of defect, whether it be vancancies or covalently bonded adatoms[22]. This was utilised to test the level of fluorination in graphene membranes when measuring their fracture strain and is presented in appendix B. Fig. 2.16 shows the Raman spectra of both pristine and partially fluorinated graphene. One can see the presence of three extra peaks in the spectrum: the D peak occurring at $\sim$1340 cm^{-1}, D′ at $\sim$1630 cm^{-1} and a combination mode at $\sim$2940 cm^{-1}

[19] Gutiérrez, H. R. *et al.* *arXiv:1208.1325*, (2012).

[20] Li, H. *et al.* *Advanced Functional Materials*, 22 (2012) 1385–1390.

[21] Dresselhaus, M. S. *et al.* *Philosophical Transactions of the Royal Society*, 368 (2010) 5355–5377.

[22] Eckmann, A. *et al.* *Nano Letters*, 12 (2012) 3925–3930.

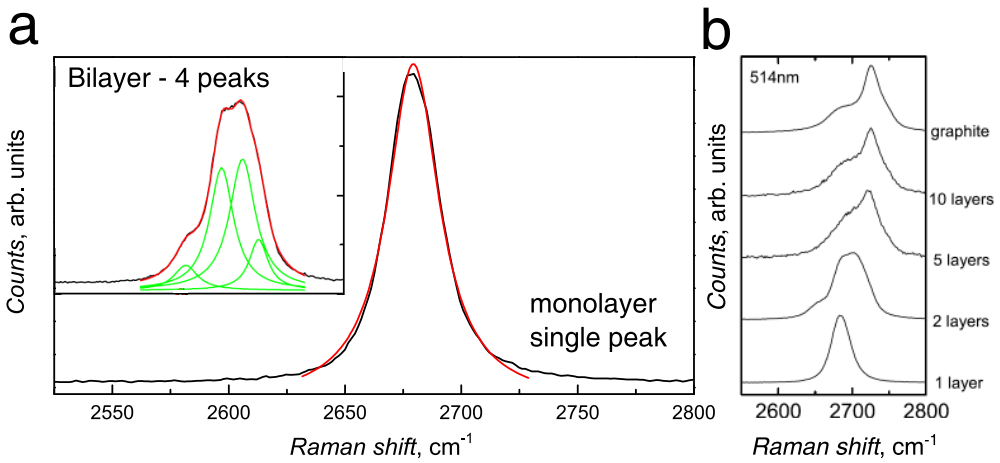

Figure 2.15: Raman spectra of mono- and bi- layer graphene. **a** The Raman spectrum of pristine graphene monolayer 2D peak showing it can be fitted with a single Lorenztian peak. The inset shows the Raman spectrum of bilayer graphene. **b** The evolution of the 2D peak for increasing number of graphene layers. All spectra are measured with a 2.41 eV laser. This figure is adapted from Ferrari *et al.*[a].

[a] Ferrari, A. C. *et al.* *Physical Review Letters*, 97 (2006) 187401.

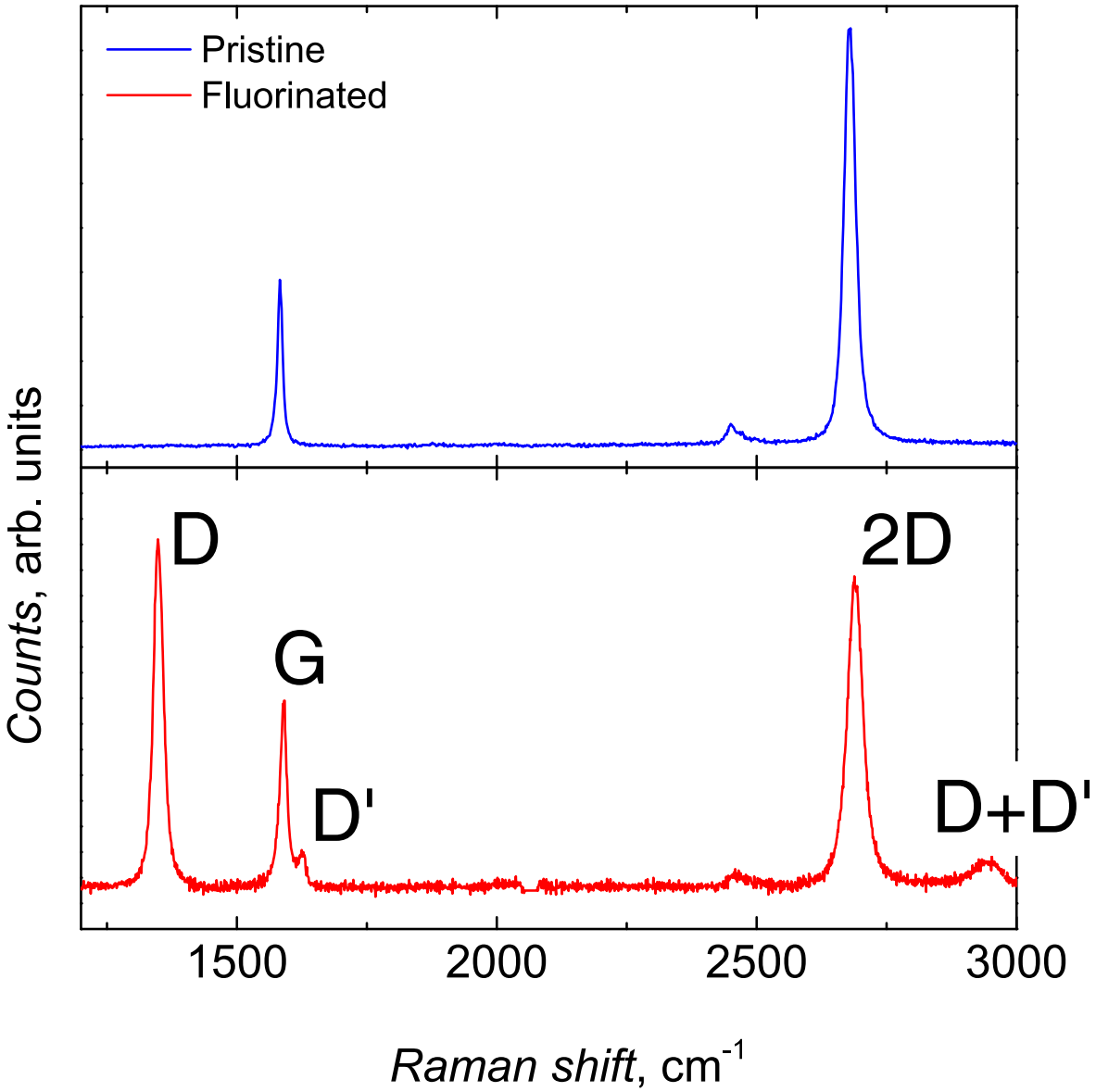

Figure 2.16: With a 2.4 eV excitation laser, the characteristic peaks of pristine graphene are the G located at ∼1580 cm^{-1}, and the 2D located at ∼2680 cm^{-1}. In the prescence of defects (e.g. atomic vacancies), further features are observed, the D peak at ∼1340 cm^{-1}, D′ at ∼1630 cm^{-1}, and combination mode D + D′ at ∼2940 cm^{-1}.

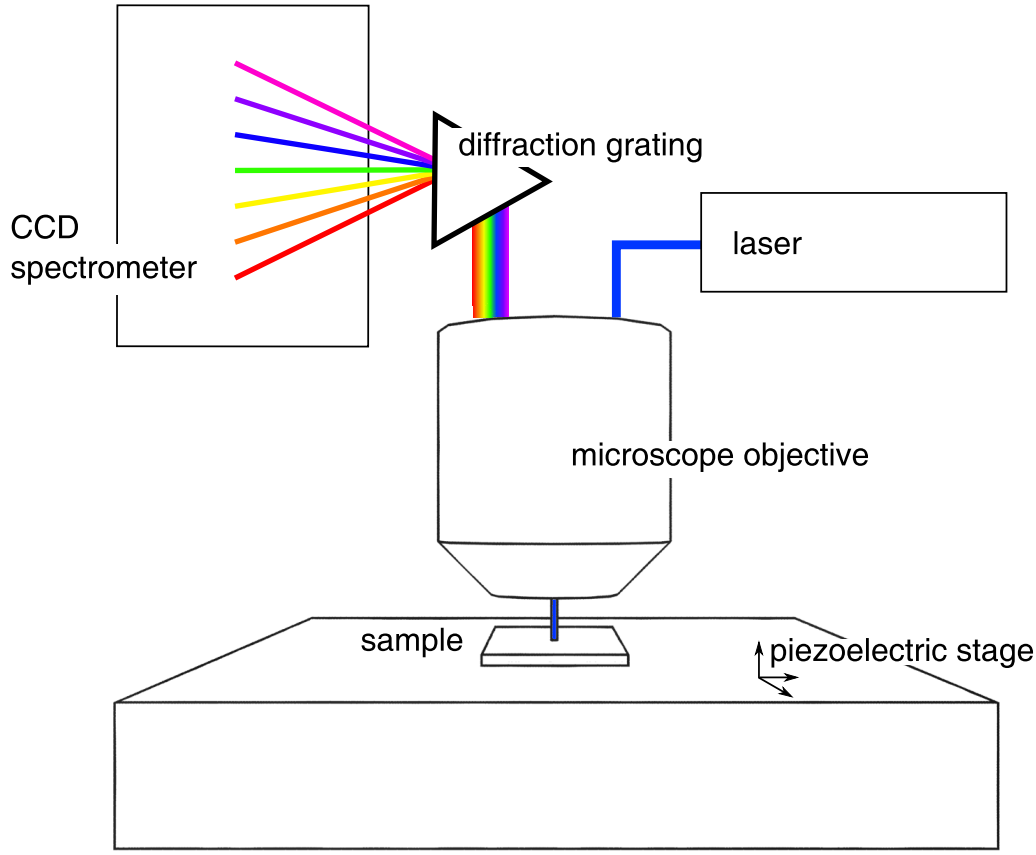

Figure 2.17: The experimental setup of the WITec scanning Raman spectoscopy apparatus.

The Raman spectroscopy setup is shown in fig. 2.17. Laser light is coupled to the microscope objective where it is focused on to the sample. The scattered light is collected by the same objective and directed onto a diffraction grating. This splits the light up by wavelength and it is projected onto a CCD spectrometer for the spectrum to be recorded. The sample sits on a piezoelectric stage so Raman spectra can be accurately recorded as a function of position. In all measurements, the laser power was measured prior to and after measurement. This was to ensure that no damage would be induced by laser heating. From experience, a power density of 500 µW µm^{-2} is small enough to ensure that no changes to the spectrum were observed after long exposure times. However, a small D peak on the order of 1% is always observed in graphene, giving the concentration of defects ~1:10^8 in pristine graphene[23].

[23] Ni, Z. H. *et al.* *Nano Letters*, 10 (2010) 3868–3872.

2.4 Scanning photocurrent microscopy

A further extension of the experimental setup is that additional analog-digital converters (ADC) in the controller allow external signals to be recorded alongside the Raman spectra. If a sample produces a photovoltage when illuminated and is electrically

contacted, the signal can be mapped as a function lateral position, simultaneously with Raman spectra; together a powerful tool.

This technique, known as scanning photocurrent microscopy, has been utilized to map photovoltages in many structures. With reference to graphene, it can give important information about doping of graphene by other materials such as metal contacts because the sign and magnitude of the voltage is dependent on the pn junction created in graphene at the interface. In general, the low density of states in graphene means that when it contacts a material with a different work function, the charge flow is primarily into or out of graphene[24]. This leaves a voltage drop at the interface which can separate electron-hole pairs created in the region by incident photons[25].

An example of this is shown in figure 2.18. A piece of graphene is placed on an oxidised silicon wafer and a thin MoS_2 flake transferred to its surface. Doping from the MoS_2 on the graphene creates regions of different doping. Electrons excited by the laser flow in the resultant electric field and a signal can be measured.

[24] Giovannetti, G. *et al.* *Physical Review Letters*, 101 (2008) 026803.

[25] Lee, E. J. H. *et al.* *Nature Nanotechnology*, 3 (2008) 486–490.

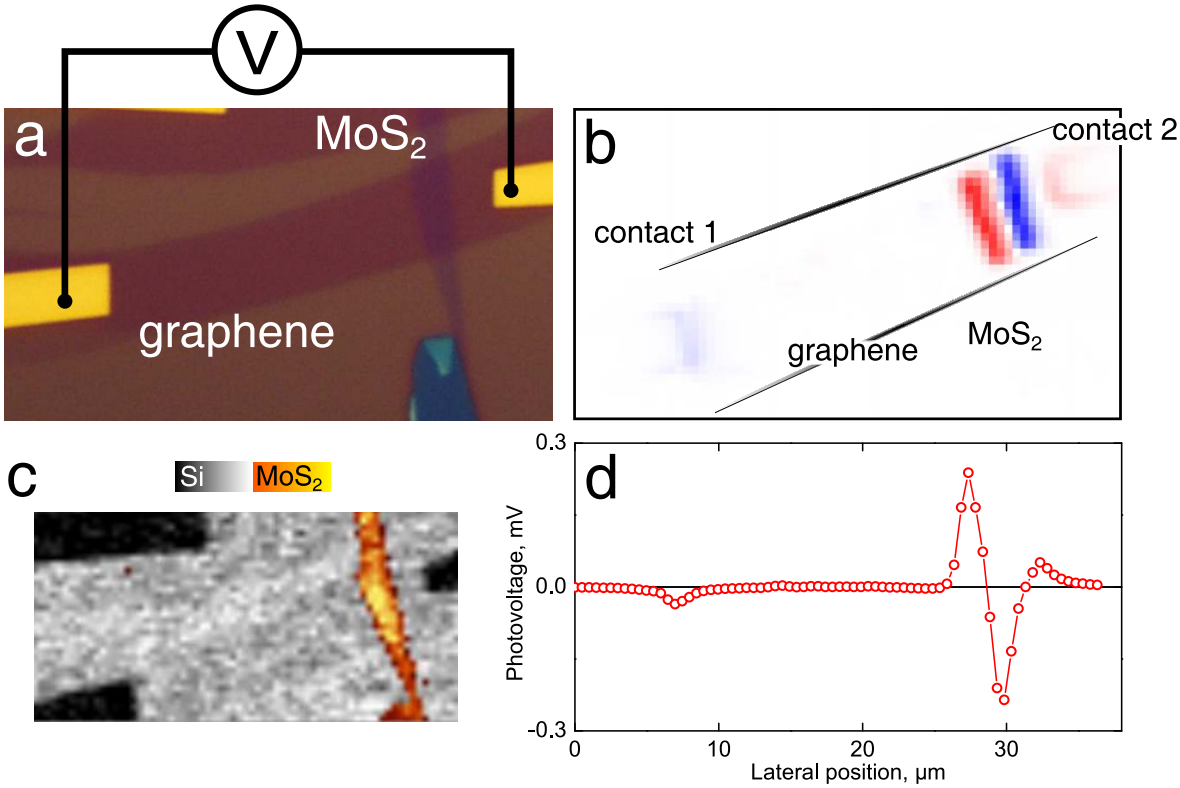

Figure 2.18: Photovoltage map of MoS_2 on graphene. **a** An optical image of the device where the a voltage is measured between the electrodes shown. **b** Photovoltage map, strong signal's observed where MoS_2 overlaps graphene and smaller signal at contacts. **c** Combined Raman map showing the intensity of the Si peak in greyscale and MoS_2 in orange. **d** Linescan taken across the photovoltage map from contact 1 to contact 2.

This technique has been used to study the generation of photocurrent in graphene/WS_2 heterostructures and is presented in chapter 6.

Part II

Experimental results

Chapter 3

Electron Tunneling through Ultrathin Boron Nitride Crystalline Barriers

The insulating two-dimensional material hBN has been used as an tunnel barrier between various metallic materials: gold, graphite, graphene or a combination thereof. The tunnel current follows an exponential dependence on number of layers with an exponent of 1.5 decades per hBN layer. Furthermore, conductive atomic force microscopy showed a high degree of homogeneity in the tunnel current across hBN terraces making it suitable as a large area tunnel barrier. The work presented in the following chapter has been published in Nano Letters[1]*. My contribution to this work entailed making the AFM, C-AFM and electronic transport measurements, analysing the data and implementing the model.*

[1] Britnell, L. *et al. Nano Letters*, 12 (2012) 1707–1710.

3.1 Introduction and motivation

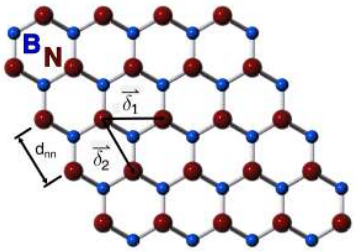

Figure 3.1: The crystal structure of hexagonal boron nitride, view parallel to the *c*-axis. The lattice bonding is primarily ionic because of the difference in electron affinity.

Graphene possesses many great qualities–as discussed in chapter 1–but in terms of developing applications, it is advantageous to explore other materials and their suitability in combination with graphene. More complex systems can be found by artificially reconstructing the third dimension; this is done by layering graphene with other 2D crystals into heterostructures resulting in similar devices to semiconductor heterostructures such as gallium arsenide. With the characterisation of such structures being the goal, it is necessary to assess the quaility and suitability of the constituent parts. One potential material is hexagonal boron nitride (hBN), see section 1.2.1. It has the same crystal structure as graphene but with the carbon atoms on the A and B sublattices replaced by boron and nitrogen atoms respectively. This symmetry breaking leads to a large bandgap on the order of ∼6 eV [2] and hence bulk hBN is a good insulator. This is further aided by its high purity and low chemical reactivity.

[2] Watanabe, K., Taniguchi, T. & Kanda, H. *Nature Materials*, 3 (2004) 404–409.

With the aim of building graphene/hBN heterostructures, a series of experiments were undertaken to confirm that hBN

would be a suitable material to use. Thin flakes of hBN were placed on conductive substrates; either graphene, graphite or Au, by our standard transfer procedure–see chapter 1 and section 3.9 at the end of this chapter. To measure the conduction parallel to the c-axis of hBN, a further top contact was made. This was done again, either by transfer of another graphene or graphite flake or by lithographically patterned Au contacts. In order to investigate the homogeneity of the samples and structural integrity following transfer, an Au or Pt/Ir coated AFM probe[3] was used as a top contact and measurements made by conductive AFM.

[3] The Au coated tips were fabricated by evaporating a 5/20 nm Cr/Au film onto standard doped Si probes by e-beam evaporation. The Pt/Ir probes were purchased from Nanosensors, the Pt/Ir probes giving a good combination of conductivity and stiffness.

At every fabrication step, the samples were annealed up to 300°C in a H_2/Ar gaseous mixture to remove contamination such as poly(methyl methacrylate) accumulated during the processing steps. The dependence of current on applied bias between the top and bottom contacts was measured over a range of samples and it was determined that hBN was of high quality over micron scale areas making it perfectly suitable for use in more advanced heterostructure devices. Also investigated was the dependence of the current on the thickness of the hBN film, from one to four atomic layers.

In the following sections the main results from the experiments are presented. First, the process of determining the number of hBN layers and electrode overlap in a sample is given. This is followed by a discussion on the effect of the number of boron nitride layers on the current flow under the applied bias between different electrodes. The behaviour is shown to follow the Simmons model of quantum mechanical tunnelling. The final section describes how conductive AFM was utilized in examining the local tunnel current flow across hBN terraces.

3.2 Determination of number of hBN layers

In order to compare the $I(V_b)$ curves for different samples it was necessary to determine the number of layers in any given sample. The results from AFM topography and optical contrast[4] were cross correlated to ensure a reliable result[5].

[4] see appendix A

[5] Gorbachev, R. V. *et al.* *Small*, 7 (2011) 465–468.

3.2.1 Atomic force microscopy

The method described in section 2.1.2 was used to determine the number of hBN layers from AFM topography images. Shown in fig. 3.2 is an example of a few layer hBN on the surface of graphite. The topography image is shown in the middle

panel with the corresponding height distribution in the top panel and a line scan in the bottom panel. The height distributionl has been fitted with 7 Gaussian functions to reconstruct the data and the difference between the centres of subsequent peaks is plotted in the inset where the dotted lines indicate the thickness of 1-3 layers of hBN using the bulk interlayer distance 3.4 Å, the error bar is from the nominal ±1 Å error of the AFM. A comparison of this with the line scan (averaged over 10 lines) means we can assign the thickness of layers as labelled on the topography image. The phase shift θ between the drive and detection voltages in TM-AFM can be used to find the perimeter of the hBN flakes when on graphite, where terraces within graphite can be confused with those in hBN. The interaction between the probe and sample material dictate θ, thus when crossing a boundary between graphite and hBN, a distinct change in θ commonly observed. An example of this is shown in fig. 3.3, where **a** shows a TM-AFM height image and **b** the corresponding phase image. The graphite lies on the left of the image and the terraces visible on the right are hBN. In the phase image this boundary is clearly seen. In cases where the boundary is difficult to find, this is a convenient method to find it.

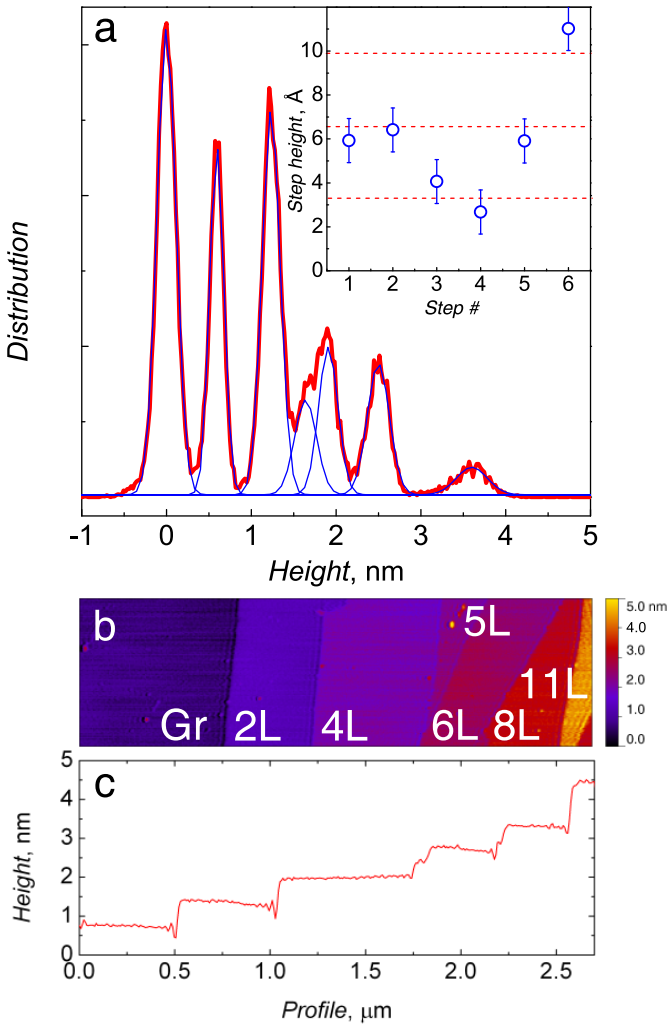

Figure 3.2: **a** The height distribution of the topography image shown below in **b**. The distribution is fitted with 7 Gaussian functions, the centres of which give the heights of the hBN terraces relative to the graphite surface. The inset shows the difference between subsequent peaks with the 1 Å error of the microscope, the dotted lines represent the thicknesses of 1-3 atomic hBN layers using the bulk c-axis lattice constant. **b** The TM-AFM topography image with the determined hBN thicknesses labelled: Gr for graphite and NL for number of hBN layers relative to the Gr height. **c** A 10 line averaged linescan taken across the width of the topography image, the step heights are correlated with the height distribution to determine layer thickness.

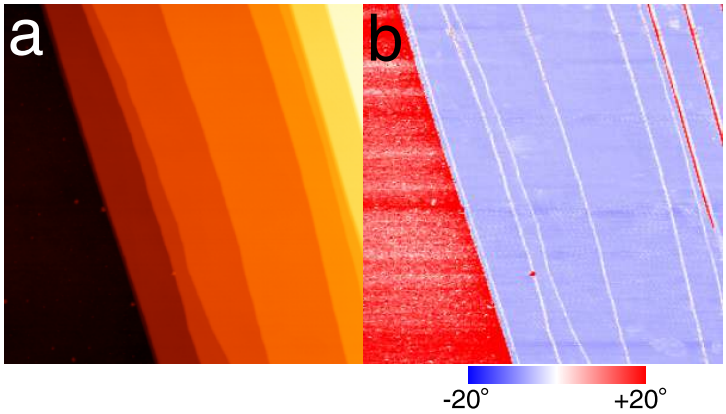

Figure 3.3: **a** A TM-AFM height image of hBN terraces on graphene, the graphene lies on the left of the image and the hBN on the right. **b** The corresponding TM-AFM phase image where the change in material is clearly observed at the point where θ changes sign. This can be used to find the perimeter of hBN flakes on all substrates investigated.

3.2.2 Optical contrast

Before AFM is used, it is necesary to identify thin hBN layers by optical contrast. Optical contrast has been shown to be useful in determining the number of graphene layers in few-layer samples[6]. The same is possible for hBN but due to its low optical absorption, the contrast is significantly lower, making flake hunting more challenging and time consuming. A model based on thin film interference[7,8] was made to simulate the interaction of light with the sample in order to find optimal conditions for flake hunting. Briefly, the model uses boundary conditions at each interface to determine the amplitude, phase and angle of the refracted and reflected light. The contrast can be tuned by varying the thickness of SiO_2 as it will determine whether the light rays will interfere constructively or destructively. This is integrated over the solid angle determined by the maximum acceptance angle of the microscope objective, see fig. 3.4. The contrast can also be changed by using different lenses with different acceptance angles. A complete description of the model for few layer hBN on SiO_2 is given in appendix A.

The model is valid for any sample and substrate materials as long as certain optical properties are known. Figure 3.6 shows the optical contrast of mono- and bi- layer hBN on SiO_2 with an oxide thickness of 300 nm. The circles are experimental data where contrast has been determined from images taken with wavelength filters with a Gaussian lineshape and a FWHM of 10 nm. The solid lines are from the model with the material parameters of SiO_2 taken from literature[9] and those of hBN, see fig. 3.5, taken from elipsometry measurements[10]. The lower panel shows optical micrographs of the same hBN flake taken

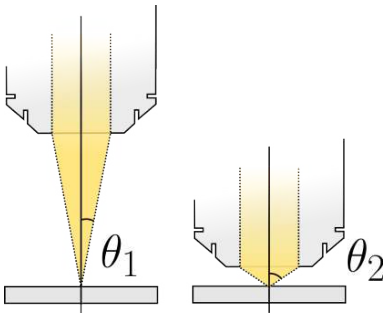

Figure 3.4: Numerical aperture of a microscope lens. $\theta_1 < \theta_2$

[6] Blake, P. *et al.* *Applied Physics Letters*, 91 (2007) 063124.

[7] Hecht, E. *Optics*. Addison-Wesley (2002).

[8] Casiraghi, C. *et al.* *Nano Letters*, 7 (2007) 2711–2717.

[9] Palik, E. D. *Handbook of Optical Constants of Solids*. Academic Press (1984).

[10] Elipsometry measurements were performed by Dr. Vasyl Kravets.

with wavelength filters at 470 nm, 530 nm and 590 nm with the change of sign corresponding to the wavelength plot clearly seen; the flake is lighter then the substrate for $\lambda < 530$ nm and darker for $\lambda > 530$.

By careful selection of wavelength filter, hBN flakes become much easier to find and by comparison with values expected from the model, the thickness of few-layer hBN can be estimated. Contrast, and hence reliability of layer number determination can be enhanced by thinning the SiO_2 by chemically etching, changing the interference conditions and hence contrast.

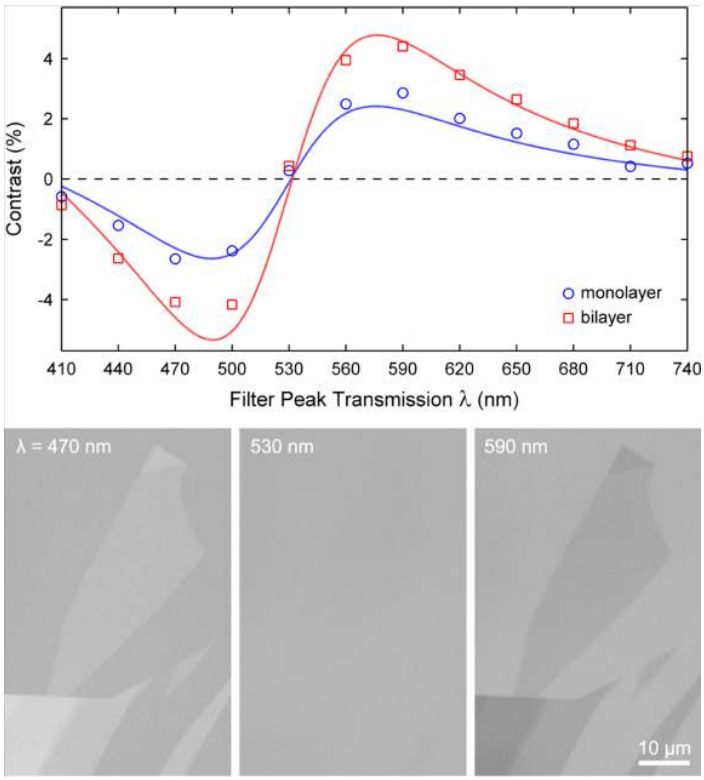

Figure 3.6: The optical contrast of mono- and bi- layer hBN on SiO_2 with an oxide thickness of 300 nm. The points are experimental data and the solid lines are from the model. The lower panel shows grayscale optical micrographs of the same hBN flake taken with wavelength filters at 470 nm, 530 nm and 590 nm. *This figure is reproduced from Gorbachev et al. (2011).*

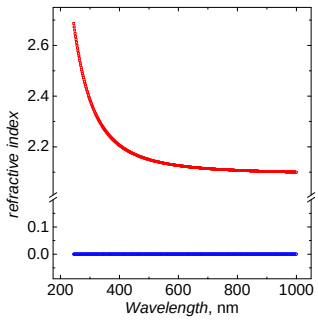

Figure 3.5: Real (red) and imaginary (blue) parts of the refractive index of hBN from ellipsometry measurements.

3.3 Electrode roughness

The materials chosen as the top or bottom contacts were Au, graphite, graphene or any combination thereof. For ease of fabrication Au was first used as both top and bottom contacts but it became apparent that due to the roughness of the Au surface–being larger than or comparable to the separation between the electrodes–the absolute current values were rather irreproducible when scaled by area of electrode overlap between different samples. To solve this problem it was decided graphene

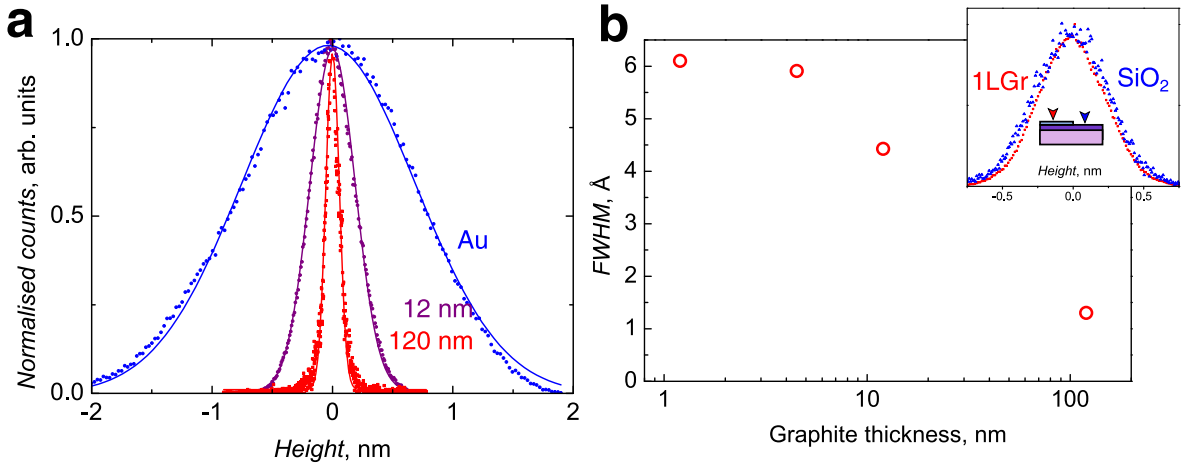

Figure 3.7: Comparative roughness of Au and graphite on SiO_2. **a** The height distributions measured by AFM on a 40 nm thick Au film, and on graphite flakes of 12 and 120 nm, measured from 1×1µm scans. The roughness of graphite is significantly smaller than the surface of the evaporated Au film. **b** The FWHM of Gaussian peaks fitted to the height distribution data of graphite on SiO_2. The inset compares the height distribution data of graphene on SiO_2 (red) and SiO_2 itself (blue) showing graphene taking on the morphology of the substrate.

or graphite would be used as electrodes; both of which have a very much flatter surface than that of evaporated Au films. Both graphene[11] on thick hBN and graphite have atomically flat surfaces, see fig. 3.7.

In order to quantify this, the height distributions of AFM topography images were compared for the different cases. Fig. 3.7**a** shows the height distributions for a 40 nm thick Au film, and graphite flakes of 12 and 120 nm thickness, taken from 1×1µm scan areas. The Au film has a full width at half maximum (FWHM) value of 1.7 nm which is significantly greater than the thickness of few-layer hBN flakes, meaning that the area contributing to the measured current will likely be significantly smaller than the total area, thus leading to the observed unpredictability of area normalised current. The surfaces of graphite with thickness greater than 100 nm change little and provide a surface that is of comparable smoothness to the hBN tunnel barrier. Fig. 3.7**b** shows the full width at half maximum (FWHM) of the height distributions for graphite on SiO_2 of different thicknesses. It takes a flake of between 50-100 nm to mask the undulations from the substrate. The inset shows the distributions for graphene on SiO_2 and SiO_2 showing graphene takes on the roughness of the oxide.

[11] Graphene tends to take on the morphology of the underlying substrate. As such when placed on the surface of bulk hBN or graphite it too will provide an atomically flat surface as expected for a plane only a single atom thick.

3.4 Current-voltage characteristics

In order to discuss the results, it is first necessary to describe the sample geometry. Samples of several types (see fig. 3.8) were made but fabrication followed the same general format as follows: [12]

[12] A more detailed description is given at the end of this chapter, section 3.9.

- A conductive substrate was chosen.
- Few-layer hBN was transferred to the surface of the conductive substrate.
- A top contact was placed to overlap with the hBN and conductive substrate in a vertical arrangement.
- External contact was made via evaporation of gold contacts through a lithographic mask.

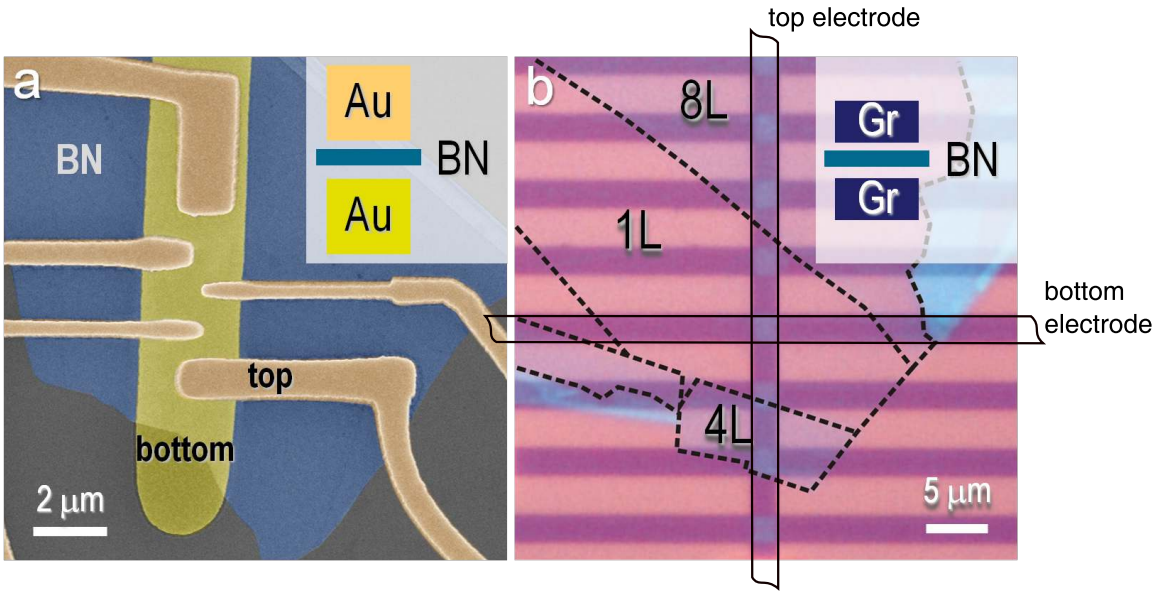

Figure 3.8: Diagrams of hBN tunnelling devices. **a** False colour SEM micrograph of a Au to Au tunnelling device. Orange and yellow areas signify top and bottom contacts respectively and the light blue shaded area signifies the hBN barrier. **b.** Optical micrograph of a graphite to graphite tunnelling device. The horizontal purple strips are bottom contacts and the single vertical strip is the top contact–making a tunnel junction at each overlap region, although barely visible the hBN can be seen inside the dashed black line with the areas of different thickness labelled by the corresponding number of layers. *This figure is reproduced from Britnell et al. (2012)*[a].

[a] Britnell, L. *et al. Nano Letters*, 12 (2012) 1707–1710.

The main results presented here will be from the *graphite* to *graphite* devices as these showed the greatest reproducibility and hence mostly samples of this type were fabricated. The graphene samples behaved in a similar fashion to graphite but involved more steps in fabrication–needing an extra hBN substrate layer for flatness–and hence tended to be more contaminated.

Two types of sample are shown in fig. 3.8. Fig. 3.8**a** shows a false colour scanning electron microscope[13] image of a Au/hBN/Au sample where the orange/yellow signify the top and bottom electrodes respectively, while the blue denotes hBN and dark grey is the SiO_2 substrate.

Fig. 3.8**b** shows an optical image of a graphite/hBN/graphite device where the horizontal and vertical purple bars are the etched graphite electrodes. The perimeter of the faintly visible hBN is shown by the dotted lines. The areas as labelled were determined by AFM. A tunnel junction occurs at each overlap

[13] This scanning electron microscope (SEM) image was taken by Dr. R. Gorbachev. SEM is a technique which has not been used heavily so it will not be explained in detail. It is sufficient to say that an accelerated beam of electrons is scanned across a sample surface and a contrast is seen due to the electrons interaction with the sample. SEM is sensitive to both the geometry and material of the sample.

of the graphite strips.

In order to measure the $I(V_b)$ characteristics of our devices, a bias voltage V_b was applied between the top and bottom contacts and the current flowing through an external load resistor was measured–ensuring that $R_{load} \ll R_{sample}$. All results presented below are from measurements on graphite/hBN/graphite devices unless explictly stated otherwise.
The $I(V_b)$ curves shown in fig. 3.9 are for 1 to 4 layers (0.34 nm to 1.4 nm) of hBN respectively and have been normalised by lateral area–the thicker the hBN the lower the current. The $I(V_b)$ curves are linear close to $V_b = 0$ but take on an exponential dependence at higher V_b. A linear fit of the zero bias region gives conductance per unit area values ranging from 1 mS µm^{-2} for hBN monolayer to 10 nS µm^{-2} for 4 hBN layers. The samples with graphene electrodes displayed similar behaviour but because of the low DOS, had a much smaller zero bias gradient. At high bias values both graphene and graphite gave similar current values as the Fermi level is moved far from the zero point in the DOS. The samples with Au electrodes showed similar $I(V_b)$ but were not reliably normalised by area and hence are neglected.

The data is condensed to show dependence of the tunnel resistance per unit area on the number of hBN layers, plotted on log scale in fig. 3.10. The area normalised resistance changes from 1 kΩ µm^2 for hBN monolayer to 0.1 GΩ µm^2 for 4 layers. The thickness dependence is ∼1.5 dec per hBN monolayer.

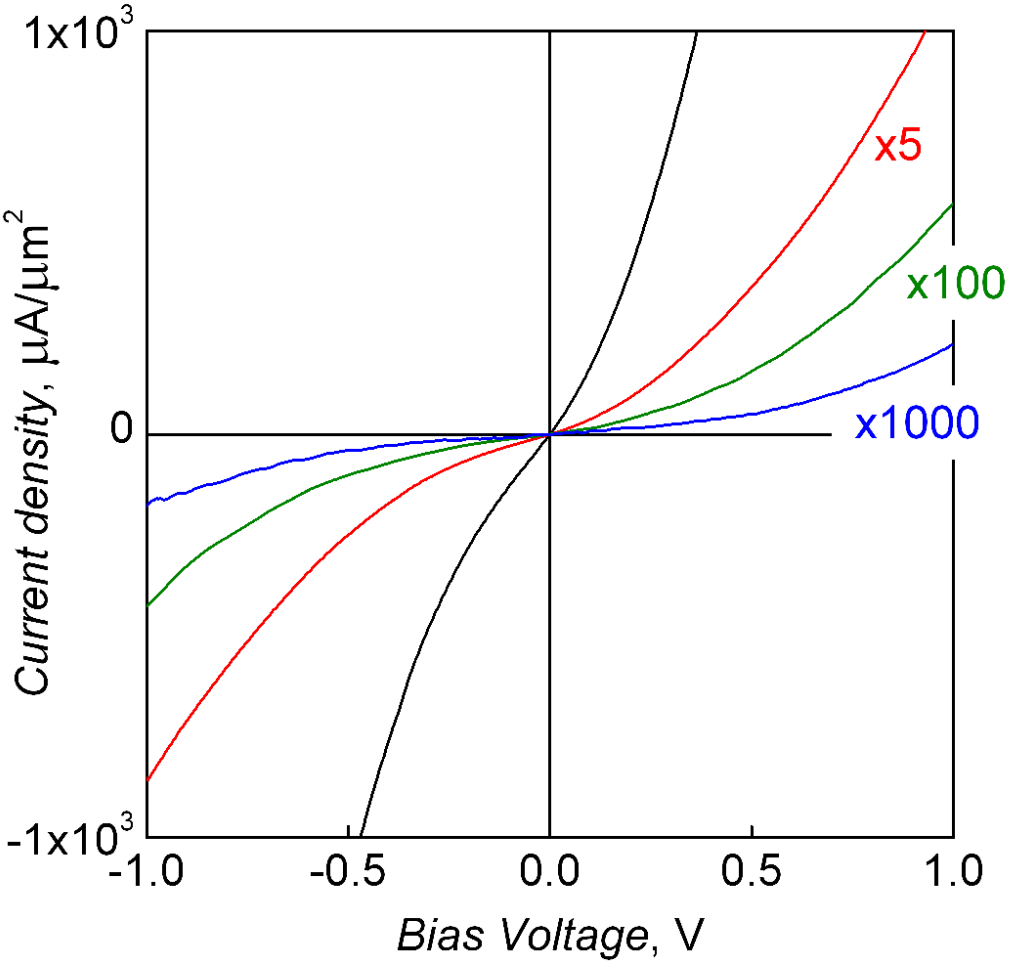

Figure 3.9: Experimental *current-voltage* characteristics for graphite/hBN/graphite tunnel junctions with thicknesses of 1 to 4 layers (black, red, green and blue respectively). In order to fit the data on the same plot the curves have been multiplied by the factors shown on the graph. The curves are linear around zero bias but take on an exponential dependence as V_b is increased. *This figure is reproduced from Britnell et al. (2012)*[a].

[a] Britnell, L. *et al. Nano Letters*, 12 (2012) 1707–1710.

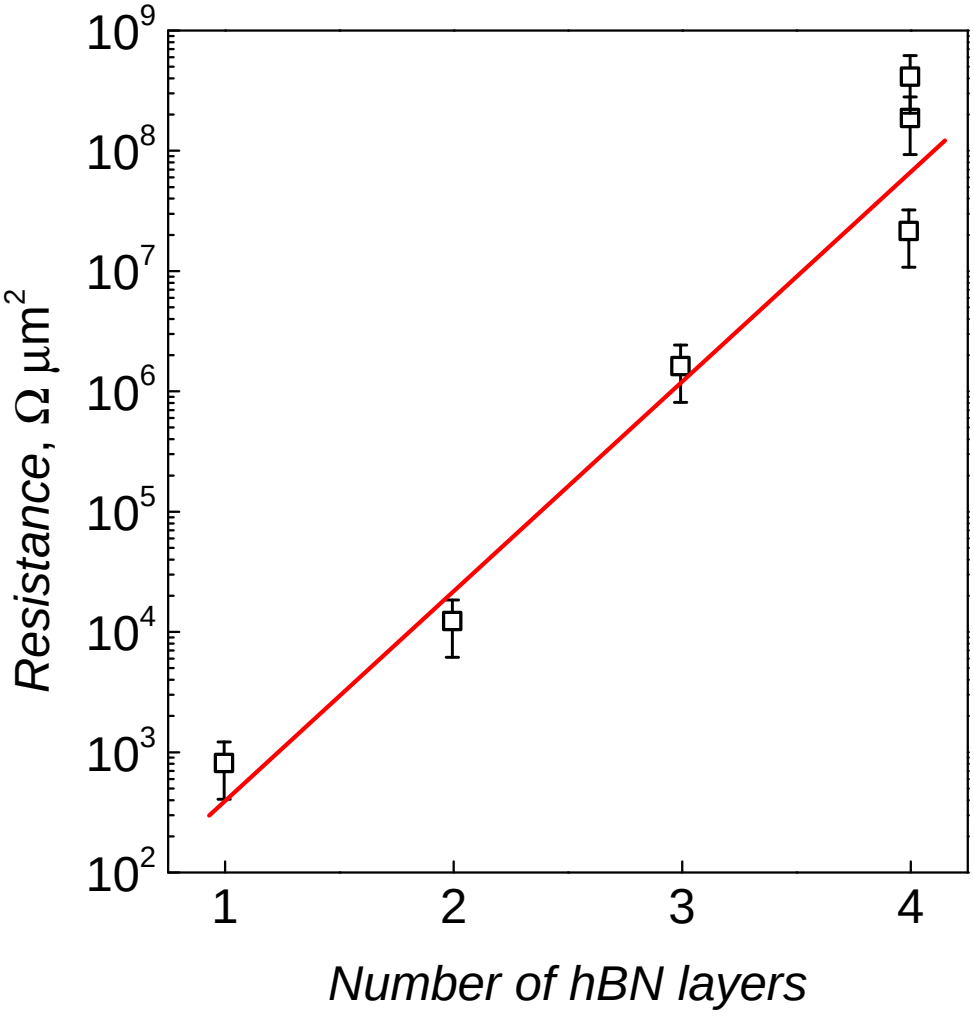

Figure 3.10: The dependence of area normalised tunnel resistance on hBN thickness. The resistance per unit area changes from 1 kΩ μm^2 for hBN monolayer to 0.1 GΩ μm^2 between 1 and 4 monolayers. The thickness dependence is ∼1.5 dec per hBN monolayer. *This figure is reproduced from Britnell et al. (2012)*[a].

[a] Britnell, L. *et al. Nano Letters*, 12 (2012) 1707–1710.

3.4.1 Graphite vs. graphene electrodes

As will be discussed in the section of modelling, the major difference when using graphene–as opposed to graphite–electrodes, is that due to the low DOS near the Dirac point, there is a much smaller gradient $\Delta I/\Delta V_b$ near V_b=0. This is shown in fig. 3.11 where $I(V_b)$ curves are shown for two devices with 4 layer hBN; the black curve is for a device with graphite electrodes and the red for graphene electrodes. The values at high bias, far from the Dirac point in graphene, become comparable as the DOS increases.

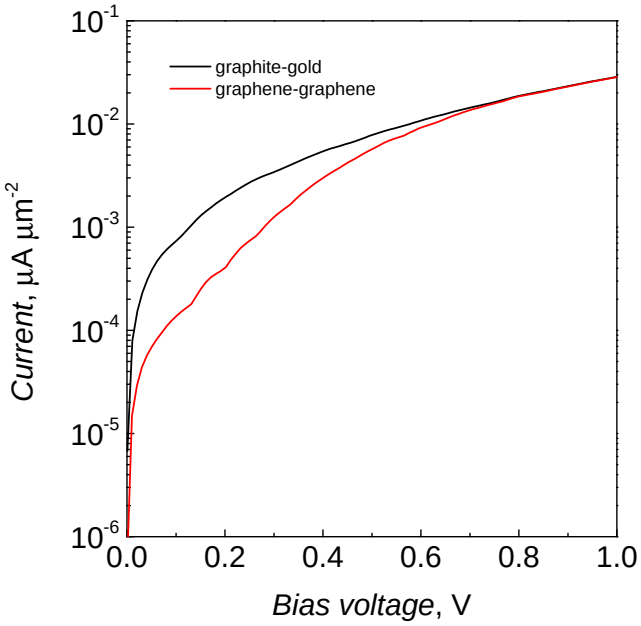

Figure 3.11: Comparison of $I(V_b)$ with graphene and graphite electrodes. The low density of states in graphene near the Dirac point means that the slope of $I(V_b)$ is much smaller at low bias in comparison to graphite electrodes. At high bias the curves become similar as the Fermi level is shifted far from the Dirac point.

3.5 Modelling

Simmons model for metal-insulator-metal (MIM) junctions

The 1963 work of Simmons[14] gives a description of tunnelling between metallic electrodes separated by an arbitrarily shaped barrier under different bias voltage conditions. A brief description of his work follows.

[14] Simmons, J. G. *Journal of Applied Physics*, 34 (1963) 1793–1803.

The hBN presents a potential barrier to electrons in one electrode from reaching the other. The probability T(E) for an electron with a kinetic energy E_x normal to the interface to tunnel through a barrier of width d is given by

$$T(E) = exp\left\{-\frac{4\pi}{h}\int_{-d/2}^{+d/2}(2m(\Delta(x) - E_x))^{\frac{1}{2}}dx\right\} \qquad (3.1)$$

where h is the Planck constant, and $\Delta(x)$ the barrier height as a function of position inside the barrier, assuming the centre of the barrier resides at $x = 0$ and the edges of the barrier at $\pm\frac{d}{2}$. The probability is exponentially dependent on the effective barrier height $\Delta(x) - E_x$. As V_b is increased the effective height is lowered increasing the probability of tunnelling.

Parameter	symbol	literature value	value used
mean barrier height, eV	$\bar{\phi}$	1.5[19]	1.43
thickness, Å	d	3.4[20]	3.7
effective mass, m_0[21]	m_e	0.5[22]	0.5

Table 3.1: Fit parameters for 1 to 4 hBN layers.

Approximating the barrier with its mean height $\bar{\phi}$, the work of Simmons[15] gives

[15] Simmons, J. G. *Journal of Applied Physics*, 34 (1963) 1793–1803.

$$I(V_b) \propto \frac{e}{4\hbar\pi^2 d^2}\left\{\left[\left(e\bar{\phi}-\frac{eV_b}{2}\right)\exp\left(\frac{-2d\sqrt{2m_e}}{\hbar}\left(e\bar{\phi}-\frac{eV_b}{2}\right)^{\frac{1}{2}}\right)\right]-\left[\left(e\bar{\phi}+\frac{eV_b}{2}\right)\exp\left(\frac{-2d\sqrt{2m_e}}{\hbar}\left(e\bar{\phi}+\frac{eV_b}{2}\right)^{\frac{1}{2}}\right)\right]\right\} \quad (3.2)$$

This expression gives the net current for a given bias where the first term gives the flow of electrons from electrode (1) to (2) and the second the flow from electrode (2) to (1). Under applied bias there is a net current, the magnitude of which is determined by the difference between the height of the barrier and the applied bias. Recent theory[16] predicts that the Fermi level of graphene lies closer to the valence band than to the conduction band of hBN and hence it is hole tunneling, rather than electron tunneling, that will dominate the $I(V_b)$. The values from literature used in the calculation are barrier height[17] $\bar{\phi}$ ∼1.5 eV and the hole effective mass $m_e = 0.5\ m_0$[18]. This expression can now be used to model the behaviour of the tunnel current. The parameters used are summarised in table 3.1 and the resultant plots are shown as dashed lines in fig. 3.12. In the plot curves for 1 to 4 layers of hBN are shown alongside the corresponding experimental data. The only parameter that is changed between curves is the thickness parameter which is increased in integer steps of the bulk c-axis lattice constant. The model replicates the behaviour well across the bias range 0 to 1 V with parameters given in the literature. The value of $\bar{\phi}$ is taken from a fit of this expression to the experimental data for 4 hBN layers using d=1.4 nm. The same parameters were then used for the corresponding thicknesses from 1 to 3 layers, giving the dashed lines shown in fig. 3.12.

[16] Kharche, N. & Nayak, S. K. *Nano Letters*, 11 (2011) 5274–5278.

[17] Kharche, N. & Nayak, S. K. *Nano Letters*, 11 (2011) 5274–5278.

[18] Xu, Y. N. & Ching, W. Y. *Physical Review B*, 44 (1991) 7787–7798.

[19] Kharche, N. & Nayak, S. K. *Nano Letters*, 11 (2011) 5274–5278.

[20] Ooi, N. *et al. Modelling and Simulation in Materials Science and Engineering*, 14 (2006) 515–535.

[21] $m_0 = 9.11 \times 10^{-31}\ kg$ is the free electron mass.

[22] Xu, Y. N. & Ching, W. Y. *Physical Review B*, 44 (1991) 7787–7798.

3.6 Local mapping of tunnelling transparency current

In order to examine the tunnelling behaviour on a smaller lateral scale conductive-AFM (see section 2.1.6) was used to

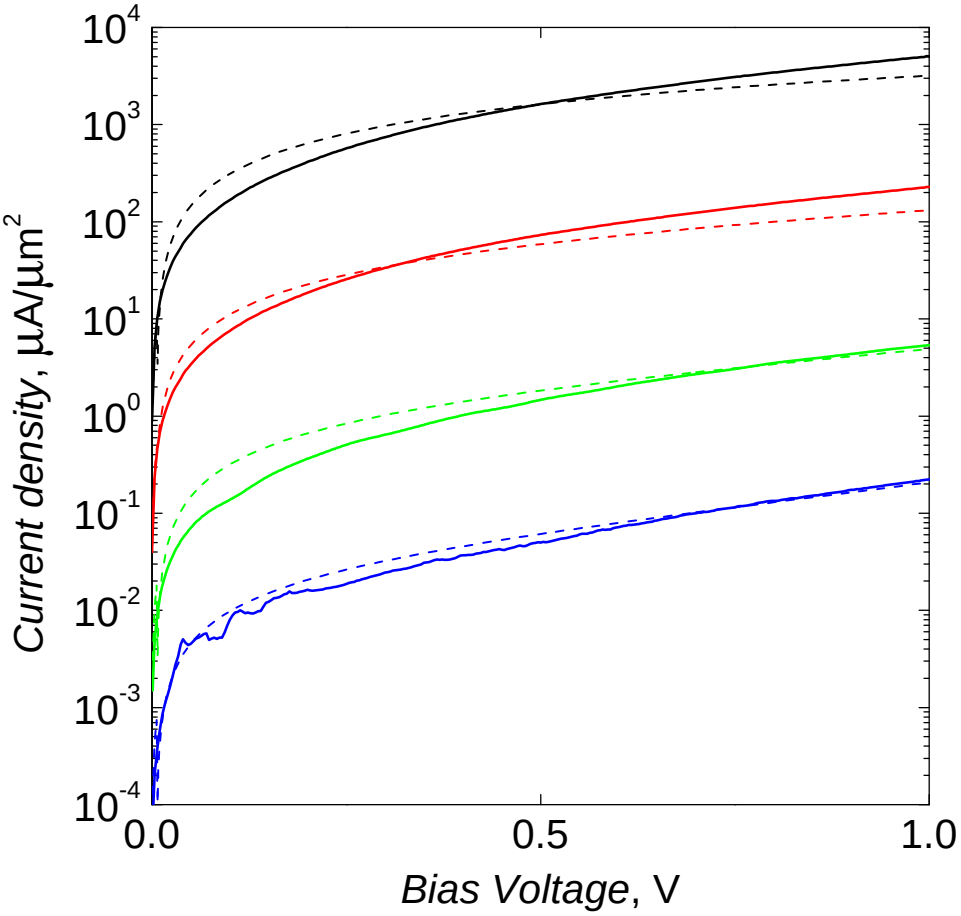

Figure 3.12: The same experimental data as shown in fig. 3.9 but shown on a logarithmic current scale. The solid lines represent the experimental data and the dashed lines are fits with the Simmons model as described in section 3.5. *This figure is reproduced from Britnell et al. (2012)*[a]

[a] Britnell, L. *et al. Nano Letters*, 12 (2012) 1707–1710.

study the local conduction through thin hBN terraces. In this case the hBN was transferred to the surface of graphite to ensure a flat surface and a conductive probe was brought into contact with the top surface, as described in section 2.1.6. Once a good contact was obtained the probe was scanned over the terrace with a very slow scan rate hunting for evidence of pinhole type defects where large deviations in current flow would be observed.

As is noted in the sample fabrication section, section 3.9, the samples used a thick graphite back electrode such that the contact surface was atomically flat. Samples with both thinner graphite and graphene were measured but due to the finite size of the tip, undulations in the substrate led to variations in tunnelling current as the effective area varied depending on the exact probe-sample contact area, see fig. 3.13. Due to thermal drift in the piezoelectric crystal used to control lateral position this was also dependent on time.

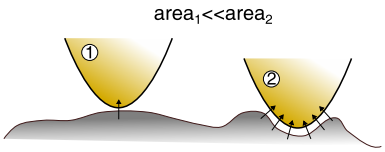

Figure 3.13: Schematic representation of the roughness dependent area of contact

3.6.1 Ensuring good contact

The electrical contact between the con-AFM probe and the top surface of hBN is vital to obtaining reliable measurements. It is possible to alter the force between the tip and sample, but with high force the conductive coating is easily damaged while scanning the sample surface. To determine the optimal force required for measurements the dependence of current with applied force was studied. The optimal operating force would be the lowest force for which the change of current with force was negligible, i.e. $\Delta I/\Delta F \approx 0$. This was studied using Pt/Ir coated AFM probes and graphite. For forces >10 nN, the decrease in resistance became negligible, when using a good quality probe, and so it was decided that an operating force of 10 nN would be suitable for recording local conductance maps. The probe-graphite resistance was checked prior to each measurement and was usually ∼10 kΩ, in agreement with systems using similar probes. This includes both the probe-graphite and graphite-electrode resistance as well as the internal resistance of the graphite itself. The probe-sample resistance should dominate because of the small contact area and spreading of the electric field inside the graphite. The probe-sample contact area should be slightly increased in ambient conditions by the ever present water meniscus[23].

[23] O'Shea, S. J., Atta, R. M. & Welland, M. E. *Reviews of Scientific Instruments*, 66 (1995) 2508.

3.6.2 Local conduction maps

A series of maps were made on various hBN/graphite samples in order to search for pinhole type defects that would allow

Technical data	Nominal value
Thickness	2 µm
Width	50 µm
Length	450 µm
Force constant	2 N/m

Table 3.2: Pt/Ir coated AFM probes used are from Nanosensors (Product code: PPP-CONTPt).

large current flow through the hBN film. An example of such a map is shown in fig. 3.14.

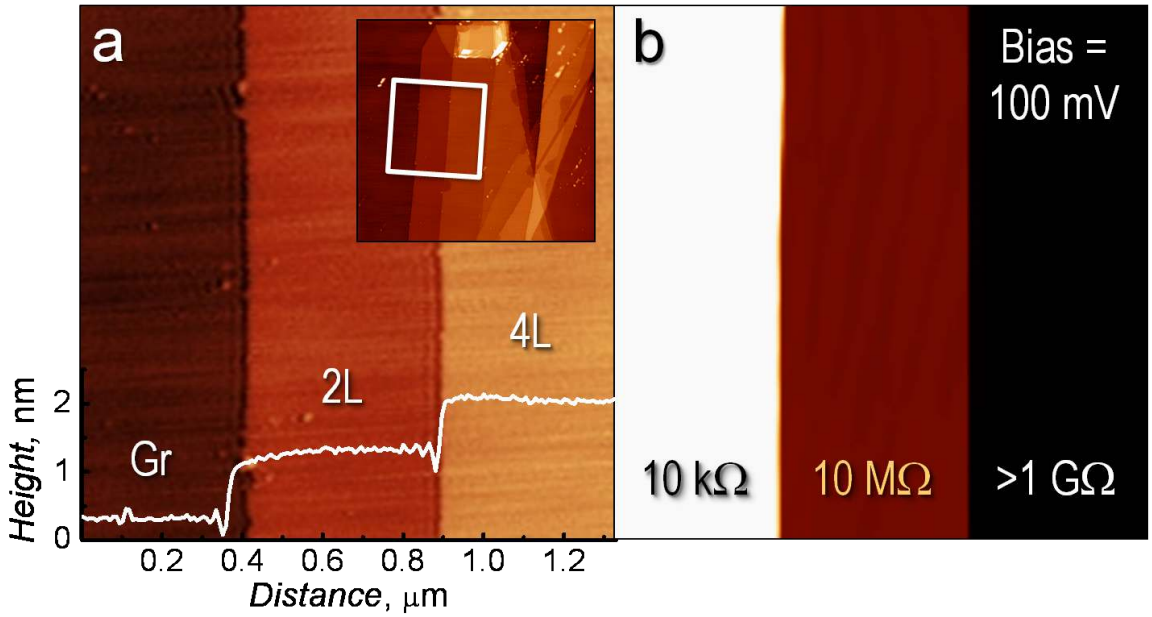

Figure 3.14: Local conduction map on graphite/hBN using conductive-AFM. **a.** A tapping-mode AFM topography image of hBN terraces on graphite. The three regions are graphite, 2 layer hBN and 4 layer hBN as labelled. The inset shows a larger scale topography image with the region of the main image marked by the square. **b.** The corresponding current image with the same three regions. The measured current is homogeneous across each region and has an exponential dependence on hBN thickness as expected. The scans were taken at 0.1 Hz. *This figure is reproduced from Britnell et al. (2012)*[a].

[a] Britnell, L. *et al. Nano Letters*, 12 (2012) 1707–1710.

Graphite was used as the back electrode due to its atomically flat surface aiding the reliability of measurement. After transferring an hBN flake to the surface of graphite, thin areas were identified by TM-AFM. Using a conductive probe, the resistance to graphite was checked to ensure a good conduction (<10 kΩ). The probe was then positioned above an hBN terrace and scanned while applying a set bias between the probe and graphite electrode, the voltage across a load resistor in series was fed into the AFM controller to be recorded alongside topography measurements. Usually, the thinnest hBN flakes are found around the edges of thicker ones, so in most cases the parameters of the scan were set to traverse the graphite/hBN border so that the ohmic conduction to graphite could be monitored during scanning. This is favoured due to the fragile nature of the conductive coating on the probes. This leads to the type of image shown in fig. 2.11. Streaks are seen at the edge of each terrace due to the relative lateral speed of the probe to the read time of the electronics. Cleaner images could be obtained by either scanning at very low scan rates or by scanning at 90° to the edge but had to be correlated with scans at 0° to check consistant values were obtained. A scan taken

at 90° is shown in fig. 3.14 where the edges of the terraces appear much sharper than in fig. 2.11. This is preferable to scanning at low scan rates due to the problems associated with thermal drift.
Similar scans were taken on many flakes; nearly all showed a very high degree of homogeneity, suggesting that few-layer hBN would be a suitable tunnel barrier for more complex electronic devices. In virtually all cases, images as shown in fig. 3.14 were seen. However, a few examples of pinholes were found, possibly due to repeated scans of the same area. They are shown here to confirm that should such features exist in all flakes they would have been observed with this technique. An example is shown in fig. 3.15. The same scan parameters were used but spikes in current were noted during scanning. These spikes appeared in both trace and retrace scans and were also present in repeated scans of the same area. In fig. 3.15**a** an AFM image of the device is shown. A 4 layer hBN flake spans the entire image while edge of the graphene back electrode is on the right hand side. In the current image, fig. 3.15**b**, one can see a darker region on the right where there is no graphene and spikes (red areas) where an increased current flow is observed. The size of the pin holes is difficult to determine as the size of the features is masked by the probe area. In fig. 3.15**c** and **d**, 3D representations of the trace and retrace current images are shown, the same features are clearly present in both, indicating that they are not artifacts of imaging.

3.7 Conclusions

It has been demonstrated that with these transfer techniques, it is possible to use hBN as a tunnel barrier for a variety of conductive materials and conductive AFM showed that hBN retains its integrity following processing with the tunnel current being highly homogeneous across micron scale areas. The $I(V_b)$ characteristics are typical of tunnelling, as confirmed by fitting with the Simmons model. The magnitude of the current in the low bias regime is dependent on the thickness of hBN by 1.5 decs per monolayer. It is concluded that hBN is a suitable material to use in 2D crystal based heterostructures with more complex geometries.

3.8 Discussion and outlook

The progression of graphene research toward the creation of heterostructures means that compatible materials should be

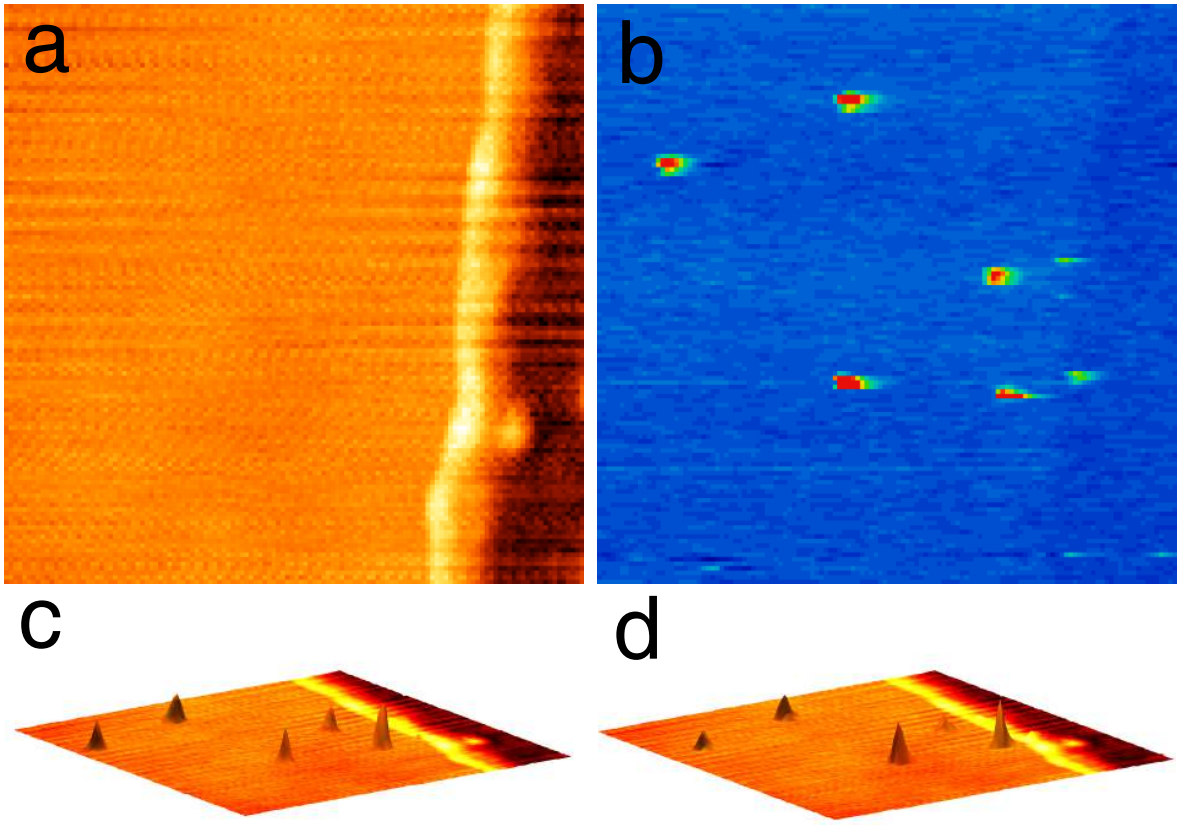

Figure 3.15: Although scarcely found on most hBN terraces, a few examples of pinholes found were found on some samples. **a** The topography image of the sample and **b** is the the corresponding current image. The entire area shown (500×500 nm) is covered by 4 layer hBN while the vertical feature in the height image is the edge of a graphene flake. In the current image, a small tunnel current is seen on graphene and no current flow on the right-hand side. Spikes in the current image are suspected pinhole defects where a large current flows. **c** The trace and **d** retrace images for current (overlaid with the height data) show that the spikes are present in the same position in both meaning they are unlikely to be artifacts. The same spikes were also seen in repeated scans of the same area. This scan was taken after waiting for thermal drift to reduce. A scan rate of 0.1 Hz and V_b=1.5 V were used.

found. The search for a suitable substrate seems to have slowed since hexagonal boron nitride was found to be close to ideal[24]. In this work we've shown that similar techniques to those required to place graphene on hBN can be used to transfer few layer hBN onto graphite in a contrariwise fashion. As a result we were able to show that few-layer hBN behaves as a uniform tunnelling barrier and due to its high purity can be used even as thin as a monolayer. While interesting in itself, more importantly it enables creation of double layer structures, where the coupling between two graphene layers can be tuned with atomic precision. The control with atomic precision is expanded upon in appendix A where a general model is presented which calculates the optical contrast between hBN of a set thickness on an arbitary substrate with a comparison to experiment. Results from double layer structures are given in the subsequent chapters.

[24] Dean, C. R. *et al. Nature Nanotechnology*, 5 (2010) 722–726.

3.9 Sample fabrication

Samples of several geometries were produced for this series of experiments as described below.

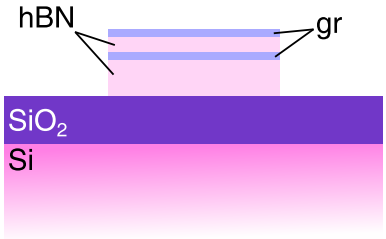

Figure 3.16: Graphene/hBN/graphene schematic.

Graphene/hBN/graphene

The following describes the fabrication of graphene/hBN/graphene samples (fig. 3.16) but exactly the same can be taken for the graphite/hBN/graphite samples except where specified.
In order to measure the tunnelling between two graphene or graphite layers, first a thick hBN flake was cleaved onto a SiO_2 substrate to be used as a flat surface for the bottom graphene layer. Two graphene flakes and a few-layer hBN flake were cleaved onto separate dual layer polymer substrates. By *dry transfer*, as described in 1.4, the first graphene flake was first transferred to the top surface of the thick hBN flake followed by the disolution of the sacrificial polymer layer. After annealing at 300° C in H_2/Ar (10:90) the few-layer hBN and then the second graphene flake were subsequently transferred to the top surface of the crystal stack in the same manner, each time followed by the same polymer removal and annealing process. The transfer alignment process was made in such a way that there was no electrical connection between the top and bottom graphene flakes except through the hBN layer. The graphite samples were produced in the same way, with the exceptions being that in some cases the etching of the graphite flakes (∼5-10 nm in thickness) was needed to produced the required electrode shape. In this case it was necessary to prepare the top

graphite flake on a Si/SiO_2 substrate, prepare an etch mask by e-beam lithography, etch the graphite in an oxygen plasma and then transfer using the wet transfer method. To help reduce trapped contamination, the graphite strips were deliberately etched to a narrow width of ∼1 µm so that upon annealing the contaminant species would be able to escape the interface[25].

[25] Haigh, S. J. *et al.* *Nature Materials*, 11 (2012) 764–767.

Graphite/hBN/AFM probe

The samples that were fabricated for conductive AFM studies, see section 3.6, were required in a slightly different geometry (fig. 3.17). First a 15 nm thick Au film was deposited onto a Si/SiO_2 wafer in an e-beam evaporator. Graphite crystallites were then cleaved on top of the deposited Au film. Thus the sample could be connected electronically in a fashion suitable for insertion into the AFM head. A 20-30 nm thick piece of graphite was chosen–thick enough that undulations and roughness from the underlying Au film are masked by the atomic flatness of graphite. A few layer hBN flake was then transferred to the surface of the graphite flake and the sample annealled as described in the previous paragraph.

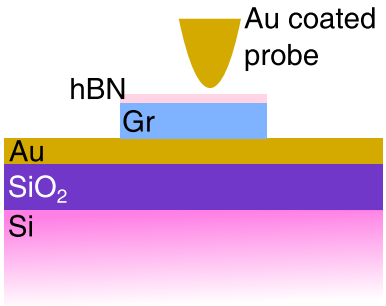

Figure 3.17: Graphite/hBN/AFM probe schematic.

Au/hBN/Au

The Au/hBN/Au samples (fig. 3.18) were produced by wet etching periodic trenches in SiO_2 through an etch mask. Au was evaporated onto the Si wafer with a thickness equal to the trench depth meaning the top of the Au electrode was a similar height to the oxide surface. Few-layer hBN was cleaved onto the wafer and using an optical microscope, suitably thin flakes that overlapped the Au electrodes were found. E-beam or optical lithographic techniques were then used to fabricate the top Au contacts.

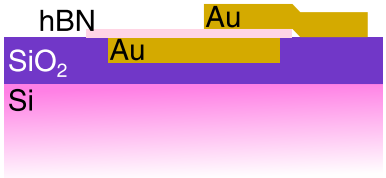

Figure 3.18: Au/hBN/Au schematic.

3.10 Measurement of overlap area

Once the thickness of hBN could be determined samples could be fabricated. However, to enable comparison of devices it was necessary to normalise by area; this was measured in several ways. The topography of most samples was measured by AFM and the area could be accurately determined. The active area was assumed to be the total area of the device. When using Au electrodes, it was apparent that the active area was unpredictable, most likely due to the roughness of the Au surface. This measured area was observed to be more reliable when replacing the Au leads with graphite. In the case of devices

that weren't measured by AFM, either SEM or optical images were used; the precision of the various methods is given in table 3.3. SEM and AFM have similar lateral precision but generally SEM can be more destructive to the sample, so AFM was preferentially used. Optical images have a much lower precision but the technique is completely non-destructive and of adequate precision for larger samples (>10 µm^2.).

Method	Precision
AFM	∼30 nm
SEM	∼10 nm
Optical (100× objective)	∼ 1 µm

Table 3.3: Precision of different techniques to measure device area.

Chapter 4

Field-effect transistor based on graphene-boron nitride heterostructures

In this chapter, devices comprised of two graphene layers which sandwich a thin insulating hBN layer will be introduced. This separation is small enough to allow electrons to quantum mechanically tunnel through the dielectric layer as shown in the previous chapter. With the device placed on an oxidised silicon wafer, the SiO_2 being used as a gate dielectric, the tunnel current can be modulated to form a tunnelling transistor. Experimental evidence of this effect is presented and a model developed which describes the data well.
The results for this chapter have been published as a letter in Science. My contribution to this work was measuring and analysing experimental data, and implementing the model.

4.1 Introduction

Among the more heavily discussed applications of graphene is its use in digital electronics. The room temperature mobility is one of the highest in any material[1,2] but it can be elastically deformed up to 20%[3] making it suitable for flexible electronics. Furthermore, chemical modification of graphene alters it electronic properties[4,5], potentially allowing circuitry to be printed onto a single graphene sheet by selective reaction[6]. However, the realisation has been hampered by the lack of an energy gap in graphene's electronic band structure; meaning that although current modulation is possible through use of an external gate electrode, it is difficult to acheive a low power dissipation *off* state which would be required for practical transistor use.
This chapter discusses the properties of a field-effect tunnelling transistor which utilizes graphene's low density of states near the Dirac point. The prototype devices are based on atomically thin crystal based heterostures[7].These devices show an *on-off* ratio of up to 40 with hBN. If the hBN layer is replaced by a TMDC such as MoS_2 or WS_2 the *on-off* ratio can exceed 10^5 as shown in the supporting information to Britnell *et al.*[8].

[1] Bolotin, K. I. *et al. Physical Review Letters*, 101 (2008) 096802.

[2] Mayorov, A. S. *et al. Nano Letters*, 11 (2011) 2396–2399.

[3] Lee, C. *et al. Science*, 321 (2008) 385–388.

[4] Elias, D. C. *et al. Science*, 323 (2009) 610–613.

[5] Nair, R. R. *et al. Small*, 6 (2010) 2877–2884.

[6] Wang, Q. H. *et al. Nature Chemistry*, 4 (2012) 724–732.

[7] .

[8] Britnell, L. *et al. Science*, 335 (2012) 947–950.

Graphene field-effect transistors (Gr-FET) have been hampered by graphene's minimum conductivity at the Dirac point and the high transparency of potential barriers to charge carriers due to Klein tunneling. This limits the switching ratios in the devices to <10 at room temperature. Low switching ratios can be utilized in analog electronics[9] but are not suitable for integrated digital electronics. The key problem is graphene's zero band gap. A band gap can be created via quantum confinement by physically restricting the dimensions of devices, examples being graphene quantum dots[10], nanoribbons[11] and graphene nanomeshes[12] and also by changing the carbon atoms' hybridization by chemical modification[13]. However, all of these methods generally degrade graphene's electronic properties, negating its use in real devices.

[9] Wu, Y. *et al. Nature*, 472 (2011) 74–78.

[10] Stampfer, C. *et al. Frontiers of Physics*, 6 (2011) 271–293.

[11] Han, M. Y. *et al. Physical Review Letters*, 98 (2007) 206805.

[12] Bai, J. *et al. Nature Nanotechnology*, 5 (2010) 190–194.

[13] Nair, R. R. *et al. Small*, 6 (2010) 2877–2884.

All these architechtures use graphene as the channel with electronic transport in the plane of the layer. In this chapter, it will be shown that the geometry introduced in the previous chapter can be used to overcome some of these problems. The setup of two graphene layers, electronically isolated by a atomically thin hBN barrier, is again used and an example is shown in fig 4.1. The device relies on quantum tunnelling of electrons between the layers and the ability to modulate the magnitude of this current via a gate electrode. The size of the tunnel current is primarily dependent on two parameters: the effective barrier height Δ and the density of states in the top and botton graphene electrodes (DOS_T and DOS_B respectively). With hBN as the thin dielectric barrier the effective barrier $\Delta \sim$1.5 eV from literature[14]. The difference between the data presented here and that in chapter 3, is that only graphene electrodes have been used and in some cases they have been fabricated into Hall bar structures so that the properties of each electrode can be measured separately.

[14] Xu, Y. N. & Ching, W. Y. *Physical Review B*, 44 (1991) 7787–7798.

Samples were made with various geometries; in the simplest case they were simply overlapping graphene flakes (still separated by hBN) with single contacts to each electrode. More details could be gleaned however, from samples where each electrode was in the shape of a Hall bar because this allowed complete analysis of each electrode's properties individually. The four-probe configuration (see fig. 4.3) of some of the devices was used so that they could be fully characterised by transport measurements, section 2.2. The actual operation of the devices was characterised by tunneling spectroscopy, i.e. $I(V_b)$ across the hBN barrier. In most cases, the three principle layers (Gr_B/hBN/Gr_T) were sandwiched on both sides by hBN to increase homogeneity and decrease doping[15,16]. All devices

[15] Dean, C. R. *et al. Nature Nanotechnology*, 5 (2010) 722–726.

[16] Mayorov, A. S. *et al. Nano Letters*, 11 (2011) 2396–2399.

were fabricated by the *dry transfer* procedure, as described in section 1.4. with thorough annealling at 300 °C between each flake transfer to remove interfacial contamination[17,18]. With the whole structure sitting on Si/SiO_2, the Si could act as the gate electrode with SiO_2/hBN as the gate dielectric.

[17] Haigh, S. J. *et al.* *Nature Materials*, 11 (2012) 764–767.

[18] Garcia, A. G. *et al.* *Nano Letters*, (2012).

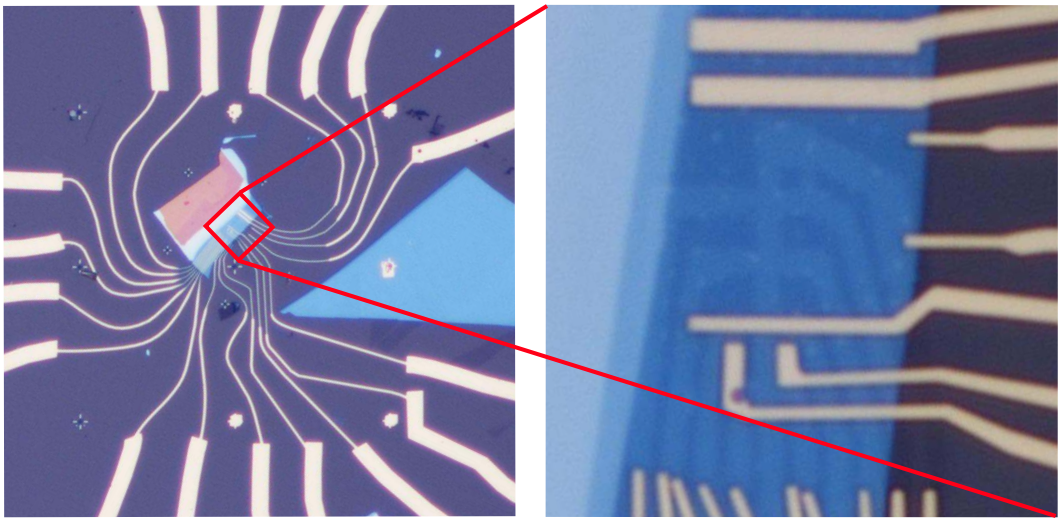

Figure 4.1: Two optical images of the same tunnelling transistor device at ×10 and ×100 magnification. In the ×100 magnification images (zoomed region indicated on the ×10 image) it is possible to make out the top Hall bar, while the bottom graphene electrode is a continuous sheet underneath the whole structure.

4.2 In-plane characteristics

The transistor operation will be discussed for two devices (device (A) in fig. 4.4 and (B) in fig. 4.5) but first the in-plane characteristics will be examined. A schematic diagram of device (A), describing the experimental setup can be seen in fig. 4.3**b**. A gate voltage V_g, applied between the Si back gate and the graphene layers, allowed the carrier concentration to be altered in both top and bottom graphene layers (Gr_T and Gr_B).

This is possible because graphene does not screen all the electric field as in conventional devices. The in-plane resistivity ρ_{xx} of both graphene layers is shown in fig.4.3**a**. The Dirac peak was seen close to zero gate voltage for both layers, signifying low levels of doping. The mobilities measured by the method described in section 2.2 were $\sim 1\times10^4$ cm^2 V^{-1} s^{-1} and $\sim 4\times10^4$ cm^2 V^{-1} s^{-1} for the top and bottom layers respectively (fig. 4.2). The doping is typically at a slightly higher level in the top layer, while the mobility is usually lower[19], possibly due to increasing surface roughness[20]. The ability of graphene to screen the electric field from the gate can be seen in Hall resistivity ρ_{xy} measurements of each layer, fig. 4.3**c,d**. At low carrier concentrations the screening efficiency is small and a similar charge is induced in both layers. However, as the

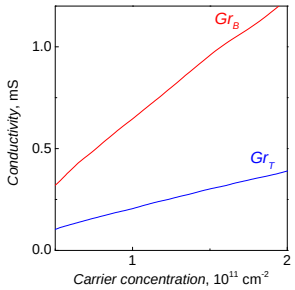

Figure 4.2: The mobility of top and bottom graphene layers of device (A) is taken from the slopes of the σ_{xx}-n plots. *This figure is reproduced in part from Britnell et al. (2012)*[a].

[a] Britnell, L. *et al.* *Science*, 335 (2012) 947–950.

[19] Ponomarenko, L. A. *et al.* *Nature Physics*, 7 (2011) 958–961.

[20] Haigh, S. J. *et al.* *Nature Materials*, 11 (2012) 764–767.

concentration of carriers in the bottom layer increases with gate electric field, it screens an increasing proportion of the field and thus the behaviour in the two layers begins to deviate. This is seen in the sub- and super- linear dependence in the top and bottom layers respectively. Note, the total induced charged remained linear, fig. 4.3**e**.

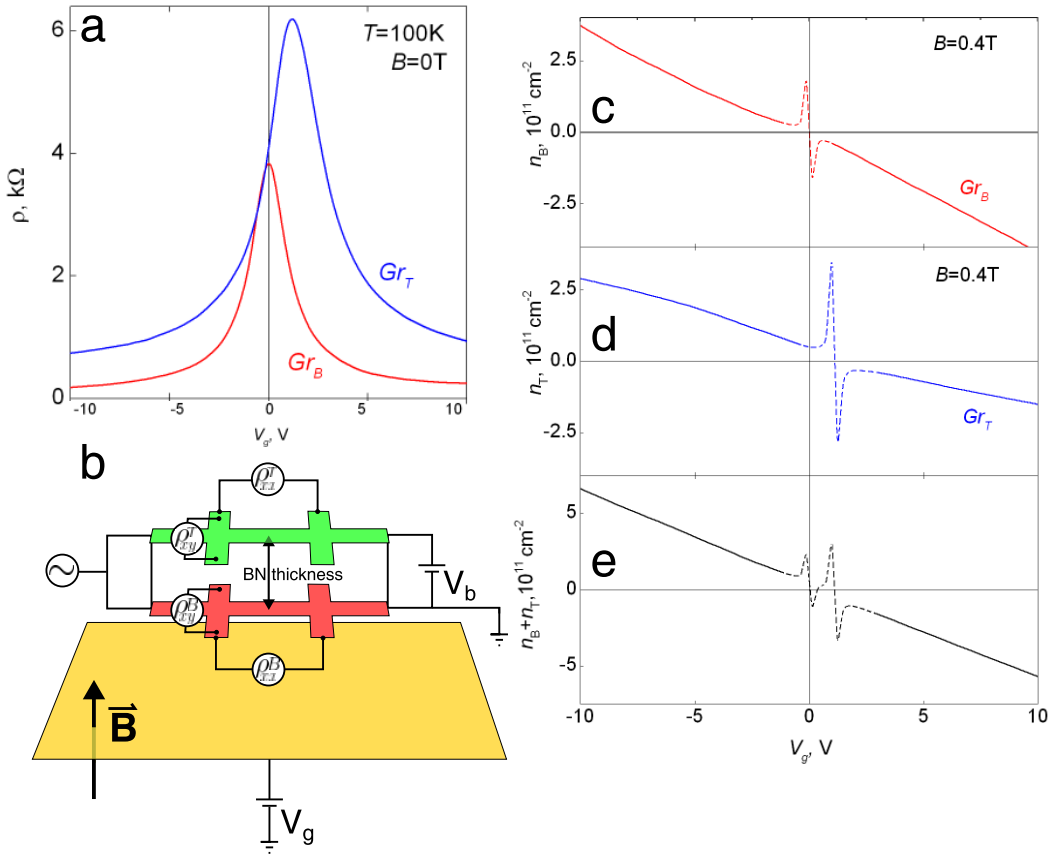

Figure 4.3: In-plane characteristics of a tunnelling transistor device. **a** The ρ_{xx} curves for top and bottom graphene layers. **b** The measurement schematic. **c** Carrier concentration in the bottom, **d** top graphene layers and **e** combined as functions of gate voltage showing superlinear, sublinear and linear dependence respectively. *This figure is reproduced in part from Britnell et al. (2012)*[a].

[a] Britnell, L. *et al. Science*, 335 (2012) 947–950.

4.3 Tunnelling transistor operation

When a bias voltage V_b was applied between the two graphene electrodes a tunnelling current was observed, as in the previous chapter. The transistor operation will be discussed for two devices; device (A) in fig. 4.4 and (B) in fig. 4.5. For both figures, panel **a** shows the $I(V_b)$ characteristics for various V_g values where there is a clear dependence of the $I(V_b)$ curves on V_g. First looking at device (A), when a small gate voltage was applied (in order to compensate doping); the low bias conductance is linear, with an inverse conductance per unit

area ρ^T ~100 GΩ µm^2. As V_b is increased the curves take on an exponential dependence. The curves at other gate voltages have a similar shape but a much larger current. To analyse this effect, each $I(V_b)$ curve was fitted with a linear function around V_b=0 giving the tunnel conductance per unit area σ^T. This is plotted in fig. 4.4**b**, where $\sigma^T = dI/dV_{V=0}$ is plotted as a function of V_g (the red line is that expected from the model presented below).

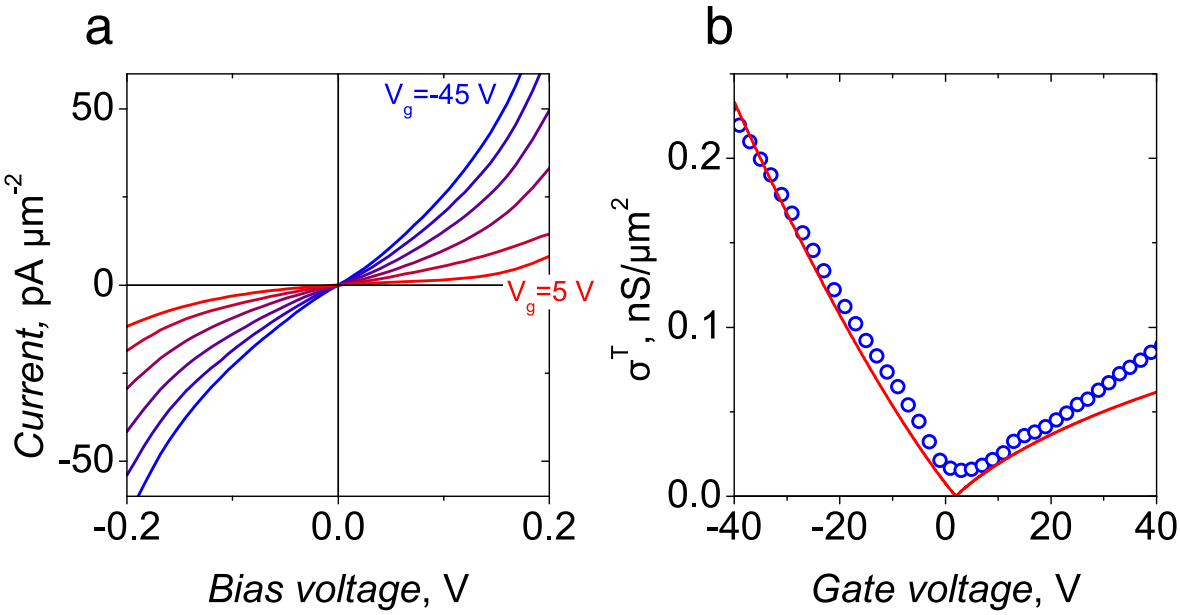

Figure 4.4: Transistor behaviour of graphene/hBN/graphene tunnel transistor device (A). **a** $I(V_b)$ characteristics at gate voltages from -45 to +5 V in 10 V steps. The gate voltage modulates the magnitude of the tunnel current. **b** The gradient of the $I(V_b)$ curves at 0 V_b is given by the blue circles and shows the conductance can be modulated by a factor of ≈20. The red line is from the model presented below. *This figure is reproduced from Britnell et al. (2012)*[a].

[a] Britnell, L. *et al. Science*, 335 (2012) 947–950.

Device (B) was not shaped into a Hall bar, so analysis of the carrier concentration and mobility could not be made but the $I(V_b, V_g)$ curves can still be analysed and are shown in fig. 4.5**a** where $I(V_b)$ is plotted in the range -55< V_g <0 V. The dependence of the $I(V_b)$ curves is similar to device (A) but there is a much broader minimum in the plot of σ^T, fig. 4.5**b**, possibly because this device was measured in ambient conditions. The minimum in the current, in both devices, did not reach zero, this is likely to be due to smearing at finite temperature and residual doping and disorder such as electron-hole puddles.

There are several things to note from the plots:

1. The neutrality point is slightly offset from zero gate voltage and lies ~2 V.
2. There is a linear dependence of σ^T on V_g, increasing on

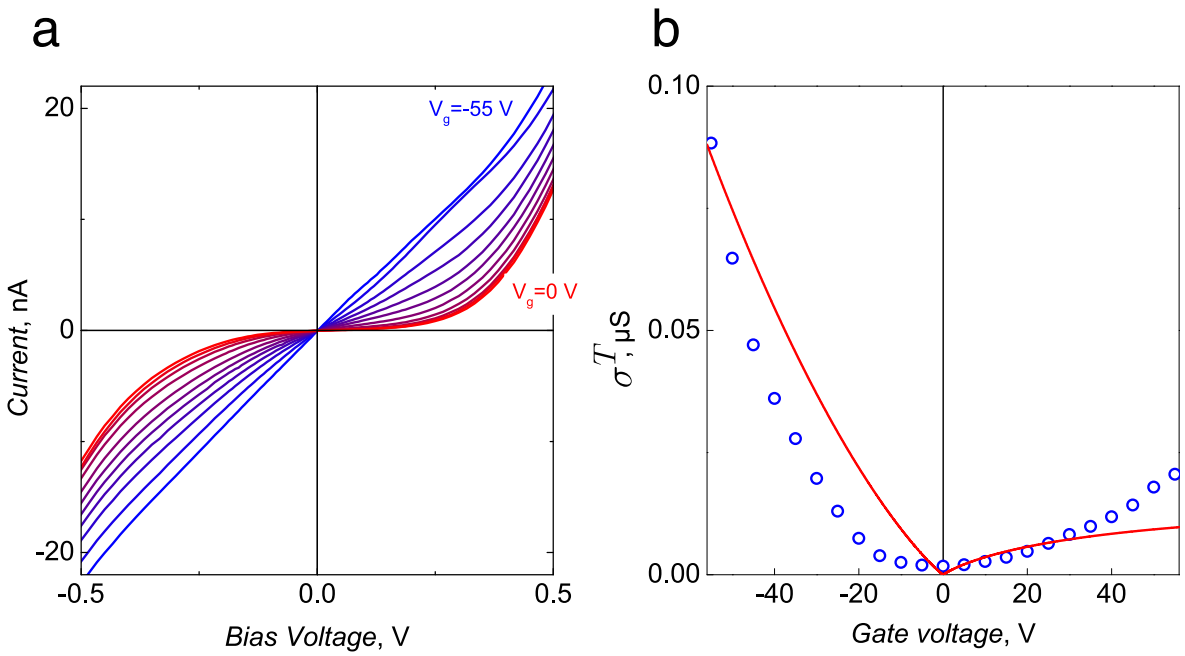

Figure 4.5: The same plots as fig. for device (B). **a** $I(V_b)$ characteristics at gate voltages from -55 to 0 V in 5 V steps. **b** The gradient of the $I(V_g)$ curves at 0 V_b is given by the blue circles and shows the conductance can be modulated by a factor of ≈40. The red line is from model presented below. *This figure is reproduced from Britnell et al. (2012)*[a].

[a] Britnell, L. *et al. Science*, 335 (2012) 947–950.

both sides of neutrality point.

3. There is an asymmetry between the tunnelling for holes (-V_g values) and for electrons (+V_g values).

Before discussing these points, it is necessary to give a brief description of the mechanism.

On either side of this minimum, the current increased primarily due to two effects: an increase in both $\mathrm{DOS_B}$ and $\mathrm{DOS_T}$ due to the gate induced charge and movement of ε_F closer to the top of the barrier, decreasing the effective barrier Δ. Fig. 4.6 shows this schematically. In **a** the initial band diagram is shown where the chemical potential is aligned across all layers, a small bias between the layers would lead to a small current because of the low DOS and height of the barrier. **b** With a positive gate voltage applied, the bands in graphene shift giving a finite number of carriers in each layer. **c** When the bias is applied now, there are many more available states to tunnel into (and out of) and in addition, the field from the gate, penetrating through the bottom graphene electrode, distorts the barrier and the Fermi level comes closer to the top of the barrier.

The relation $\sigma^T \propto \mathrm{DOS_B}(V_g)\times\mathrm{DOS_T}(V_g)\times\mathrm{T}(V_g)$ was used to analyze the data where $\mathrm{DOS_{B,T}}(V_g)$ are the density of states in the bottom and top electrodes and $\mathrm{T}(V_g)$ is the transmission

probability for tunnelling. T(V_g) is proportional to the exponent of Δ and so one might expect an exponential dependence of I on V_g but this was not observed in these devices and is instead linear. The DOS also has a dependence on gate voltage of both polarities, see fig. 4.3, thus leading to an increase in σ^T. It is deemed that the changes in I seen, are dominated by the changes in DOS.

The effect on the transmission coefficient was a smaller but still an important effect: the direction of the shift in ε_F is dependent on the sign of V_g, and hence T(V_g) increased for negative V_g but decreased for postive V_g due to the relative position of the Dirac point in graphene and the energy gap in hBN: recent theory[21] predicts that the Dirac point in graphene sits ~1.5 eV above the valence band of hBN, with the conduction band over 4 eV further above. This leads to the asymmetry of the σ^T. For device (A), σ^T changed by a factor of 20 for holes and 6 for electrons, for device (B) the current changed by 40 for holes and 10 for electrons.

The data can be well replicated with Δ=1.5 eV and m=0.5 m_0, which is in agreement with the effective mass of holes in hBN[22]. This is expected from the exponential dependence on tunnelling probability on barrier height, which is smaller for holes than electrons. Analysis of the data reveals that the changes observed in σ^T with V_g is due to changes in DOS in the two graphene layers rather than changes in the barrier height Δ.

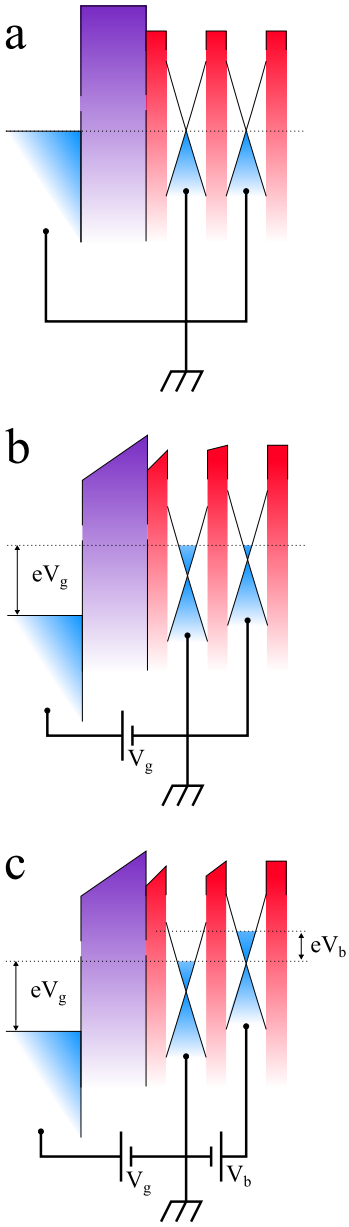

Figure 4.6: Schematic of a graphene/hBN/graphene device and band structure alignment under applied voltages **a** Supposed band structure alignment without any voltages applied. **b**The influence of an applied gate voltage V_g, between sample and the silicon backgate. **c** The influence of both the gate voltage and an applied bias V_b, between the two graphene layers. *This figure is reproduced from Britnell et al. (2012)*[a].

4.4 Modelling device operation

It is not possible to simply use the Simmons model in the case of graphene electrodes because of the field penetrating through the graphene layers. Hence a model was derived considering this quantum capacitance in a system comprised of capacitative plates. An electric field between the silicon gate electrode and the bottom graphene is denoted by $F_g = V_g/D$, where D is the combined thickness of the silicon oxide and the hBN substrate flake. A further electric field across the hBN tunnel barrier, of thickness d, is given $F_b = V_b/d$. The dielectric constants of both SiO_2 and hBN are similar and for simplicity it is assumed that $\epsilon_{SiO_2} = \epsilon_{hBN} \equiv \epsilon$.

In order to better understand the behaviour of the devices, a model was developed to calculate the shape of the σ^T curves. The general outline is that, both the gate voltage V_g and σ^T can

[a] Britnell, L. *et al.* *Science*, 335 (2012) 947–950.

[21] Kharche, N. & Nayak, S. K. *Nano Letters*, 11 (2011) 5274–5278.

[22] Xu, Y. N. & Ching, W. Y. *Physical Review B*, 44 (1991) 7787–7798.

be determined as functions of top layer carrier concentration n_T. The equations are then parametrised with values of n_T known from experiments.

Modelling the behaviour of the system is done by considering three conductive regions, separated by two dielectrics, as shown in fig. 4.8 as capacitive plates. Where both the dielectric constant of both barriers is given by $\epsilon_{SiO_2} = \epsilon_{hBN} \equiv \epsilon$. The bottom plate will be the gate electrode, while the middle and top plates, graphene with chemical potentials $\mu_{B,T}$ dependent on the respective carrier concentrations $n_{B,T}$.
Firstly looking fig. 4.7 for a voltage V_g between the the gate and bottom graphene electrodes.

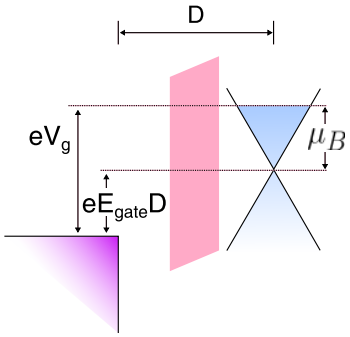

Figure 4.7: The field between the bottom graphene and gate electrodes.

$$eV_g = eE_{gate}D - \mu_B(n_B) \tag{4.1}$$

where E_{gate} is the field between the plates. Gauss's law gives the field for two parallel plates as $E_{gate} = \frac{-en_B}{\epsilon}$ and hence

$$eV_g = \frac{-e^2 n_B D}{\epsilon} - \mu_B(n_B) \tag{4.2}$$

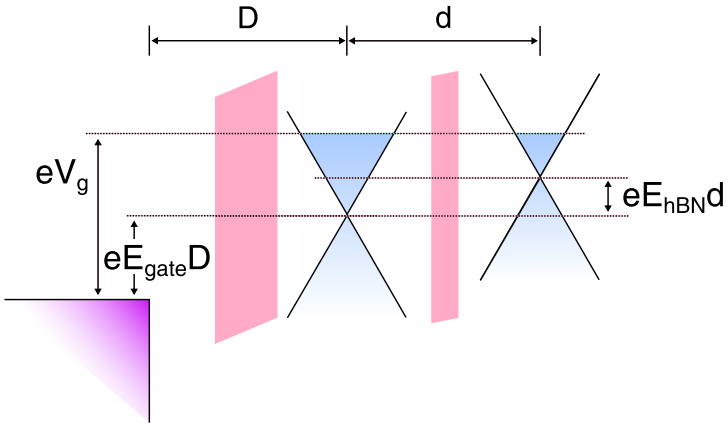

Figure 4.8: The total schematic diagram of the tunnelling transistor.

Now, also considering the top graphene electrode, fig. 4.8. The generalisation of the situation above gives the carrier concentration induced in the bottom graphene layer due to the total field across the gate E_{gate} and tunnel barrier E_{hBN}.

$$(E_{hBN} - E_{gate}) = \frac{en_B}{\epsilon} \tag{4.3}$$

where $E_{gate} = \frac{V_g}{D} = \frac{-en_{total}}{\epsilon}$ and the field penetrating through the barrier gives

$$E_{hBN} = \frac{-en_T}{\epsilon} \tag{4.4}$$

The total induced charge must be $n_{total} = n_B + n_T$. The equation for the potential between the graphene layers is

$$eV_b = eE_{hBN}d - \mu_T(n_T) + \mu_B(n_B) \tag{4.5}$$

Using the condition of electron-hole symmetry $\mu(-n) = -\mu(n)$ and the equations (4.3) and (4.4) into equation (4.5) gives

$$eV_b + \frac{n_T e^2 d}{\varepsilon} + \sqrt{n_T \pi}\hbar v_F + \sqrt{(n_T + \frac{\varepsilon V_g}{eD})\pi}\hbar v_F = 0; \tag{4.6}$$

Now taking the general equation for tunnelling

$$I(V_b) \propto \int DOS_B(E) DOS_T(E+eV_b) T(E) [f(E-eV_b) - f(E)] dE, \tag{4.7}$$

where $f(E)$ is the Fermi-Dirac distribution, it is possible to calculate all parts in terms of n_T. However, a form for $T(E)$ is still needed. The probability is related to the dispersion relation of the barrier material and for an isotropic barrier one can use $T(E) \propto \exp(-2d\sqrt{2m\Delta}/\hbar)$.
With the above equations it is possible to parametrise both the current I and the gate voltage V_g with known values of the carrier density n_T and implemented in mathematical software in order to plot the red curves shown in figs. 4.4 and 4.5.

4.5 Conclusions

In this chapter, results from two graphene/hBN/graphene tunnelling devices have been presented. The devices exhibited quantum mechanical tunnelling of holes between the electrodes under an applied bias. The $I(V_b)$ curves are linear close to zero bias but become exponential at higher bias. The magnitude of this tunnelling current can be modulated by a gate voltage V_g which is maximum near $V_b = 0$ and the observed switching ratios at room temperature are greater than those reported for graphene elsewhere. The switching ratios are modest in comparison with that required by industry due to a relatively weak $T(E)$ dependence and so the current modulation is dominated by the changes in the DOS in both graphene layers. There is the possibility to improve this by using a tunnel barrier with smaller band gap so that the shift of the chemical potential can be comparable to the barrier and hence a stronger $T(V_g)$ dependence.

Chapter 5

Disorder induced negative differential resistance in graphene-boron nitride heterostructures

The $I(V_b)$ characteristics of devices with the same architecture as described in chapter 4 have been investigated at higher bias. It was found that these devices exhibited a distinct peak and regions of negative differential conductance which is attributed to a resonant tunnelling mechanism. This is modelled using the Bardeen Hamiltonian transfer method. My contribution to this work involved the measurement of electronic transport properties and subsequent analysis of the data. I also the determined the thicknesses of the various layers by AFM and Raman spectroscopy.

5.1 Introduction

In the previous chapter it was shown that heterostructures formed by layering graphene and hBN resulted in devices that allowed modulation of a tunnel current between the graphene electrodes around zero bias by applying an external gate voltage. This chapter will discuss more exotic features observed in the $I(V_b)$ curves of some devices at higher bias.

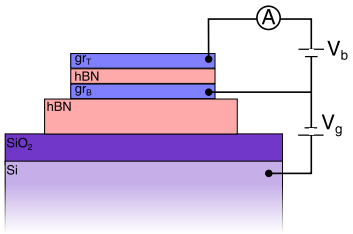

Figure 5.1: Schematic diagram of a negative differential conductivity device with the voltage conventions labelled. The setup is the same as in the previous chapter. A tunnel current is measured between graphene electrodes and the effect is gate dependent.

A gate dependent peak in the tunnel current was observed at bias values greater than a few hundred mV which is attributed to a resonant tunneling mechanism. Negative differential conductivity (NDC) is observed and the conductivity has a peak/valley ratio of up to 3 at liquid helium temperatures and the NDC survives up to room temperature. Both the position and lineshape of the peak are dependent on gate voltage. The observed phenomena has been predicted[1] and is described by a model based on the Bardeen transfer Hamiltonian approach[2]. The theoretical simulations presented here were performed by L. Eaves and co-workers at the University of Nottingham[3,4].

[1] Feenstra, R. M., Jena, D. & Gu, G. *Journal of Applied Physics*, 111 (2012) 043711.

[2] Bardeen, J. *Physical Review Letters*, 6 (1961) 57–59.

[3] Eaves, L., Greenway, M. T. & Fromhold, T. M. Private Communication (2012).

[4] This model will be discussed but should not to be attributed to the author.

In order to describe the experimental data, the model takes into account both a resonance effect as the Dirac cones in the two layers align and an elastic scattering mechanism. The nanometer scale separation of the electrodes mean these NDC devices have potential to work at high frequency and have applications in digital electronics, where their multi-valued $I(V_b)$ can be used for logic. They also have applications in analog electronics where they can be used as high frequency oscillators.

Resonant tunneling is usual considered in systems where a confined[5] region is isolated from electrodes on either side by a tunnel barrier. As bias between the electrodes is increased, the chemical potential in the electrodes will coincide at certain points with the discrete energy levels of the confined region, giving states for the electrons to tunnel through. This results in a peak in the $I(V_b)$ curves. In the graphene/hBN/graphene devices shown presently, a similar effect is observed but without the electrons needing to tunnel through discrete energy levels. It is also possible to tune the position of this current peak in the $I(V_b)$ with a gate electrode.

[5] Confined in the quantum mechanical sense so that energy levels become quantized. NDC has been heavily studied in double quantum well structures in III-V materials[6]

[6] Mizuta, H. & Tomonori, T. *The Physics and Applications of Resonant Tunnelling Diodes*. Cambridge Unversity Press (1995).

The devices are similar to those discussed in chapter 4 but are schematically shown again for clarity in figure 5.1. As before, a thick hBN flake (20-50 nm) was deposited on the oxidised surface of a doped Si substrate using the 'scotch tape' technique. The hBN again acts as a high-quality substrate[7] on which the rest of the device is placed. This actual device consists of two graphene electrodes on either side of a thin hBN flake which acts as a tunnel barrier. These devices were again, all produced by the *dry transfer* technique as described in chapters 1 and 3 with the hBN tunnel barrier thickness being measured by a combination of AFM and optical contrast.

[7] Dean, C. R. *et al. Nature Nanotechnology*, 5 (2010) 722–726.

A tunnel current I is generated when a bias voltage V_b is applied between the two graphene electrodes. The gate voltage V_g is applied between the doped Si and the bottom graphene, shown in fig. 5.1. As was discussed in the previous chapter, the use of graphene distinguishes these devices from those based on conventional semiconductor heterostructures as the low DOS close to the Dirac point means the electric field from the gate is only partially screened. Thus, the gate voltage changes the carrier density in the both graphene electrodes.

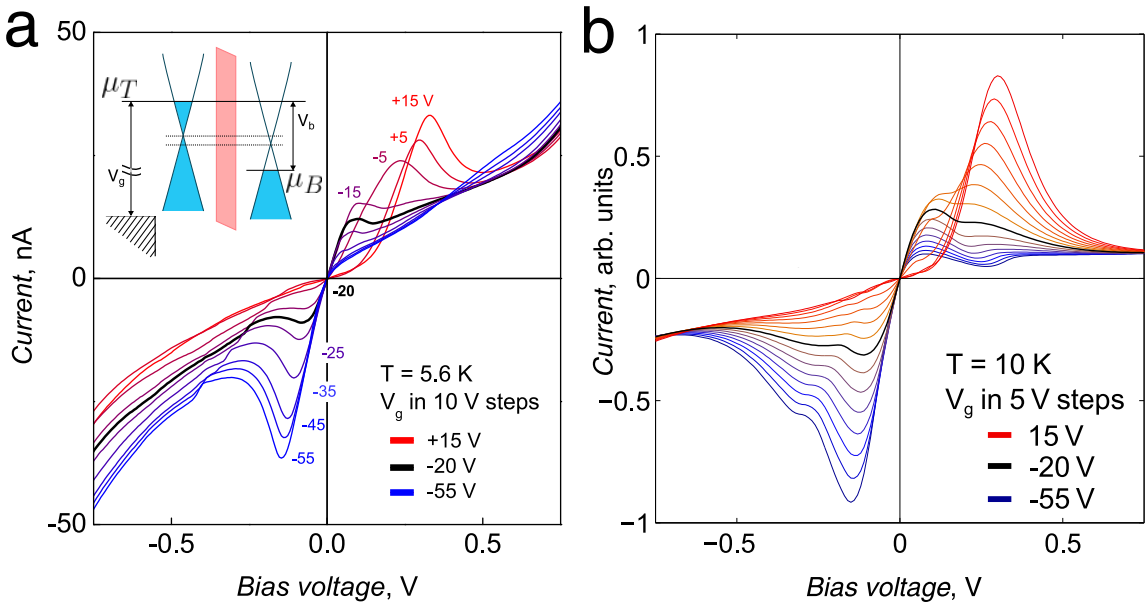

Figure 5.2: **a** Experimental low-temperature negative differential conductivity $I(V_b)$ characteristics for device (1) with a 4 layer hBN (∼1.4 nm) tunnel barrier and a 0.3 µm^2 overlap area of the graphene electrodes. The measurement temperature was 5.6 K. The $I(V_b)$ are taken at gate voltages in 10 V steps ranging from -55 to +15 V with the addition of the symmetric curve at V_g=-20 V, corresponding to the case where the gate induced charge equals the remnant doping in graphene layers. The inset shows the doping levels of the graphene electrodes for the +15 V curve. **b** Data simulated from theory using the Bardeen Hamiltonian model using q_c= 12 nm and initial n-doping (4.4×10^{11} cm^{-2}) of the bottom layer and p-doping (1.0×10^{12} cm^{-2}) of the top layer.

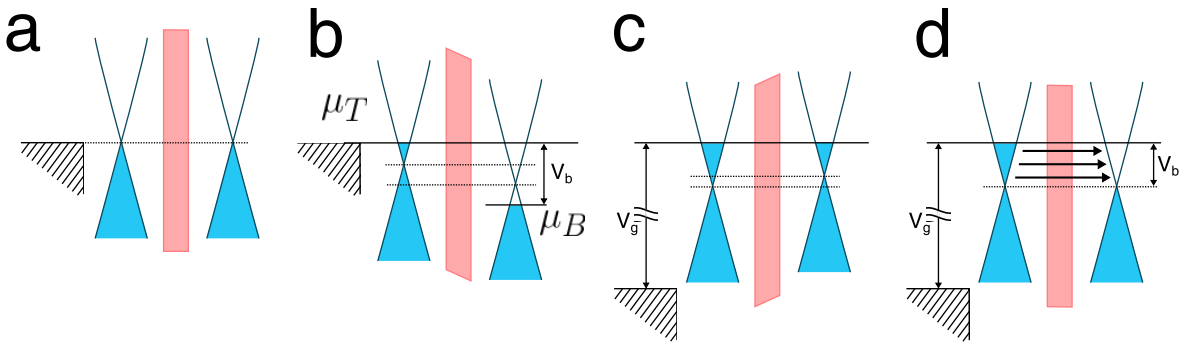

Figure 5.3: **a** In the absence of gate and bias voltage, the chemical potentials are aligned with the Dirac points. **b** With applied bias electrons (holes) collect in the negative (positive) electrode and a field is present across the tunnel barrier. **c** With gate voltage the chemical potential is shifted in both layers and an electric field present across the tunnel barrier. **d** With gate voltage applied, the graphene bands are aligned for finite bias and the resonant peak is seen.

The discussion will centre around two devices. The first device, denoted device (1), has a 4 layer hBN tunnel barrier (∼1.4 nm) and a cross sectional area of 0.3 µm^2. Fig. 5.2**a** shows $I(V_b)$ data measured at 5.6 K on device (1) for a range of V_g from -55 V to +15 V. Clearly visible is a peak in the current, which at V_g=+15 V, has a position close to +0.3 V. It is also quite clear that the position and amplitude of the peak are gate dependent; the peak moving to -0.1 mV at V_g=-55 V, with no peak any longer visible on the positive bias voltage side. The region of NDC extends for about 200 mV from V_b=0.3-0.5 V for the V_g=+15 V where the curve is higly asymmetric with a single peak for positive V_b. As the V_g is decreased the curves approach

symmetry at V_g ∼-20 V, the thicker black line. The resonance is now centred at V_b ∼0 V with the peak split equally between the positive and negative bias values. Note, while the width of the resonance is approximately constant, the peak/valley ratio reaches a minimum in the symmetric case at V_g =-20 V.

The peak/valley ratio for device (1) is plotted in fig. 5.4 where it is seen that as the ratio decreases for one polarity it increase for the other with a minimum in the symmetric case. In fig. 5.2**b** are curves from the theoretical simulations which are based on the Bardeen transfer Hamiltonian approach[8,9] as described below. There is a strong similarity between the simulations and the experimental data, suggesting the proposed mechanism is correct. The peak/valley ratio is smaller for the experimental data which can be due to current leakage.

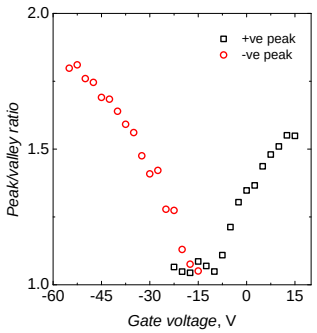

Figure 5.4: Peak/valley ratio for resonance peaks in graphene/hBN/graphene tunnel device (1).

[8] Feenstra, R. M., Jena, D. & Gu, G. *Journal of Applied Physics*, 111 (2012) 043711.

[9] Eaves, L., Greenway, M. T. & Fromhold, T. M. Private Communication (2012).

5.1.1 A physical description of the model

In order to understand the physical origin of the NDC features observed in the devices, the idealised case is considered initially.[10]

In the ideal case there are two separated, crystallographically aligned graphene layers which are undoped when V_b=V_g=0 V. In this case the chemical potential μ_T (top) and μ_B (bottom) in both layers coincides with the Dirac points of each layer, i.e., they are all at the same energy as in fig. 5.3**a**. For a device of this type (when biased) electrons will collect in the negative electrode and holes in the positive electrode creating an electric field and placing a shift between the positions of the Dirac points in each layer, fig. 5.3**b**. The band structure misalignment means a carrier tunneling from one electrode to the other must change its in-plane wavevector $\boldsymbol{k}$ due to momentum conservation. The condition of momentum conservation can be relaxed if a scattering process is allowed. Although the scattering mechanism has not been determined, it is seen in conventional double well structures that disorder and interaction effects can produce such effects[11]. With the application of a gate voltage, fig. 5.3**c**, the bands in each graphene layer will initially be offset from one another and the bias voltage brings them back into alignment and the current peak is seen, fig. 5.3**d**. Thus for a range of gate voltages, different bias voltages will be needed to realign the bands resulting in the shift of the resonance peak, as seen in fig. 5.2.

[10] Although the theoretical simulation qualitatively describes the data, it is necessary to take into account a couple of other factors to replicate the experimental data.

[11] Eisenstein, J. P., Pfeiffer, L. N. & West, K. W. *Physical Review Letters*, 69 (1992) 3804–3807.

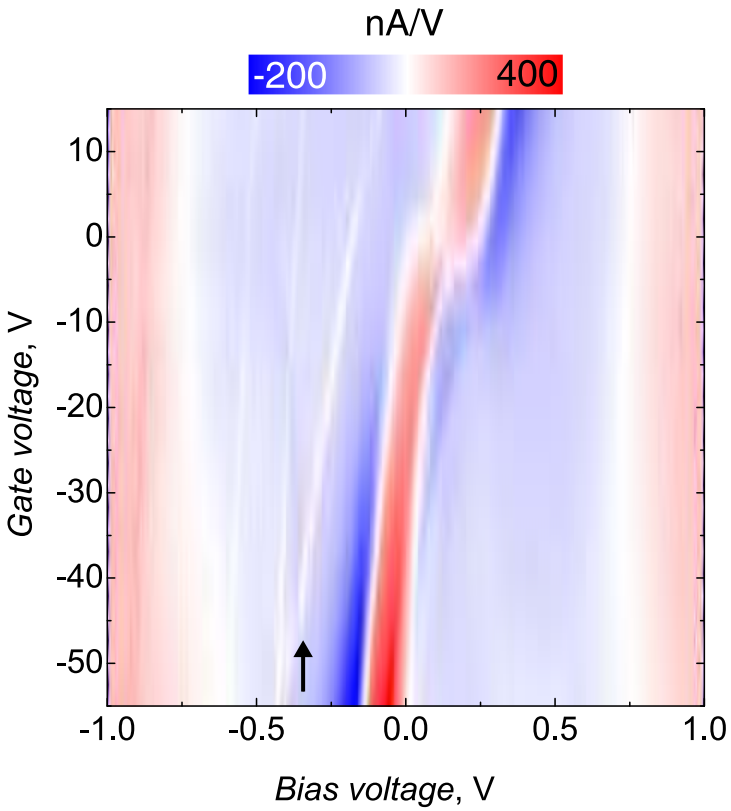

Figure 5.5: A V_g-V_b map of differential conductivity for the data shown in fig. 5.2

5.2 Theoretical modelling - scattering potential and doping effects

An electron tunnelling between misaligned bands needs a change $\boldsymbol{q}$ in its in-plane wavevector $\boldsymbol{k}$ which can be disorder induced. It is assumed that such disorder exists in these devices and can be described by a scattering potential $V_S(\boldsymbol{q})$ where the shape of the scattering potential dictates the form of the resonance curve. A Gaussian dependance was used to model the experimental data. The shape of the potential gives a maximum allowable momentum change $\boldsymbol{q}_c$, the reciprocal of which gives a limit on the real space variation of the potential. The model itself uses the Bardeen formulation with a scattering potential of the form $V(\boldsymbol{q}) \sim \frac{1}{q_c^2+q^2}$ where $\boldsymbol{q}_c^{-1}$ =12 nm. The model as described, see fig. 5.2**b**, qualitatively describes the behaviour of device (1). It is symmetric around the point V_g=0 V, which is not the case for the experimental data shown in fig. 5.2**a**. However, by considering residual doping of the graphene layers a decent quantitative fit can be found. The doping values needed to fit the data were 4.4× 10^{11} cm^{-2} (n-type) for the bottom layer and 1.0× 10^{12} cm^{-2} (p-type) which correspond to shifts in the Fermi level of 80 and -110 meV respectively. These are resonable values, considering the processing steps in device fabrication.

With these conditions satisfied a peak in $I(V_b)$ can now appear because the Dirac cones are aligned when a bias voltage is applied, meaning there are many empty states with the same momentum available for the electrons to jump into. Further features are visible in the differential conductance map in fig. 5.5 where a shoulder is visible on the peaks which can be attributed to the case when the Dirac point of one electrode is aligned with chemical potential of the other layer. Around this point, the current will be insensitive to V_b because the number of accepter (or emitter) states varies little due to a vanishing density of states. The vertical trace indicated by the arrow is the point where the μ_T passes the Dirac point in the bottom graphene layer.

So far it has been assumed that the two graphene layers are crystallographically aligned but there is no experimental evidence for this in our devices. However, if rotational misalignment is taken into account in the model, it is found that it is only the magnitude of $I(V_b)$ that is affected, not the shape and so the features should be observable in any case. It is now technologically possible to engineer crystallographically aligned graphene electrodes[12] but this was not done in this case. It would be the aim of further work to understand how the alignment affects the results.

[12] Yankowitz, J. X. M. *et al. Nature Physics*, 8 (2012) 382–386.

The model presented by Feenstra *et al.*[13] also predicts resonant tunnelling in the case where graphene is nanocrystalline. That is to say, within each electrode many different crystal orientations are present. Although the structure of the graphene electrodes for these devices was not investigated, it is unlikely to be the case here. The high quality graphite and mechanical clevage which produced the graphene for these devices always results in single crystal flakes, evidenced by their edges having common crystal directions and their high mobility.

[13] Feenstra, R. M., Jena, D. & Gu, G. *Journal of Applied Physics*, 111 (2012) 043711.

A further example of such behaviour was observed in device (2). Low temperature $I(V_b)$ of device (2) is shown in fig. 5.6**a**. Similar features to those discussed with respect to device (1) are observed; including the NDC and resonant peak. The shoulder, although visible, is less distinct. In fig. 5.6**a** the $I(V_b)$ measured for V_g in the range -60-+20 V is displayed. Again, the shift from symmetry at $V_g = 0$ is attributed to residual doping, with the symmetric curve lying between -30< V_g <-20 V. Alongside the low temperature data in fig. 5.6**b** is room temperature data for the same device. Notably, the NDC survives up to 300 K but the peak/valley ratio decreases as the overal current increases due to the extra thermal energy of the carriers.

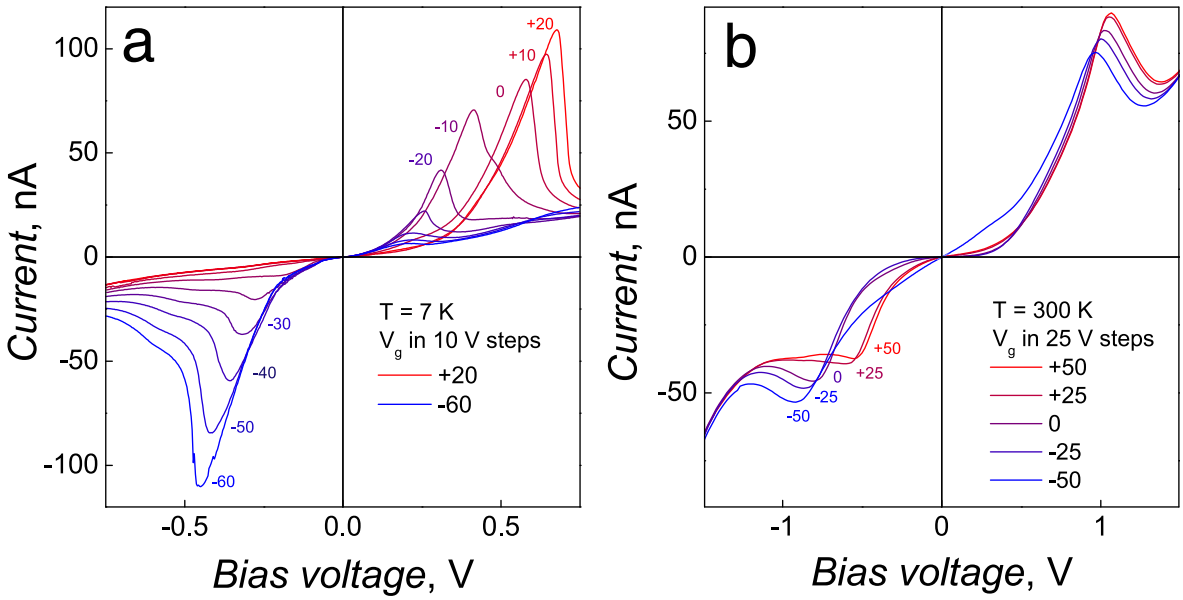

Figure 5.6: **a** Experimental low-temperature negative differential conductivity $I(V_b)$ characteristics for device (2) with a 5 layer hBN tunnel barrier and a 0.6 μm^2 overlap area of the graphene electrodes. The measurement temperature was 7 K. The $I(V_b)$ are taken at gate voltages in 10 V steps ranging from -60 to +20 V. **a** Room temperature data for the same device showing the NDC survives although the peak/valley ratio is decreased.

5.3 Conclusions

These graphene/hBN/graphene devices exhibit distinct NDC features at bias voltages between 0.1 and 1 voltage, with the position of the peak tunable between positive and negative bias voltage by application of a voltage to a gate electrode. The NDC is due to alignment of the Dirac cones in each graphene layer and can be present even in the case of misaligned graphene lattices. The experimental data is well replicated by simulations using the Bardeen Hamiltonian matrix method. Development of these devices would be beneficial because they overcome some of the problems encountered by conventional NDC devices such as the dwell time where the electron resides inside the quantum well for a finite time. Tunnelling times are on the order of femtoseconds and so these devices may have applications in high-frequency electronics although the operating frequency of the devices remains to be investigated and will certainly be lowered with the unavoidable effect of parasitic capacitance and resistance in the load circuit.

Chapter 6

Photodetection in graphene-WS_2 heterostructures

In this chapter it will be shown that graphene-WS_2 heterostructures can be utilized for photodetection and light harvesting. These devices are comprised of two graphene electrodes sandwiching a photoactive WS_2 crystal. Using scanning photocurrent microscopy and tunnelling spectroscopy it was observed that the structures were strongly photoactive with a photoresponsivity above 0.1 A/W, corresponding to an external quantum efficiency of 30%, which makes them promising for solar harvesting and photodetection applications. The architecture of such devices and the possibility to use CVD-grown graphene for the heterostructures should allow for large scale integration.

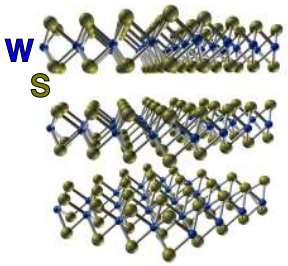

Figure 6.1: The crystal structure of WS_2.

6.1 Introduction

Transition metal dichalcogenides (TMDCs) form a group of layered materials that is currently attracting interest because of their photonic and electronic properties. Two examples, molybdenum disulfide and tungsten disulfide are photoactive and of particular interest because monolayers posses a direct band gap and strong photoluminescence[1]. Importantly here, WS_2 has potential use in solar cells due, in part, to the size of its band gap (1.8/1.3 eV direct/indirect gap[2,3]) and its large optical absorption[4,5], which is greater than 10^7 m^{-1} across the visible range, meaning 95% of the light can be absorbed by a 300 nm film. A further advantage of WS_2 is its chemical stability; meaning it does not undergo photocorrosion[6].

Previously, thick planar WS_2 structures were studied for solar harvesting[7]. However, efforts to extract photocurrent were hampered by the need to create a pn junction to separate the electron-hole (e-h) pairs, created by incoming photons. With vertical 2D-crystal based heterostructures, a beneficial combination of each materials properties emerges: WS_2 as a good photoactive material and graphene as a good transparent electrode. Using a graphene/WS_2/graphene stack with

[1] Gutiérrez, H. R. *et al. arXiv:1208.1325*, (2012).

[2] Kam, K. K. & Parkinson, B. A. *Journal of Physical Chemistry*, 86 (1982) 463–467.

[3] Wilson, J. A. & Yoffe, A. D. *Advances in Physics*, 18 (1969) 193–335.

[4] Kumar, A. & Ahluwalia, P. K. *European Physical Journal B*, 85 (2012) 186.

[5] Chatzitheodorou, G. *et al. Materials Research Bulletin*, 23 (1988) 1261–1271.

[6] Tributsch, H. *et al. Phys. Chemie*, 83 (1979) 1655.

[7] Ballif, C. *et al. Applied Physics A: Materials Science & Processing*, 62 (1996) 543–546.

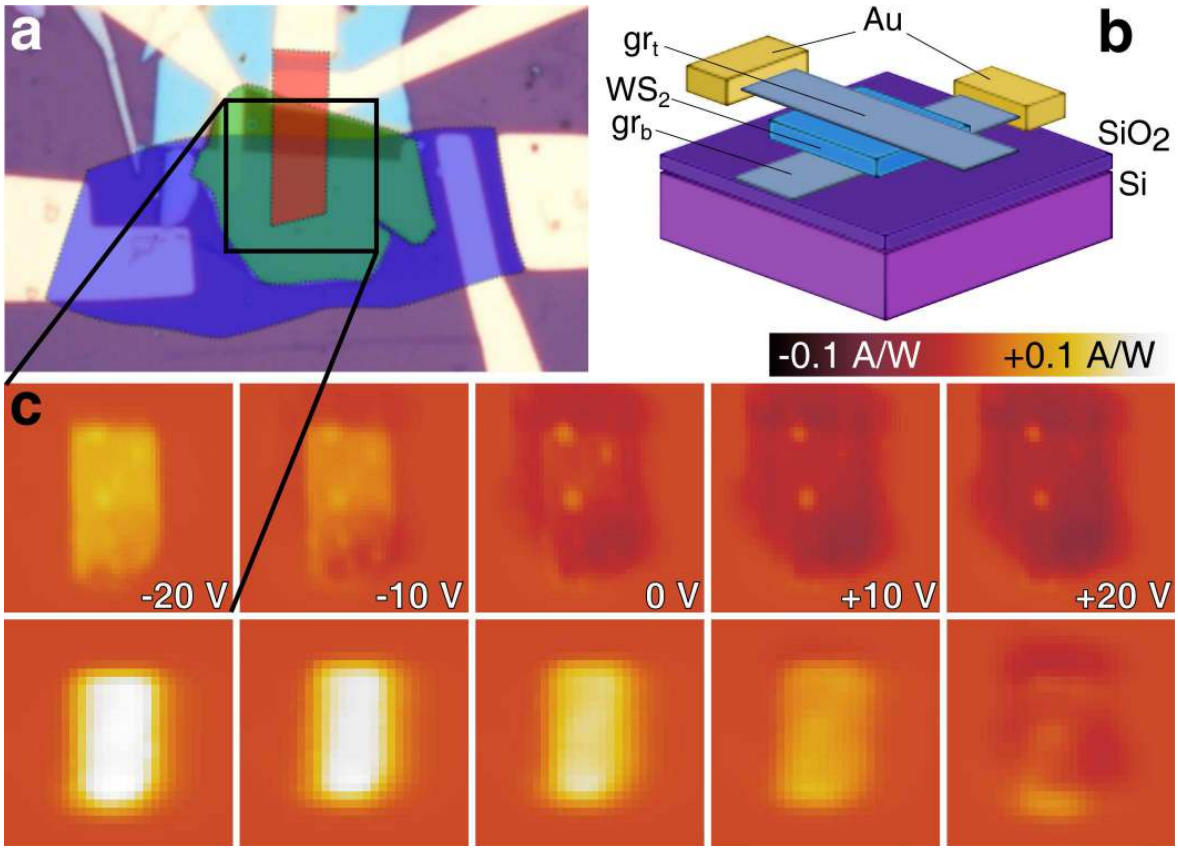

Figure 6.2: **a** An optical micrograph of one of our devices. The shading of the three constituent layers denotes the regions of the respective materials top and bottom graphene electrodes shown in red and blue, while WS_2 is shown in green and for clarity. **b** A schematic cartoon of the device with the principal layers shown. hBN is not shown. **c** photocurrent maps taken before (above) and after (below) the device was stored in a humid atmosphere to change doping. A signal is only seen in the area where all three layers overlap. The two graphene layers were connected via 1 kΩ resistor, on which the photocurrent was measured. No bias was applied.

appropriately positioned Fermi levels and simply doping the two graphene layers differently (either by electrostatic gating or chemical methods) leads to large photocurrent. The layered nature of the structures means it is possible, in principle, to fabricate large area light harvesting devices. Without illumination, such devices act as tunnelling transistors[8].

[8] Britnell, L. *et al.* *Science*, 335 (2012) 947–950.

6.2 Methods

Graphene and thin graphite flakes were produced by micromechanical exfoliation of graphite. Single crystal WS_2 supplied in powder form by Sigma-Aldrich was used for mechanical exfoliation. Despite an average crystal size of only 2 µm it is possible to find crystals up to 50 µm that could be exfoliated as well.

Recent progress has led to relatively facile fabrication of graphene hybrid devices with a large degree of versatility[9,10,11]. The method allows flakes of layered materials to be transferred to the surfaces of one another with a high degree of accuracy and cleanliness. In this way, stacks of different materials can be created with precise control over the constituents of the new hybrid material.

[9] Dean, C. R. *et al.* *Nature Nanotechnology*, 5 (2010) 722–726.

[10] Ponomarenko, L. A. *et al.* *Nature Physics*, 7 (2011) 958–961.

[11] Britnell, L. *et al.* *Science*, 335 (2012) 947–950.

The *dry transfer* technique[12,13] was used to create these structures. This technique involves the mechanical exfoliation of the required flakes onto a dual layer polymer stack. The bottom polymer layer can be selectively dissolved and the resulting membrane inverted and positioned above the target flake. The initial bottom flake was instead cleaved onto a Si/SiO_2 wafer (290 nm oxide). After each transfer the top polymer layer was dissolved and the device annealed thoroughly in a gaseous mixture of H_2/Ar (10:90) at 250°C before the subsequent transfer of the next flake. In this way, stacks with an arbitrary number of layers could be produced. Once the required flake stack had been fabricated, electrical contact was made via standard photolithographic processing and e-beam evaporation of a Cr adhesion layer (5nm) and Au (50 nm) and placed in a package for measurements.

[12] Dean, C. R. *et al.* *Nature Nanotechnology*, 5 (2010) 722–726.

[13] Ponomarenko, L. A. *et al.* *Nature Physics*, 7 (2011) 958–961.

In order to make scanning photocurrent microscopy measurements (section 2.4) we utilize a WITec scanning Raman system. The sample was placed onto a piezoelectric stage with laser light incident from above. The laser was focussed by a x100 microscope objective with a laser spot size that is diffraction limited (diameter 500 nm). The laser spot is scanned over the

surface and the resultant current flow between the two graphene electrodes is measured simultaneously with the Raman spectra for each point in the scan.

6.3 Results

Demonstrated here are devices comprising three principal layers top and bottom graphene electrode layers sandwiching a photoactive WS_2 layer, (see the optical image fig. 6.2 and a cartoon schematic, fig. 6.2**b** of one of our devices). The three important regions are shaded for clarity (red/blue are top/bottom graphene electrodes respectively and green is the WS_2 photoactive region). In the fabrication procedure, the flakes were transferred using the *dry transfer* technique[14,15] with thorough annealing (see section 6.2) at each stage to ensure minimal contamination between the layers[16] and low level doping of the graphene layers. hBN was chosen as both a substrate and an encapsulating layer to achieve a higher doping homogeneity[17,18]. Thus, the final structure of a typical device, on top of an oxidised silicon wafer, was hBN/graphene/WS_2/graphene/hBN. Here, the doped silicon could be used as a back gate and SiO_2/hBN the gate dielectric. A series of such structures was produced where the thickness of the WS_2 layer was varied from ∼5-50 nm. Devices with WS_2 thickness of ∼20 nm were chosen for the devices presented here because they were found to absorb a decent proportion of incident photons and allow full characterisation by tunnelling spectroscopy.

[14] Dean, C. R. *et al.* *Nature Nanotechnology*, 5 (2010) 722–726.

[15] Ponomarenko, L. A. *et al.* *Nature Physics*, 7 (2011) 958–961.

[16] Haigh, S. J. *et al.* *Nature Materials*, 11 (2012) 764–767.

[17] Dean, C. R. *et al.* *Nature Nanotechnology*, 5 (2010) 722–726.

[18] Mayorov, A. S. *et al.* *Nano Letters*, 11 (2011) 2396–2399.

The $I(V_b)$ characteristics of the samples strongly depended on illumination, see fig. 6.3**a**. Without illumination, the devices displayed strongly non-linear $I(V_b)$ curves (fig. 6.3**b** inset where transistor behaviour can be seen. The on-off ratio for this device was $\sim 10^3$). Comparing this with the main figure, one can see that this was in strong contrast to when they were illuminated: the resistance dropped by more than 3 orders of magnitude and the curves became linear around zero bias. At higher bias ($\sim \pm 0.2$ V) they began to saturate, as the number of available charge carriers in the photoactive region was limited.
To elucidate further, the photocurrent generated in our devices was mapped by scanning photocurrent microscopy (section 2.4), where a laser spot was scanned over the sample, and the resultant photocurrent displayed as a function of laser spot position. In fig. 6.2**c** one can see that a current is generated only in the region where all three principal layers overlap. With reference to fig. 6.3**b**, we explain the origin of the photocurrent by examining the collective band diagram. In the ideal case the

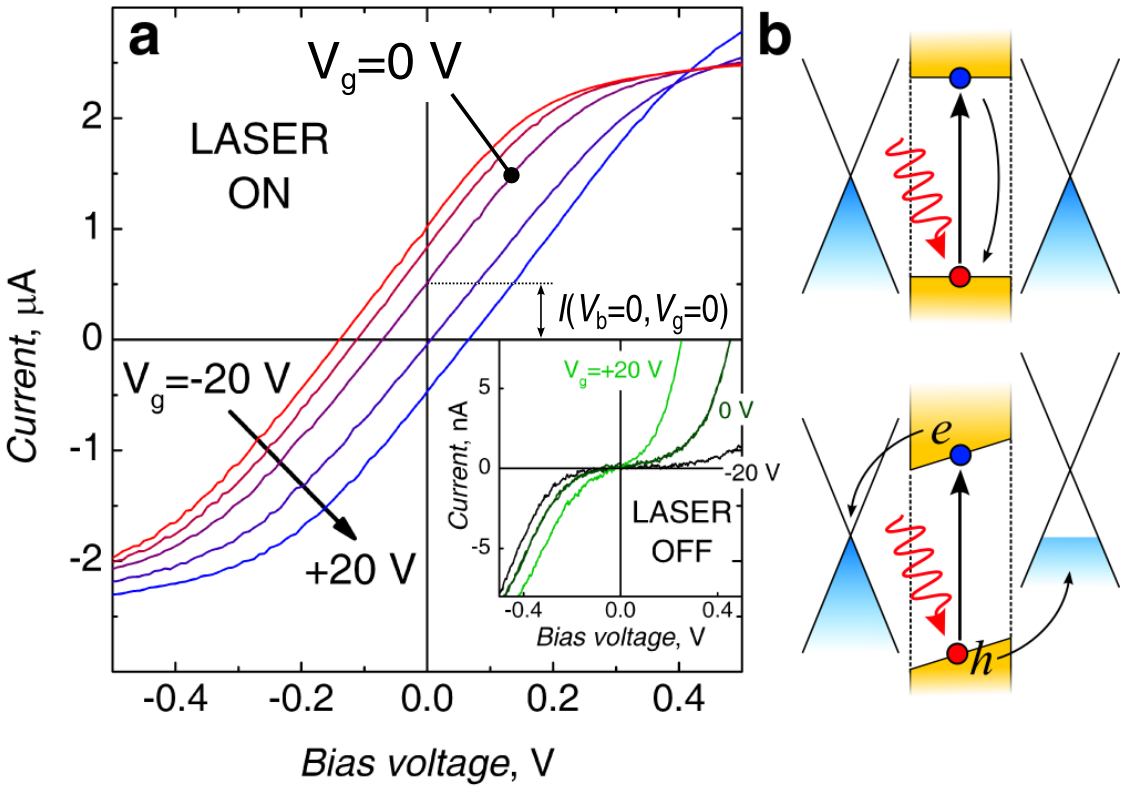

Figure 6.3: **a** $I(V_b)$ curves taken at gate voltage values from -20 to $+20$ V in 10 V steps, as signified by the arrow, after doping. The $V_g = 0$ curve is labelled and note the offset in the absence of either gate or bias voltage. The laser illumination energy was 2.54 eV and the power 10 μW. The curves are linear at low bias but saturate at higher bias due to limited available charge carriers. The inset shows $I(V_b)$ curves taken without illumination at $V_g = 0, \pm 20\ V$, the current undergoes a large modulation with gate voltage. **b** Schematic band diagram for Gr/WS_2/Gr heterostructure with and without a built-in electric field to separate the generated e-h pairs.

structure is symmetric (fig. 6.3**b** top) and the electrons/holes generated in WS_2 (by absorption of a photon with sufficient energy) will have no preferred diffusion direction and hence no net photocurrent is measured. However, in the presence of a built-in electric field (fig. 6.3**b** bottom) across the WS_2 (either due to a difference in the initial doping between the graphene sheets or by gating[19]), the e-h pairs will be separated and a photocurrent measured.

[19] Britnell, L. *et al.* *Science*, 335 (2012) 947–950.

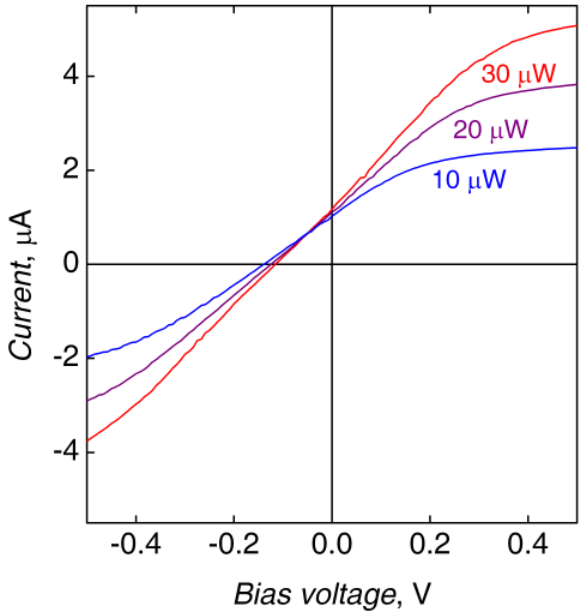

Figure 6.4: $I(V_b)$ characteristics of the device shown in fig 2, under laser illumination of varying intensity. The resistivity of the device changes only when laser light is incident on the region where all three constituent flakes overlap and the slope of the $I(V_b)$ curves is dependent on the power. Shown are $I(V_b)$ curves taken with a 2.54 eV laser set to a total power of 10, 20 and 30 μW, all at $V_g = -20\ V$. The power was always measured under the objective with a 0.5 μW precision.

The effect was investigated by taking photocurrent maps at different gate voltages V_g, see fig. 6.2**c**. Immediately after fabrication and subsequent annealing, the devices showed a minimum in the integrated photocurrent close to zero gate voltage (fig 6.2**c**, upper panels, the same can be seen in fig. 6.3**a**). For any finite V_g (either positive or negative) the photocurrent increased proportionally to V_g but began to saturate at $\sim \pm$ 20 V, again due to the finite number of generated charge carriers. After leaving a non-encapsulated sample in a humid atmosphere for 1 day the photocurrent maps were retaken (6.2**c**, bottom panels). The photocurrent at zero gate voltage became finite (positive) and the response with gate voltage was shifted by $\sim$ 20 V. The effect is also seen in fig. 6.2**a** where the intercept of the $I(V_b)$ curves is shifted due to movement of the chemical

potential in graphene. In general our devices also showed a strong gate dependence without illumination, which allows them to be used as tunnelling transistors[20]. The highest measured *on-off* ratio (highest to lowest current modulation) for the devices was 10^3.

[20] Britnell, L. *et al.* *Science*, 335 (2012) 947–950.

The performance of these prototype light harvesting devices was also investigated. For power generation, an important parameter is the extrinsic quantum efficiency (EQE), defined as the ratio of the number of charge carriers generated to the number of incident photons. This can be expressed in terms of the photocurrent I, incident power per unit area P and excitation wavelength λ by

$$EQE = \frac{hc}{e\lambda}\frac{I}{P} \tag{6.1}$$

where h is the Planck constant, c the speed of light in vacuum and e the electron charge. Fig. 6.4 shows the effect on the $I(V_b)$ characteristics, of irradiance with different intensities. Again, all measured $I(V_b)$ curves were linear in the low bias regime and with slopes dependent on the illumination intensity. Using the relation for EQE one can calculate the efficiency, shown in fig. 6.5, where the data were collected for several wavelengths at zero bias and $V_g = -40$ V. The extrinsic quantum efficiency did not appear to be dependent on wavelength, as expected from the approximately constant optical absorption, over this range[21]. It is likely that the decrease in quantum efficiency with increasing power is due to screening of the built-in electric field by the excited electrons in the conduction band of WS_2. To improve performance it is proposed that either a thicker WS_2 layer should be used or multiple structures stacked upon each other in order that all incident light is absorbed within the device, pushing EQE even higher.

[21] Ballif, C. *et al.* *Applied Physics A: Materials Science & Processing*, 62 (1996) 543–546.

6.4 Conclusions

It has been shown that the fabrication of graphene-WS_2 hybrid devices allows the production of prototypical efficient solar cells. It is possible to reach an extrinsic quantum efficiency of 30% which is expected to be higher under lower intensity illumination (e.g. solar radiation) and by optimizing the device design. The photocurrent generated was seen to be almost independent of wavelength from 488 to 633 nm. The same device can be used as a transistor and has *on-off* ratios exceeding 10^3. The use of various TMDCs as well as their combinations would allow one to create photovoltaic devices with sensitivity in the predetermined spectral range, suitable for large scale production.

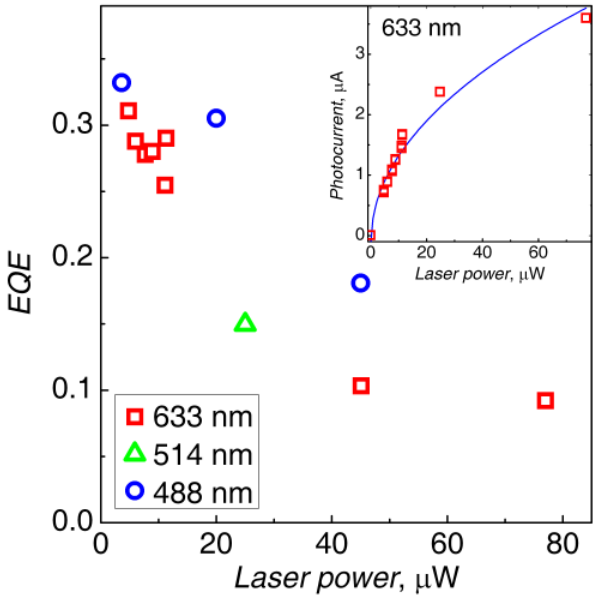

Figure 6.5: The external quantum efficiency of the devices is the ratio of the number of measured e-h pairs to absorbed incident photons. Due to the small variation in optical absorption across this wavelength range the data for different wavelengths collapse onto a single curve. The inset shows the photocurrent measured with a 1.95 eV laser as a function of intensity and follows a sublinear dependence. This results in the largest quantum efficiency values at low intensities.

Chapter 7

Concluding remarks and outlook

7.1 Conclusions

Graphene-based heterostructures have been introduced and investigation in the form of electrical, structural and optoelectronic characterisation has been presented. Starting from the study of the most basic structures comprising only two crystal layers it's been shown that hBN presents a suitable tunnel barrier for separating other conducting layered crystals such as graphene. The normalised tunnel current was observed to follow an exponential relationship with a constant ∼1.5 decades per hBN layer. The Simmons model was used to simulate the experimental data and a good agreement was found with barrier height and charge carrier effective mass (Δ=1.5 eV and m=0.5m_0 respectively). The homogeneity of hBN was investigated by conductive atomic force microscopy and it was found to be almost entirely free of defects. The fact that the tunnel current was constant across large terraces makes it an applicable tunnel barrier for electronic devices. hBN was then utilised in devices which were shown to exhibit current modulation between graphene electrodes. Although the switching ratios in these devices were modest (up to 50), they did have a low power *off* state and should work at high frequency because transit times between such closely spaced electrodes are on the order of femtoseconds. For practical application a much larger *on* current would be needed and this can be achieved by using transition metal dichalcogenides (TMDCs)[1] because movement of the Fermi level becomes comparable to their band gap. These devices also exhibited negative differential conductivity in their current-voltage characteristics which has potential use in high frequency digital and analog electronics. The peak/valley ratio was up to 3 at 4 K and still visible at 300 K. It was also shown that by replacing the hBN layer with a transition metal dichalcogenide such as tungsten disulfide resulted in a photoactive devices capable of producing a significant photocurrent. These devices have potential applications in light harvesting technologies if improvements to the external quantum effciency can be made.

[1] Britnell, L. *et al.* *Science*, 335 (2012) 947–950.

7.2 Outlook

The tunneling transistor, negative differential conductance and photovoltaic samples were all shown to exhibit decent performances for proof-of-concept devices. However, work is already being undertaken to improve their design. In the case of the tunnelling transistor, replacement of the hBN with a transistion metal dichalcogenide such as molybdenum or tungsten disulfide results in *on-off* ratios which are acceptable by industrial standards[2,3]. Further work is being undertaken to determine the source of scattering in the negative differential devices so that it can be better understood and utilised. For the photovoltaic cells, the optimal construction is being investigated so that maximum photovoltage can be obtained. This could be achieved in a couple of ways; firstly by maximising the asymmetry in doping to enhance the zero bias offset in current and secondly by decoupling the WS_2 layers so that each layer possess a direct band gap hence increasing absorption. The latter point could be acheived by either mechanically stacking multiple layers or intercalating the crystals with another species. Also possible is fabrication of repeated stacks to ensure all light is absorbed within the photoactive region. Another much sought after goal would be to reverse the process of these devices: by applying a bias between the electrodes, electrons will tunnel through the photoactive region, recombine with a hole and emit a photon. If such a light emitting diode could be fabricated then in principle it would be possible to print them using solution processing of the crystal layers. For all devices, the drive towards a scalable process for manufacture should be investigated. This could take the form of solution processing where the constituent crystals are dip cast onto each other or direct growth by methods such as chemical vapour deposition. Progess in this area is already being made. Finally, although the devices presented here are interesting in their own right, one goal of future work would be aimed at condensing the various properties into single devices. For example, a device which produces a photovoltage that could in turn drive a transistor creating a simple amplifier, could in principle be fabricated in the same sample. The inclusion of further layered crystals should result in devices with a raft of properties and applications.

[2] Britnell, L. *et al.* *Science*, 335 (2012) 947–950.

[3] Georgiou, T. *et al.* *Unpublished*, (2012).

Part III

Appendix

Appendix A

Visibility of boron nitride

A.1 Thin film interference

In this first appendix, a model is presented that allows one to calculate the optical contrast of hBN on arbitary substrates; soley using knowledge of the optical constants of the materials. The model is based on thin film interference theory[1,2]. To put it simply, by using certain rules at each thin film interface one can compute the total reflection and transmission of the system. Computing theses numbers for two systems; one with and one without hBN allows one to calculate the contrast between hBN and substrate.

[1] Hecht, E. *Optics*. Addison-Wesley (2002).

[2] Lipson, S., Lipson, H. S. & Tannhauser., D. *Optical Physics*. Cambridge Unversity Press (1995).

Thin film interference was used to describe the optical contrast of graphene on Si/SiO_2[3]. It was found that optical contrast between graphene flake and substrate could be tuned by varying the oxide thickness. In the early days of graphene research this was important because before the fabrication procedures were optimized the lateral flake dimensions tended to be on the order of microns which make them rather difficult to find by eye under low contrast conditions. As graphene flake sizes increased this became less of an issue but hBN, for instance, has a much lower contrast because its optical constants[4] are not ideal for these conditions and so a model was created to find the optimal parameters/substrates on which to find it.

[3] Blake, P. *et al. Applied Physics Letters*, 91 (2007) 063124.

[4] It should be pointed out that although it is a misnomer to refer to these parameters as *optical constants*, since for the majority of the time they are not constant over the visible range, it can be safe to make this approximation, in the case of graphene for example.

It was also found that the simplification of only considering normal light incidence was inadequate to describe hBN. Therefore, the angle of incidence was included in the model to account for these deviations from experimental observation. The microscope objectives used to find hBN have a finite numerical aperture and hence the angular dependence of the contrast is included. It is worth noting that this slightly decreases the discrepancy between observation and theory for graphene[5]. It was also found that it was more versatile to implement the matrix method[6] to calculate contrast so that an arbitary number of layers could be included in the calculation, allowing one to look at other substrates which maybe include other thin film layers.

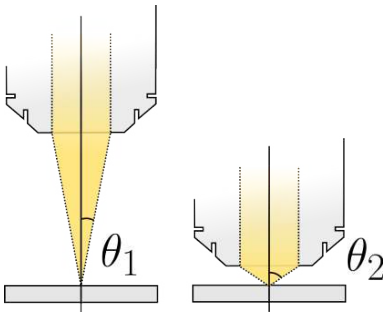

Figure A.1: Numerical aperture of a microscope lens. $\theta_1 < \theta_2$

[5] Casiraghi, C. *et al. Nano Letters*, 7 (2007) 2711–2717.

[6] Hecht, E. *Optics*. Addison-Wesley (2002).

To describe the model the treatment given by Hecht[7] is followed.

[7] Hecht, E. *Optics*. Addison-Wesley (2002).

With reference to fig. A.2, it is assumed that the system is made up of materials which have planar interfaces perpendicular to the z-axis. Materials of infinte extent in the positive and negative z direction sandwich a stack of thin films.

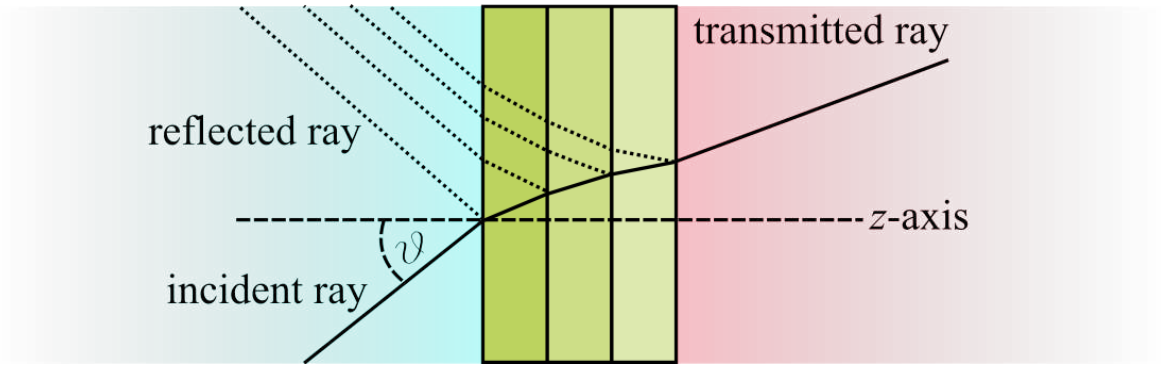

Figure A.2: A schematic for thin film interference. A wave enters from the left travelling in the positive z direction. Some proportion is reflected from the first interface while the rest is refracted towards the second interface and this process is repeated for each interface resulting in multiple reflected and refracted beams which interfere and produce the total reflected and transmitted waves.

In order to model this sytem, two boundary conditions are needed. It follows from Maxwell's equations that the tangential components of the electric E and magnetic fields H associated with beam are continuous across each interface. Hence, by denoting the first region by I and the second by II, one can state that

$$E_I = E_{iI} + E_{rI} = E_{tI} + E'_{rII} \tag{A.1}$$

and

$$H_I = \sqrt{\frac{\epsilon_0}{\mu_0}}(E_{iI} - E_{rI}) n_I \cos\theta_{iI} H_I = \sqrt{\frac{\epsilon_0}{\mu_0}}(E_{tI} - E'_{rII}) n_{II} \cos\theta_{iII} \tag{A.2}$$

through the relation

$$\vec{H} = \sqrt{\frac{\epsilon_0}{\mu_0}} n\hat{k} \times \vec{E} \tag{A.3}$$

where the subscripts i, r and t denote *incident*, *reflected* and *transmitted* waves respectively and θ is the angle of incidence. The constants ϵ_0 and μ_0 are the permitivity and permeability of free space. It also needs to be considered that each time a wave traverses the film it also picks up a phase shift $k_0(2n_I d\cos\theta_{iII})/2 = k_0 h$ where k_0 is the wavenumber.
After some algebra we obtain

$$\begin{bmatrix} E_I \\ H_I \end{bmatrix} = \begin{bmatrix} \cos k_0 h & (i\sin k_0)h)/\Upsilon_I \\ \Upsilon_I i \sin k_0 h & \cos k_0 h \end{bmatrix} \begin{bmatrix} E_{II} \\ H_{II} \end{bmatrix} \tag{A.4}$$

where

$$\Upsilon_I = \sqrt{\frac{\epsilon_0}{\mu_0}} \frac{n_I}{\cos\theta_{iI}} \tag{A.5}$$

If we denote the first matrix on the RHS as $\mathcal{M}_{\mathcal{I}}$ we can write

$$\begin{bmatrix} E_I \\ H_I \end{bmatrix} = \mathcal{M}_{\mathcal{I}} \begin{bmatrix} E_{II} \\ H_{II} \end{bmatrix} \tag{A.6}$$

Thus a third boundary would result in the relation

$$\begin{bmatrix} E_I \\ H_I \end{bmatrix} = \mathcal{M}_I \mathcal{M}_{II} \begin{bmatrix} E_{III} \\ H_{III} \end{bmatrix} \tag{A.7}$$

and hence it becomes very easy to add an arbitary number of slabs to the stack as long as one knows the optical constants of each material. The so called *characteristic* matrix

$$\mathcal{M} = \mathcal{M}_I \mathcal{M}_{II} \ldots \mathcal{M}_p \tag{A.8}$$

is just the product of the *characteristic* matrix for each interface.

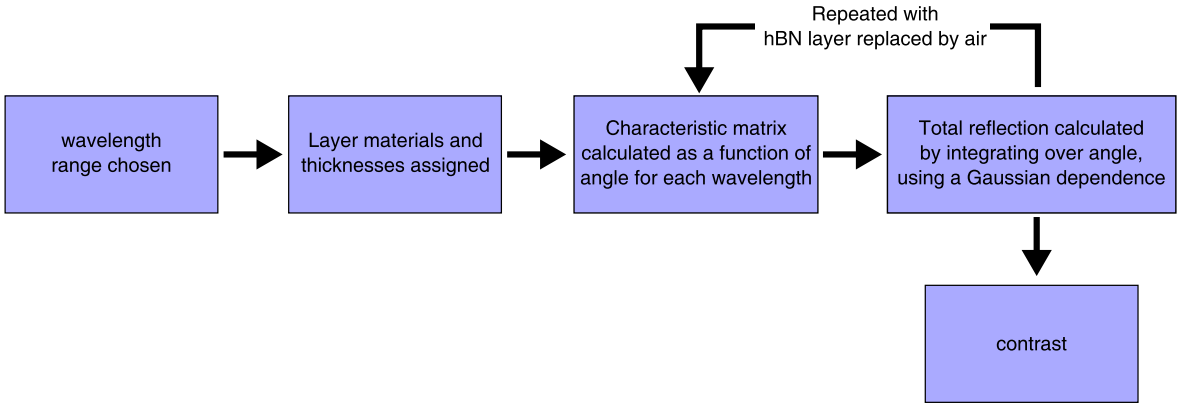

Figure A.3: Computation schematic to calculate contrast of few-layer hBN on Si/SiO_2.

With knowledge of the refractive indices of the constituent materials it is possible to calculate the total reflected and transmitted intensity of the system as a whole. The implementation of this was done in MatLab with the scheme in fig. A.3.

[7] Gorbachev, R. V. *et al.* *Small*, 7 (2011) 465–468.

A.2 Optimization of contrast on Si/SiO_2

The most relevant substrate for use is Si/SiO_2 because it is versatile and many fabrication processes are optimised for it. The contrast of mono- and bi- layer hBN was measured on a

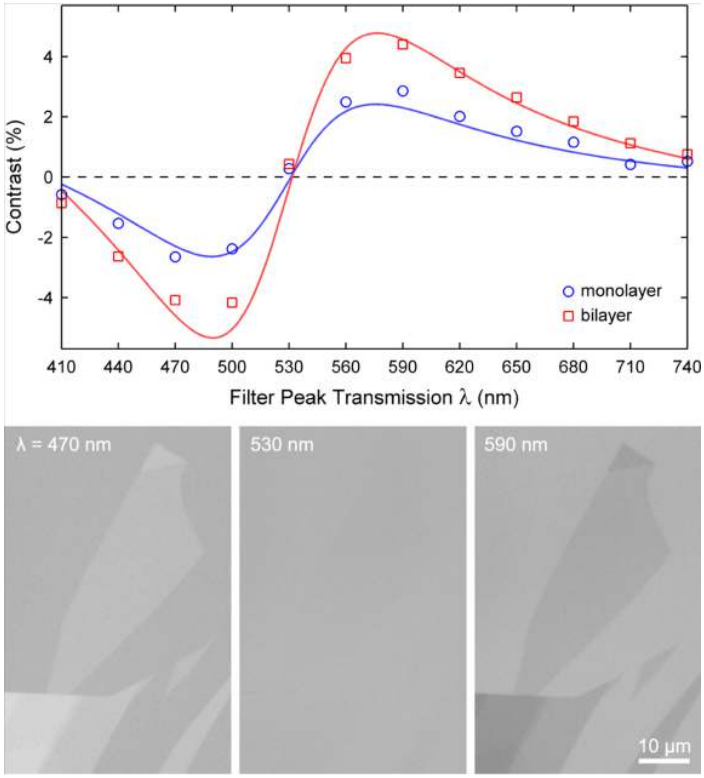

Figure A.4: The optical contrast of mono- and bi- layer hBN on a silicon wafer with 300 nm oxide. The points are experimental data and the solid lines are taken from the model. The lower panel shows grayscale optical images of the same hBN flake taken with wavelength filters of 470 nm, 530 nm and 590 nm. *This figure is taken from Gorbachev et al. (2010)*[8]

silicon wafer with a 300 nm oxide layer and is plotted in fig. A.4 as the open circles. The solid lines plotted are computed by the model described above and one can see a reasonable fit with experiment. One can see that selecting a wavelength filter of either 490 or 570 nm gives the best contrast. This is explicitly shown in the panel below. To further optimize conditions for flake hunting, a map such that shown in fig. A.5 was made. It shows the optical contrast for monolayer hBN as a function of both wavelength and oxide thickness. One can use the map to find the region with the highest values. It can be seen that using an oxide thickness of between 70-80 nm gives the best result because the contrast maintains the same sign over the visible range meaning hunting can be done in white light.

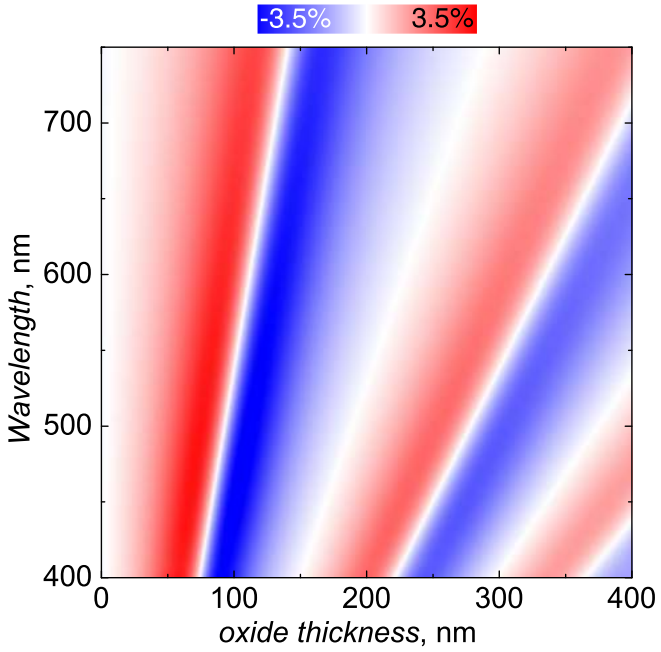

Figure A.5: Optical contrast of monolayer hBN on Si/SiO_2 mapped as a function of wavelength and oxide thickness.

Appendix B

Mechanical properties of fluorographene

The aim of this research was to investigate to what degree graphene's mechanical properties are degraded after fluorination. My contribution was determining the relative fracture load of graphene and fluorographene membranes using an atomic force microscopy probe. This work is published in Small as part of a more comprehensive study on fluorographene[1].

[1] Nair, R. R. *et al.* *Small*, 6 (2010) 2877–2884.

B.1 Introduction

Fluorographene is a chemical derivative of graphene which is formed by attaching fluorine atoms to the graphene lattice, fig. B.1. It has been suggested to be a potential material for use in applications where Teflon is currently used–such as low friction coatings–as it is more stable and inert. It would be useless however, if its mechanical strength made it unsuitable for such applications. Its mechanical strength was measured as part of the materials characterisation. This was done in the same way as described in section 2.1.5.

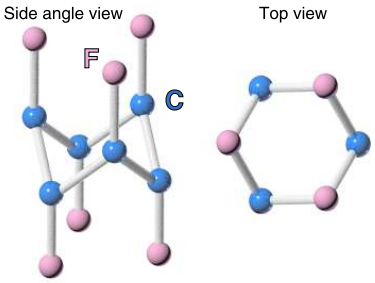

Figure B.1: The structure of flurographene.

B.2 Experimental results

Due to fluorine's highly reactive nature, it is not possible to use SiO_2 as a substrate. Instead, a standard transmission electron microscope (TEM) sample holder was used. These holders have Au support with an amorphous carbon scaffold with a periodic array of holes of diameter 1.6 µm. A graphene flake was transferred to the top of such a grid and placed in proximity to XeF_2 for 1 week[2]. This is sufficient time for the XeF_2 to dissociate and the F atoms to bind to the graphene stoichiometrically in a C:F 1:1 ratio. Raman spectra taken on the flakes at various stages of fluorination are shown in fig. B.2. One can see that in pristine graphene there is no D peak visible. After 1 day, a strong D peak appears at 1340 cm^{-1} showing a large presence of defects. Finally after 1 week of fluorination the peaks are almost completely absent in the

[2] Nair, R. R. *et al.* *Small*, 6 (2010) 2877–2884.

spectra as fluorographene becomes transparent to the laser light as the band gap exceeds the excitation energy.

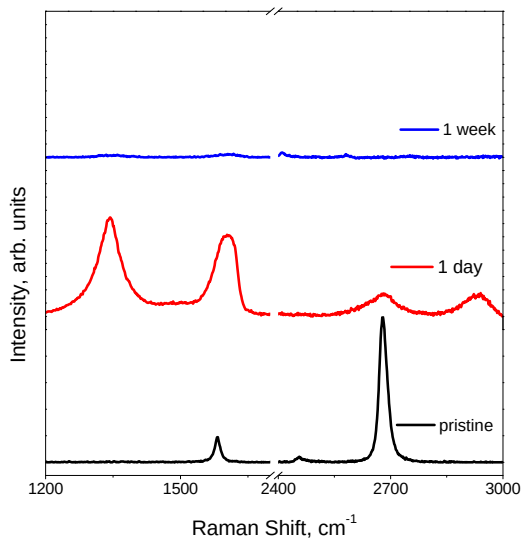

Figure B.2: Raman spectra of pristine graphene and after fluorination time of 1 day and 1 week. *The Raman spectra shown were measured by R. Nair*

In order to determine the fracture force, an AFM tip would be intentionally driven into the membrane centre until breakage. It was important to find the centre accurately to impart isotropic strain on the membrane. The underlying grid had a small lip surrounding the hole (∼20 nm high) and this was used to find the centre. Monitoring linescans whilst scanning the membrane at 0° orientation, the maximum distance between the edges was found. The scan was rotated to 90° and the process repeated. For each membrane this was done three times to ensure the tip was centred on the membrane.

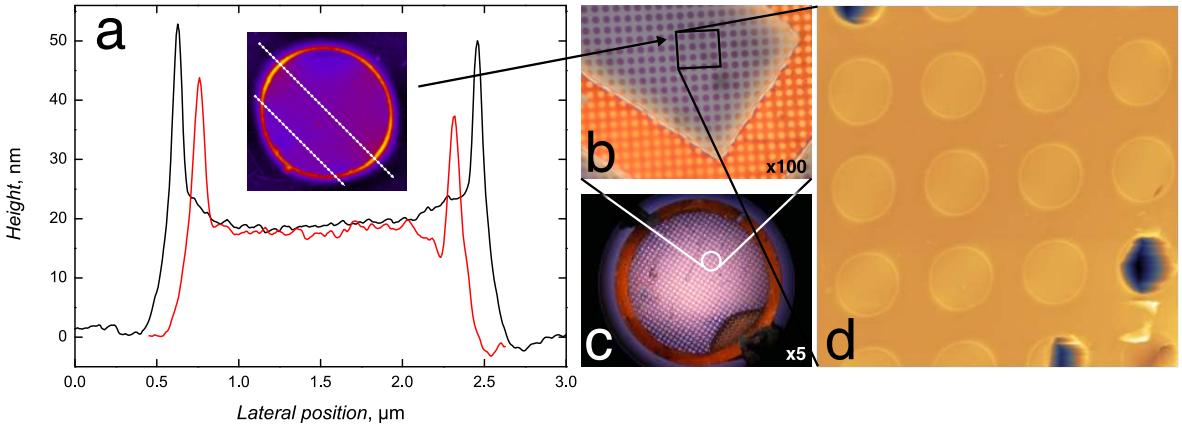

Figure B.3: Method to find the membrane's centre

In order to obtain statistics, 15 fully covered holes were measured by TM-AFM, examples in fig. B.3, and the AFM tip

was driven into their centre while force-distance curves were recorded to the fracture point. The point of fracture was simple to find as the example in fig. B.4 shows. The sudden drop observed in the load curve was used.

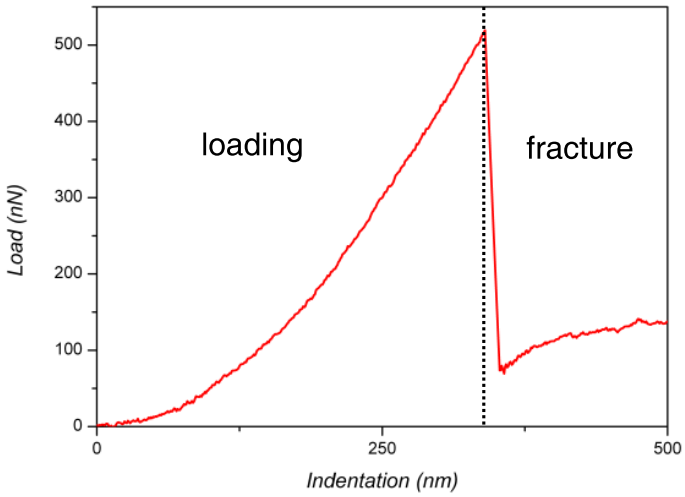

Figure B.4: Force-displacement curve up to the fracture point of the fluorographene membrane.

Unlike the situation described in section 2.1.5, it was not possible to determine the Young's modulus of flurographene because of the deflection of the carbon support. Whereas any deformation in SiO_2 is negligible, the carbon grid was observed to deflect by an amount that rendered analysis unreliable. As such only an analysis of the fracture load could be determined. A histogram of the fracture force for the 15 membranes is shown in fig. B.5. The peak in the distribution is at 0.35, where the number has been normalised to the fracture load of a pristine graphene flake taken under the same conditions. The before and after TM-AFM images are shown in fig. B.5. After fracture, the previously complete membrane shows a large rip eminating from the centre to one edge.

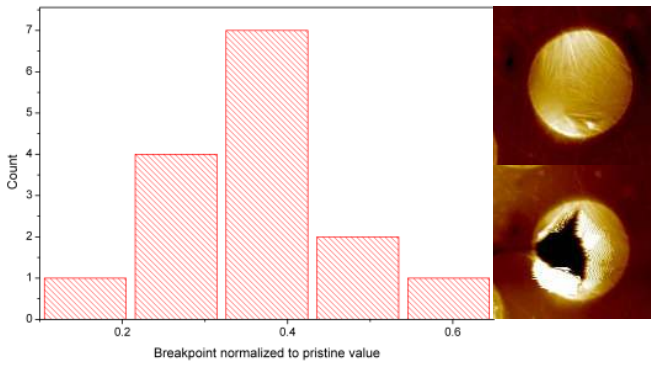

Figure B.5: Histogram of the normalised fracture load of fluorographene

References

◇ Ashcroft, N. W. & Mermin, N. *Solid State Physics*. Harcourt Brace (1976).

◇ Ayari, A., Cobas, E., Ogundadegbe, O. & Fuhrer, M. S. Realization and electrical characterization of ultrathin crystals of layered transistion-metal dichalcogenides. *Journal of Applied Physics* **101**, 014507 (2007).

◇ Bae, S., KIm, H., Lee, Y., Xiangfan, X., Park, J.-S., Zheng, Y., Balakrisnan, J., Lei, T., Kim, H. R., Song, Y. I., Kim, Y.-S., Kwang, S., Özylimaz, B., Ahn, J.-H., Hong, B. H. & Iijima, S. Roll-to-roll production of 30-inch graphene films for transparent electrodes. *Nature Nanotechnology* **5**, 574–578 (2010).

◇ Bai, J., Zhong, X., Jiang, S., Huang, Y. & Duan, X. Graphene nanomesh. *Nature Nanotechnology* **5**, 190–194 (2010).

◇ Balandin, A. A., Ghosh, S., Bao, W., Calizo, I., Teweldebrhan, D., MMiao, F. & Lau, C. N. Superior thermal conductivity of single-layer graphene. *Nano Letters* **8**, 902–907 (2008).

◇ Ballif, C., Regula, P. E., Schmid, M., Remskar, M., Sanjinés, R. & Lévy, F. Preparation and characterization of highly oriented, photoconducting WS_2 thin films. *Applied Physics A: Materials Science & Processing* **62**, 543–546 (1996).

◇ Bardeen, J. Tunnelling from a many-particle point of view. *Physical Review Letters* **6**, 57–59 (1961).

◇ Binnig, G., Quate, C. F. & Gerber, C. Atomic force microscope. *Physical Review Letters* **56**, 930–933 (1986).

◇ Binnig, G. & Rohrer, H. Scanning tunneling microscopy. *IBM Journal of Research and Development* **30**, 355–369 (1986).

◇ Blake, P., Hill, E. W., Neto, A. H. C., Novoselov, K. S., Jiang, D., Yang, R., Booth, T. J. & Geim, A. K. Making graphene visible. *Applied Physics Letters* **91**, 063124 (2007).

◇ Bolotin, K. I., Sikes, K. J., Hone, J., Stormer, H. L. & Kim, P. Temperature-dependent transport in suspended graphene. *Physical Review Letters* **101**, 096802 (2008).

◇ Bonaccorso, F., Sun, Z., Hasan, T. & Ferrari, A. C. Graphene photonics and optoelectronics. *Nature Photonics* **4**, 611–622 (2010).

◇ Britnell, L., Gorbachev, R. V., Jalil, R., Belle, B. D., Schedin, F., Katsnelson, M. I., Eaves, L., Morozov, S. V., Mayorov, A. S., Peres, N. M. R., Castro Neto, A. H., Leist, G. A. K., J., Ponomarenko, L. A. & Novoselov, K. S. Electron tunneling through ultrathin boron nitride crystalline barriers. *Nano Letters* **12**, 1707–1710 (2012).

◇ Britnell, L., Gorbachev, R. V., Jalil, R., Belle, B. D., Schedin, F., Mishchenko, A., Katsnelson, M. I., Eaves, L., Morozov, S. V., Peres, N. M. R., Leist, J., Geim, A. K., Novoselov, K. S. & Ponomarenko, L. A. Field-effect tunneling transistor based on vertical graphene heterostructures. *Science* **335**, 947–950 (2012).

◇ Bromley, R. A., Murray, R. B. & Yoffe, A. D. The band structures of some transition metal dichalcogenides: III. Group VI A: trigonal prism materials. *Journal of Physics C: Solid Sate Physics* **5**, 759–778 (1972).

◇ Casiraghi, C., Harschuh, A., Lidorikis, E., Qian, H., Harutyunyan, H., Gokus, T., Novoselov, K. S. & Ferrari, A. C. Rayleigh imaging of graphene and graphene layers. *Nano Letters* **7**, 2711–2717 (2007).

◇ Chatzitheodorou, G., Fiechter, S., Kunst, M., Luck, J. & Tributsch, H. Low temperature chemical preparation of semiconducting transition metal chalcogenide films for energy conversion and storage, lubrication and surface protection. *Materials Research Bulletin* **23**, 1261–1271 (1988).

◇ Cohen, S. R., Rapoport, L., Ponomarev, E. A., Cohen, H., Tsirlina, T., Tenne, R. & Lévy-Clément, C. The tribological behaviour of type II textured MX_2 (M=Mo, W; X=S, Se) films. *Thin Solid Films* **1-2**, 190–197 (1998).

◇ Coleman, J. N., Lotya, M., O'Neill, A., Bergin, S. D., King, P. J., Khan, U., Young, K., Gaucher, A., De, S., Smith, R. J., Shvets, I. V., Arora, S. K., Stanton, G., Kim, H.-Y., Lee, K., Kim, G. T., Duesberg, G. S., Hallam, T., Boland, J. J., Wang, J. J., Donegan, J. F., Grunlan, J. C., Moriarty, G., Shmeliov, A., Nicholls, R. J., Perkins, J. M., Grieveson, E. M., Theuwissen, K., McComb, D. W., Nellist, P. D. & Nicolosi, V. Two-dimensional nanosheets produced by liquid exfoliation of layered materials. *Science* **331**, 568–571 (2011).

◇ Das, A., Pisana, S., Chakrabory, B., Piscanec, S., .Saha, S. K., Waghmare, U. V., Novoselov, K. S., Krishnamurthy, H. R., Geim, A. K., Ferrari, A. C. & Sood, A. K. Monitoring dopants by Raman spectroscopy scattering in an electrochemically top-gated graphene transistor. *Nature Nanotechnology* **3**, 210–215 (2008).

◇ Dean, C. R., Young, A. F., Cadden-Zimansky, P., Wang, L., Ren, H., Watanabe, K., Taniguchi, T., Kim, P., Hone, H. & Shepard, K. L. Multicomponent fractional quantum Hall effect in graphene. *Nature Physics* **7**, 693–696 (2011).

◇ Dean, C. R., Young, A. F., Meric, I., Lee, C., Wang, L., Sorgenfrei, S., Watanabe, K., Taniguchi, T., Kim, P., Shepard, K. L. & Hone, J. Boron nitride substrates for high-quality graphene electronics. *Nature Nanotechnology* **5**, 722–726 (2010).

◇ Dresselhaus, M. S., Jorio, A., Cançado, L. G., Dresselhaus, G. & Saito, R. *Graphene nanoelectronics Chapter 2: Raman spectroscopy: Characterization of edges, defects, and the Fermi energy of graphene and sp^2 carbons.* Springer (2012).

◇ Dresselhaus, M. S., Jorio, A., Filho, A. G. S. & Saito, R. Defect characterization in graphene and carbon nanotubes using Raman spectroscopy. *Philosophical Transactions of the Royal Society* **368**, 5355–5377 (2010).

◇ Eaton, P. & West, P. *Atomic Force Microscopy.* Oxford University Press (2010).

◇ Eaves, L., Greenway, M. T. & Fromhold, T. M. Private Communication (2012).

◇ Eckmann, A., Felten, A., Mishchenko, A., Britnell, L., Krupke, R., Novoselov, K. S. & Casiraghi, C. Probing the nature of defects in graphene by Raman spectroscopy. *Nano Letters* **12**, 3925–3930 (2012).

◇ Eisenstein, J. P., Pfeiffer, L. N. & West, K. W. Coulomb barrier to tunnelling between parallel 2-dimensional electron-systems. *Physical Review Letters* **69**, 3804–3807 (1992).

◇ Elias, D. C., R. R., N., Mohiuddin, T. M. G., Morozov, S. V., Blake, P., Ferrari, A. C., Bokhvalov, D. W., Katsnelson, M. I., Geim, A. K. & Novoselov, K. S. Control of graphene's properties by reversible hydrogenation: evidence of graphane. *Science* **323**, 610–613 (2009).

◇ Emtsev, K. V., Bostwick, A., Horn, K., Jobst, J., Kellogg, G. L., Ley, L., McChesney, J. L., Ohta, T., Reshanov, S. A., Röhrl, J., Rotenberg, E., Schmid, A. K., Waldmann, D., Weber, H. B. & Seyller, T. Towards wafer-size graphene layers by atmospheric pressure graphitization of silicon carbide. *Nature Materials* **8**, 203–207 (2009).

◇ Feenstra, R. M., Jena, D. & Gu, G. Single-particle tunneling in doped graphene-insulator-graphene junctions. *Journal of Applied Physics* **111**, 043711 (2012).

◇ Ferrari, A. C. Raman spectroscopy of graphene and graphite: Disorder, electron–phonon coupling, doping and nonadiabatic effects. *Solid State Communications* **143**, 47–57 (2007).

◇ Ferrari, A. C., Meyer, J. C., Scardaci, V., Casiraghi, C., Lazzeri, M., Mauri, F., Piscanec, S., Jiang, D., Novoselov, K. S., Roth, S. & Geim, A. K. Raman spectrum of graphene and graphene layers. *Physical Review Letters* **97**, 187401 (2006).

◇ Garcia, A. G., Neumann, M., Amet, F., Williams, J. R., Watanabe, K., Taniguchi, T. & Goldhaber-Gordon., D. Effective cleaning of hexagonal boron nitride for graphene devices. *Nano Letters* (2012).

◇ Georgiou, T., Jalil, R., Belle, B. D., Britnell, L., Geim, A. K., Novoselov, K. S. & Mishchenko, A. Graphene-WS_2 heterojunction: high performance, flexible field effect transistor. *Unpublished* (2012).

◇ Giovannetti, G., Khomyakov, P. A., Brocks, G., Karpan, V. M., van den Brink, J. & Kelly, P. J. Doping graphene with metal contacts. *Physical Review Letters* **101**, 026803 (2008).

◇ Gomes, K. K., Mar, W., Ko, W., Guinea, F. & Manoharan, H. C. Designer Dirac fermions and topological phases in molecular graphene. *Nature* **483**, 306–310 (2012).

◇ Gómez-Navarro, C., Meyer, J. C., Sundaram, R. S., Chuvilin, A., Jurasch, S., Burghard, M., Kern, K. & Kaiser, U. Atomic structure of reduced graphene oxide. *Nano Letters* **10**, 1144–1148 (2010).

◇ Gorbachev, R. V., Riaz, N. R. R., I., Jalil, R., Britnell, L., Belle, B. D., Hill, E. W., Novoselov, K. S., Watanabe, K., Taniguchi, T., Geim, A. K. & Blake, P. Hunting for monolayer boron nitride: optical and Raman signatures. *Small* **7**, 465–468 (2011).

◇ Gutiérrez, H. R., Perea-López, N., Elias, A. L., Berkdemir, A., Wang, B., Lv, R., López-Urias, F., Crespi, V. H., Terrones, H. & Terrones, M. Extraordinary room-temperature photoluminescence in WS_2 monolayers. *arXiv:1208.1325* (2012).

◇ Haigh, S. J., Gholinia, A., Halil, R., Romani, S., Britnell, L., Elias, D. C., Novoselov, K. S., Ponomarenko, L. A., Geim, A. K. & Gorbachev, R. Cross-sectional imaging of individual layers and buried interfaces of graphene-based heterostructures and superlattices. *Nature Materials* **11**, 764–767 (2012).

◇ Han, M. Y., ẗOzyilmaz, B., Zhang, Y. & Kim, P. Energy band-gap engineering of graphene nanoribbons. *Physical Review Letters* **98**, 206805 (2007).

◇ Hecht, E. *Optics*. Addison-Wesley (2002).

◇ Hertel, S., Waldmann, D., Jobst, J., Albrecht, A., Reshanov, S., Schöner, A., Krieger, M. & Weber, H. B. Tailoring the graphene/silicon carbide interface for monolithic wafer-scale electronics. *Nature Communications* **3**, 957 (2012).

◇ Hilton, M. R. & Fleischauer, P. D. Applications of solid lubricant films in spacecraft. *Surface and Coatings Technology* **54-55**, 435–441 (1992).

◇ Huang, X., Qi, X., Boey, F. & Zhang, H. Graphene-based composites. *Chemical Society Reviews* **41**, 666–686 (2012).

◇ Kam, K. K. & Parkinson, B. A. Detailed photocurrent spectroscopy of the semiconducting group IV transistion metal dichalcogenides. *Journal of Physical Chemistry* **86**, 463–467 (1982).

◇ Kharche, N. & Nayak, S. K. Quasiparticle band gap engineering of graphene and graphone on hexagonal boron nitride substrate. *Nano Letters* **11**, 5274–5278 (2011).

◇ Kumar, A. & Ahluwalia, P. K. Electronic structure of transition metal dichalcogenides monolayers 1H-MX_2 (M = Mo, W; X = S, Se, Te) from ab-initio theory: new direct band gap semiconductors. *European Physical Journal B* **85**, 186 (2012).

◇ Lee, C., Li, Q., Kalb, W., Liu, X.-Z., Berger, H., Carpick, R. W. & Hone, J. Frictional characteristics of atomically thin sheets. *Science* **328**, 76–80 (2010).

◇ Lee, C., Wei, X., Kysar, H. W. & Hone, H. Measurement of the elastic properties and intrinsic strength of monolayer graphene. *Science* **321**, 385–388 (2008).

◇ Lee, E. J. H., Balasubramanian, K., Weitz, R. T., Burghard, M. & Kern, K. Contact and edge effects in graphene devices. *Nature Nanotechnology* **3**, 486–490 (2008).

◇ Li, H., Zhang, Q., Yap, C. C. R., Tay, B. K., Edwin, T. H. T., Olivier, A. & Baillargeat, D. From bulk to monolayer MoS_2: evolution of Raman scattering. *Advanced Functional Materials* **22**, 1385–1390 (2012).

◇ Li, X., Cai, W., Columbo, L. & Ruoff, R. S. Evolution of graphene growth on Ni and Cu by carbon isotope labelling. *Nano Letters* **9**, 4268–4272 (2009).

◇ Lipson, S., Lipson, H. S. & Tannhauser., D. *Optical Physics*. Cambridge Unversity Press (1995).

◇ Liu, J., Tang, H. & Gooding, J. J. Strategies for chemical modification of graphene and applications of chemically modified graphene. *Journal of Materials Chemistry* **22**, 12435–12452 (2012).

◇ Martin, J., Akerman, N., Ulbricht, G., Lohmann, T., Smet, J. H., Klitzing, K. V. & Yacoby, A. Observation of electron-hole puddles in graphene using a scanning single-electron transistor. *Nature Physics* **4**, 144–148 (2007).

◇ Masubuchi, S., Ono, M., Yoshida, K., Hirakawa, K. & Machida, T. Fabrication of graphene nanoribbon by local anodic oxidation lithography using atomic force microscope. *Applied Physics Letters* **94**, 082107 (2009).

◇ Mattevi, C., Kim, H. & Chhowalla, M. A review of chemical vapour deposition of graphene of copper. *Journal of Materials Chemistry* **21**, 3324–3334 (2011).

◇ Mattheiss, L. F. Band structures of transistion-metal-dichalcogenide layer compounds. *Physical Review B* **8**, 3719–3740 (1973).

◇ Mayorov, A. S., Elias, D. C., Mukhin, I. S., Morozov, S. V., Ponomarenko, L. A., Novoselov, K. S., Geim, A. K. & Gorbachev, R. V. How close can one approach the Dirac point in graphene experimentally? *Nano Letters* **12**, 4629–4634 (2012).

◇ Mayorov, A. S., Gorbachev, R. V., Morozov, S. V., Britnell, L., Jalil, R., Ponomarenko, L. A., Blake, P., Novoselov, K. S., Watanabe, K., Taniguchi, T. & Geim, A. K. Micrometer-scale ballistic transport in encapsulated graphene at room temperature. *Nano Letters* **11**, 2396–2399 (2011).

◇ Mizuta, H. & Tomonori, T. *The Physics and Applications of Resonant Tunnelling Diodes*. Cambridge Unversity Press (1995).

◇ Mohiuddin, T. M. G., Lombardo, A., Nair, R. R., Bonetti, A., Savini, G., Jalil, R., Bonini, N., Basko, D. M., Galiotis, C., Marzari, N., Novoselov, K. S., Geim, A. K. & Ferrari, A. C. Uniaxial strain in graphene by Raman spectroscopy: G peak splitting, Grüneisen parameters, and sample orientation. *Physical Review B* **79**, 205433 (2009).

◇ Nair, R. R., Blake, P., Grigorenko, A. N., Novoselov, K. S., Booth, T. J., Peres, N. M. R. & Geim, A. K. Fine structure constant defines visual transparency of graphene. *Science* **320**, 1308 (2008).

◇ Nair, R. R., Ren, W., Jalil, R., Riaz, I., Kravets, V. G., Britnell, L., Blake, P., Schedin, F., Mayorov, A. S., Yuan, S., Katsnelson, M. I., Cheng, H.-M., Strupinski, W., Bulusheva, L. G., Okotryb, A. V., Grigorieva, I. V., Grigorenko, A. N., Novoselov, K. S. & Geim, A. K. Fluorinated graphene: fluorographene: a two-dimensional counterpart of teflon. *Small* **6**, 2877–2884 (2010).

◇ Nair, R. R., Wu, H. A., Jayaram, P. N., Grigorieva, I. V. & Geim, A. K. Unimpeded permeation of water through helium-leak-tight graphene-based membranes. *Science* **335**, 442–444 (2012).

◇ Neto, A. H. C., Guinea, F., Peres, N. M. R., Novoselov, K. S. & Geim, A. K. The electronic properties of graphene. *Reviews of Modern Physics* **81**, 109–162 (2009).

◇ Ni, Z. H., Ponomarenko, L. A., Nair, R. R., Yang, R., Anissiova, S., Grigorieva, I. V., Schedin, F., Blake, P., Shen, Z. X., Hill, E. H., Novoselov, K. S. & Geim, A. K. On resonant scatterers as a factor limiting carrier mobility in graphene. *Nano Letters* **10**, 3868–3872 (2010).

◇ Novoselov, K. S. Graphene: materials in the flatland (Nobel lecture). *Angewandte Chemie International Edition* **50**, 6986–7002 (2011).

◇ Novoselov, K. S., Falko, V. I., Columbo, L., Gellert, P. R., Schwab, M. G. & Kim, K. A roadmap for graphene. *Nature* **490**, 192–200 (2012).

◇ Novoselov, K. S., Geim, A. K., Morozov, S. V., Jiang, D., Katsnelson, M. I., Grigorieva, I. V., Dubonos, S. V. & Firsov, A. A. Two-dimensional gas of massless Dirac fermions in graphene. *Nature* **438**, 197–200 (2005).

◇ Novoselov, K. S., Geim, A. K., Morozov, S. V., Jiang, D., Zhang, Y., Dubonos, S. V., Grigorieva, I. V. & Firsov, A. A. Electric field effect in atomically thin carbon films. *Science* **306**, 666–669 (2004).

◇ Novoselov, K. S., Jiang, D., Schedin, F., Booth, T. J., Khotkevich, V. V., Morozov, S. V. & Geim, A. K. Two-dimensional atomic crystals. *Proceedings of the National Academy of Sciences of the United States of America* **102**, 10451–10453 (2005).

◇ Ooi, N., Rajan, V., Gottlieb, J., Catherine, Y. & Adams, J. B. Structural properties of hexagonal boron nitride. *Modelling and Simulation in Materials Science and Engineering* **14**, 515–535 (2006).

◇ O'Shea, S. J., Atta, R. M. & Welland, M. E. Characterization of tips for conducting atomic force microscopy. *Reviews of Scientific Instruments* **66**, 2508 (1995).

◇ Pachoud, A., Jaiswal, M., Ang, P. K., Loh, K. P. & Özyilmaz, B. Graphene transport at high carrier densities using a polymer electrolyte gate. *Europhysics Letters* **92**, 27001 (2010).

◇ Palik, E. D. *Handbook of Optical Constants of Solids*. Academic Press (1984).

◇ Park, S. & Ruoff, R. S. Chemical methods for the production of graphenes. *Nature Nanotechnology* **4**, 217–224 (2009).

◇ Ponomarenko, L. A., Geim, A. K., Zhukov, A. A., Jalil, R., Morozov, S. V., Novoselov, K. S., Grigorieva, I. V., Hill, E. H., Cheianov, V. V., Falko, V., Watanabe, K., Taniguchi, T. & Gorbachev, R. V. Tunable metal-insulator transition in double-layer graphene heterostructures. *Nature Physics* **7**, 958–961 (2011).

◇ Radmacher, M. Measuring the elastic properties of living cells by the atomic force microscopy. *Methods in Cell Biology* **68**, 67–90 (2002).

◇ Saito, R., Dresselhaus, G. & Dresselhaus, M. S. *Physical Properties of Carbon Nanotubes*. Imperial College Press (1998).

◇ Samarakoon, D. K., Chen, Z., Nicolas, C. & Wang, X.-Q. Structural and electronic properties of fluorographene. *Small* **7**, 965–969 (2011).

◇ Sarma, S. D., Adam, S., Hwang, E. H. & Rossi, E. Electronic transport in two-dimensional graphene. *Reviews of Modern Physics* **83**, 407–470 (2011).

◇ Schedin, F., Geim, A. K., Morozov, S. V., Jiang, D., Hill, E. H., Blake, P. & Novoselov, K. S. Detection of individual gas molecules adsorbed on graphene. *Nature Materials* **6**, 652–655 (2007).

◇ Schneider, G. F., Calado, V. E., Zandbergen, H., Vandersypen, L. M. K. & Dekker, C. Wedging transfer of nanostructures. *Nano Letters* **10**, 1912–1916 (2010).

◇ Schutte, W. H., De Boer, J. L. & Jellinek, F. Crystal structures of tungsten disulfide and diselenide. *Journal of Solid State Chemistry* **70**, 207–209 (1987).

◇ Simmons, J. G. Generalized formula for the electric tunnel effect between similar electrodes separated by a thin insulating film. *Journal of Applied Physics* **34**, 1793–1803 (1963).

◇ Song, L., Ci, L., Lu, H., Sorokin, P. B., Jin, C., Ni, J., Kvashnin, A. G., Kvashnin, D. G., Lou, J., Yakobson, B. I. & Ajayan, P. M. Large scale growth and characterisation of atomic hexagonal boron nitride layers. *Nano Letters* **10**, 3209–3215 (2010).

◇ Stampfer, C., Fringes, S., Güttinger, J., Molitor, F., Volk, C., Terrés, B., Dauber, J., Engels, S., Schnez, S., Jacobsen, A., Dröscher, S., Ihn, T. & Ensslin, K. Transport in graphene nanostructures. *Frontiers of Physics* **6**, 271–293 (2011).

◇ Tenne, R., Margulis, L., Genut, M. & Hodes, G. Polyhedral and cylindrical structures of tungsten disulphide. *Nature* **360**, 444–446 (1992).

◇ Tributsch, H., Gerischer, H., Clemen, C. & Bucher, E. On the photopotential output of electrochemical solar cells based on layer-type d-band semiconductors. *Phys. Chemie* **83**, 1655 (1979).

◇ Wallace, P. R. The band theory of graphite. *Physical Review Letters* **71**, 622–634 (1947).

◇ Wang, Q. H., Jin, Z., Kim, K. K., Hilmer, A. J., Paulus, G. L. C., Shih, C.-J., Ham, M.-H., Sanchez-Yamagishi, J. D., Watanabe, K., Taniguchi, T., Kong, H., Jarillo-Herrero, P. & Strano, M. S. Understanding and controlling the substrate effect on graphene electron-transfer chemistry via reactivity imprint lithography. *Nature Chemistry* **4**, 724–732 (2012).

◇ Watanabe, K., Taniguchi, T. & Kanda, H. Direct-bandgap properties and evidence for ultraviolet lasing of hexagonal boron nitride single crystal. *Nature Materials* **3**, 404–409 (2004).

◇ Wilson, J. A. & Yoffe, A. D. The transition metal dichalcogenides discussion and interpretation of the observed optical, electrical and structural properties. *Advances in Physics* **18**, 193–335 (1969).

◇ Wu, Y., ming Lin, Y., Bol, A. A., Jenkins, K. A., Xia, F., Farmer, D. B., Zhu, Y. & Avouris, P. High-frequency, scaled graphene transistors on diamond-like carbon. *Nature* **472**, 74–78 (2011).

◇ Xu, Y. N. & Ching, W. Y. Calculation of ground-state and optical properties of boron nitrides in the hexagonal, cubic and wurtzite structures. *Physical Review B* **44**, 7787–7798 (1991).

◇ Yang, H., Heo, J., Park, S., Song, H. J., Seo, D. H., Byun, K.-E., Kim, P., Yoo, I., Chung, H.-J. & Kim, K. Graphene barristor, a triode device with a gate-controlled Schottky barrier. *Science* **336**, 1140–1143 (2012).

◇ Yankowitz, J. X. M., Cormode, D., Sanchez-Yamagishi, J. D., Watanabe, K., Taniguchi, T., Jarillo-Herrero, P., Jacquod, P. & LeRoy, B. J. Emergence of superlattice Dirac points in graphene on hexagonal boron nitride. *Nature Physics* **8**, 382–386 (2012).